Delft University of Technology

Force characterization for a submerged velocity cap in unsteady flows

Giovanni Doni

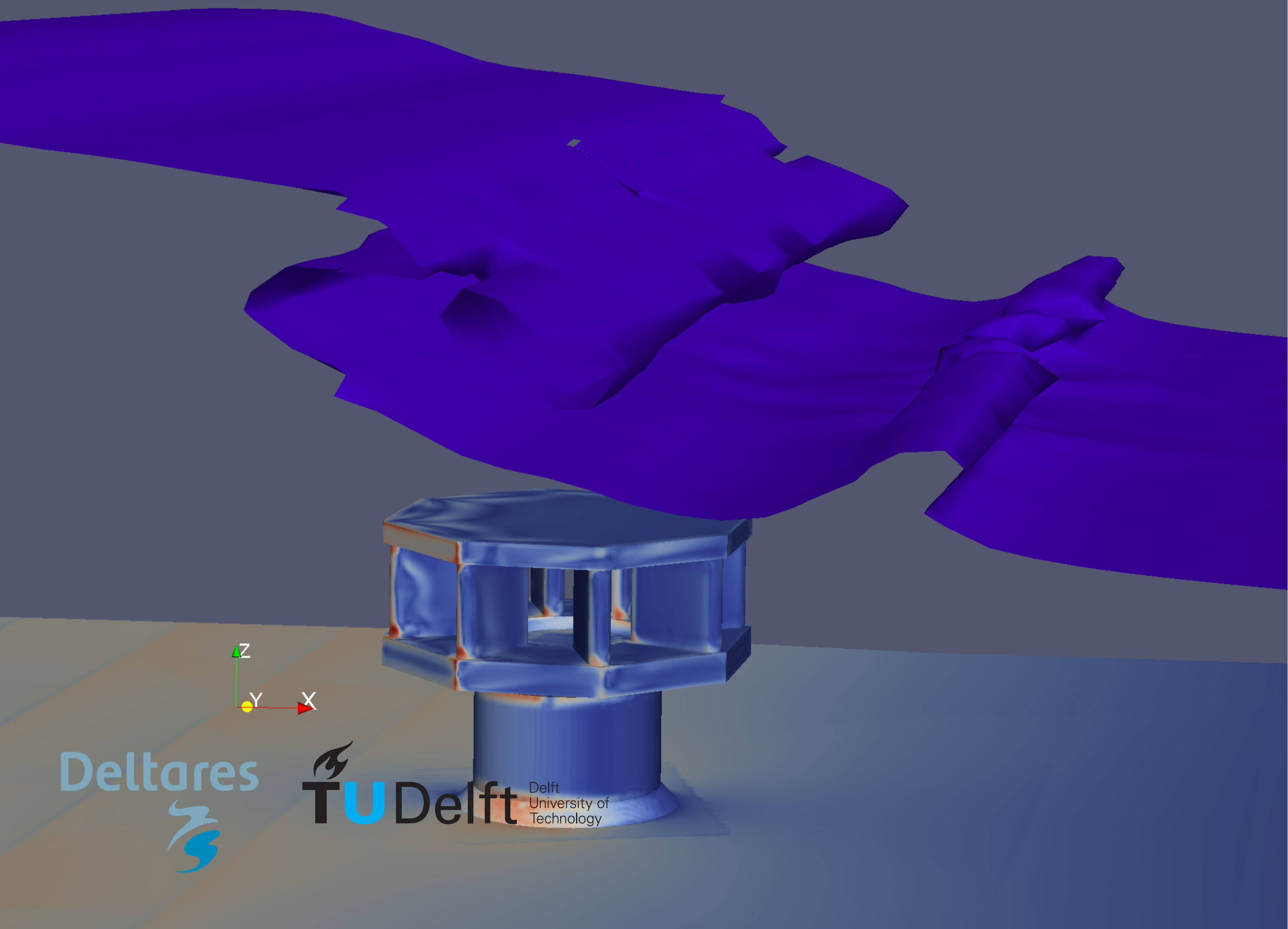

Force characterization for a submerged velocity cap in unsteady flows

by

Giovanni Doni

in partial fulfillment of the requirements for the degree of

Master of Science

in Civil Engineering

at the Delft University of Technology,

to be defended on Tuesday December 11, 2018 at 01:30 PM.

Student number:	4627881	
Project duration:	February, 2018 – October, 2018	
Thesis committee:	Prof. dr. ir. W.J.S. Uijttewaal (chairman)	TU Delft
	Dr. ir. J.D. Bricker (daily supervisor)	TU Delft
	Dr. ir. B. Hofland	TU Delft
	Dr. N.G. Jacobsen (company daily supervisor)	Deltares
	Ir. A. de Fockert	Deltares

In the cover: an impression of the velocity cap captured by means of the visualization software ParaFoam.

Summary

Coastal facilities such as desalination plant or a nuclear power plant need a continuous discharge of salty water to carry out their functions. Hereby an intake structure, such as a velocity cap, can be used to take in water from the sea. These intakes are open seafloor founded constructions mounted at a water depth ranging between 10 and 20 meters. It is composed by a top part with openings and guiding walls, and a vertical hollow shaft which is the beginning of the discharge pipe. The specific geometry prevents the formation of a whirlpool from the surface and avoids that bed sediments or floating debris are taken in.
In order to design such an intake cap in an offshore environment, the action of waves and in general of unsteady flows is the most important design load to be accounted for.

This thesis has the aim to investigate the nature of the forces and turning moment acting on the structure and to provide tools, in the form of hydrodynamic coefficients, that can be used to compute the design loads. These coefficients are only known from literature for simple geometries and defining them for the specific shape of the velocity cap can optimize the design. The analysis is based at first on experimental records collected during a previous campaign which included forces and surface elevation measurements as well as Particle Image Velocimetry (PIV). The measurements are then used to validate a CFD model in OpenFOAM®. The focus is mainly on the loads generated by the passage of solitary waves which were simulated both experimentally and numerically.
The characterization of the flow field is based on the analysis of the inline velocity which is used to estimate the Keulegan-Carpenter number (KC) and the frequency number (β). The availability of PIV measurements allowed studying the development of the turbulent patterns around the cap during the passage of a solitary wave. Structure-induced turbulence is shown to be fundamental to define the total loads on the structure in the numerical model. The use of a turbulence closure is in fact observed to be needed in order to come to a validation of the CFD model.
The visualization of the flow field computed by the model showed that the turbulence development after the solitary wave has passed was not captured correctly. Although this is likely to be the reason why the tail of the computed force signal underestimates the experimental records, the peak of the force signal is predicted with an accuracy of ± 8%. In the case of the vertical load the error observed between numerical results and experimental records reached up to 15% but part of the mismatch is attributed to a bias in the experimental records.

Once the CFD tool is validated, it is used to generate additional test cases on solitary waves and regular waves in order to expand the scope of this research. The hydrodynamic force coefficients are defined fitting both the experimental records and the load estimates of the numerical model by means of the weighted least squares method. The inline force characterization followed the theory of the Morison equation which is shown to provide a good fit in all analyzed cases. Good agreement is found between numerical and experimental results with regards to the estimate of the inertia coefficient while the numerical estimate of the drag coefficient is up to 19 % lower than the experimental estimate.
Vertical force and overturning moment signals were originally fitted with the most common formulas used in literature which relate the variation of these two loads to a horizontal drag term only. The mismatch between the fit obtained and the original signals suggested that the classical formulas needed to be expanded with one or more extra terms. The best fits for the vertical force are found with an equation that includes the effect of the horizontal drag, the vertical drag and of the vertical inertia, while in the case of the turning moment the best fits are obtained with a combination of horizontal drag, vertical drag, horizontal inertia and vertical inertia.

Preface

This thesis has been produced as final work to fulfill my MSc in Hydraulinc Engineering at the Delft University of Technology.
The work was entirely carried out at Deltares which I thank for the financial support and the offer of a professional and enjoyable workplace.

First of all I want to thank Niels Jacobsen for the help, suggestions and opinions on my work which helped me keep focus in the long and, at times, challenging months of the thesis project.

I am extremely grateful to the rest of my committee, Prof. Uijttewaal, Dr. Hoflad, Dr. Bricker, and Ir. de Fockert. as well. I feel happy and honored of having worked under their guidance.

I definitely cannot forget thanking the people I met at Deltares and who helped me considerably in my job. In first place Helena who worked on the post-processing of the PIV data and then Gosse and Wout for the important advice regarding many aspects of the PIV measuring technique. Additionally, I want to thank Alex Capel for the information on the set-up of the past experiments and last but not least Karen for her warmth and her exquisite coffee.

Finally my parents and my girlfriend, the people that were listening to me even when I, tired or demotivated, was blabbering for entire days. Your support, suggestions and love kept me going.

Giovanni Doni
Delft, December 2018

Contents

List of Tables xi

List of Figures xiii

Nomenclature xix

1 Introduction 1
- 1.1 Context . . . 1
- 1.2 Physical model tests at Deltares . . . 2
- 1.3 Research question . . . 3
- 1.4 Thesis structure . . . 3

2 Literature review on hydrodynamic force characterization 5
- 2.1 Unsteady flows and forces on an object . . . 5
  - 2.1.1 Inline and vertical forces . . . 7
  - 2.1.2 Overturning moment . . . 9
- 2.2 Force coefficients determination . . . 10
  - 2.2.1 Least Squares . . . 10
  - 2.2.2 Weighted least squares . . . 11
- 2.3 Studies on loads on offshore structures . . . 11
  - 2.3.1 Physical model investigations . . . 11
  - 2.3.2 Numerical model investigations . . . 14
- 2.4 Relevance of this thesis . . . 14

3 Experimental data 15
- 3.1 Geometry and scaling . . . 15
  - 3.1.1 The facility . . . 15
  - 3.1.2 Scaling . . . 16
  - 3.1.3 Water depths . . . 16
- 3.2 Test cases . . . 17
  - 3.2.1 Solitary wave tests . . . 17
- 3.3 Measurements . . . 18
  - 3.3.1 Surface elevation measurements . . . 18
  - 3.3.2 Force measurements . . . 19
  - 3.3.3 PIV measurements . . . 21

4 Numerical models 25
- 4.1 OceanWave3D . . . 25
  - 4.1.1 General description . . . 25
  - 4.1.2 Governing equations . . . 26
  - 4.1.3 Domain . . . 27
  - 4.1.4 Convergence study . . . 27
  - 4.1.5 Breaking waves . . . 29
- 4.2 OpenFOAM . . . 29
  - 4.2.1 Governing equations . . . 30
  - 4.2.2 Turbulence modeling . . . 31
  - 4.2.3 Boundary conditions . . . 31
  - 4.2.4 Domain size . . . 35
  - 4.2.5 Convergence study . . . 35
  - 4.2.6 Wave celerity prediction . . . 36

5 Validation of the OpenFOAM model 39
- 5.1 Synchronization . . . 39
  - 5.1.1 Limitation of the synchronization method . . . 39
  - 5.1.2 Links between time axes . . . 40
- 5.2 Laminar simulations . . . 40
  - 5.2.1 Experimental bias and pressure correction. . . . 40
  - 5.2.2 Force estimate . . . 42
- 5.3 Reynolds Averaged simulations . . . 43
  - 5.3.1 The importance of the grid refinement. . . . 43
  - 5.3.2 Force results . . . 45
- 5.4 Comparison with the PIV measurements . . . 46
  - 5.4.1 Synchronization analysis. . . . 47
  - 5.4.2 Observation on the velocity field prediction . . . 48
- 5.5 Summary . . . 50

6 Experimental characterization of the loads for solitary waves 53
- 6.1 Undisturbed velocity . . . 53
  - 6.1.1 Velocity and acceleration from the N-S/VOF solver . . . 54
  - 6.1.2 Differences between OCW3D and OpenFOAM estimate of the undisturbed velocity . . . 55
  - 6.1.3 Characterization of the flow field. . . . 55
- 6.2 Force fits . . . 57
  - 6.2.1 Inline force fits . . . 58
  - 6.2.2 Vertical force fits . . . 58
- 6.3 Coefficients results . . . 60
  - 6.3.1 Inline force coefficients . . . 60
  - 6.3.2 Vertical force coefficients . . . 61
- 6.4 Summary . . . 62

7 Numerical characterization of the loads 65
- 7.1 Additional test cases . . . 65
  - 7.1.1 Additional solitary wave tests . . . 65
  - 7.1.2 Regular waves . . . 66
  - 7.1.3 Characterization of the flow field. . . . 67
- 7.2 Force and moment fits . . . 68
  - 7.2.1 Inline force fits . . . 68
  - 7.2.2 Vertical force fits . . . 68
  - 7.2.3 Centroidal moment fits . . . 70
- 7.3 Coefficients results . . . 73
  - 7.3.1 Inline force coefficients . . . 74
- 7.4 Partition of the structure . . . 74
  - 7.4.1 Vertical force coefficients . . . 78
  - 7.4.2 Centroidal moment coefficients . . . 81
- 7.5 Influence of the discharge. . . . 81
  - 7.5.1 Numerical set-up . . . 81
  - 7.5.2 Force analysis . . . 82
- 7.6 Summary . . . 84

8 Discussion 85
- 8.1 Vertical force and centroidal moment equations . . . 85
- 8.2 Validity of the OpenFOAM model . . . 86
  - 8.2.1 Experimental and numerical reconstruction of the velocity field. . . . 86
  - 8.2.2 Experimental and numerical estimate of the inline force coefficients . . . 86
- 8.3 Comparison with previous works . . . 87

9 Conclusions 89
- 9.1 Recommendations and future works . . . 90

Bibliography 93

A Geometrical properties of the velocity cap 97
A.1 Frontal area 98
A.2 Volume 98
A.3 Center of mass 98

B Irregular wave tests 99
B.1 OCW3D modelling of the irregular wave cases 100

C Preliminary undisturbed velocity estimates 103
C.1 PIV estimate 103
C.2 Analytic estimates of the horizontal velocity 103
C.3 Velocities from the OceanWave3D computations 105

D Implementation of the weighted least squares method for the coefficient fitting 107
D.1 General description of the weighted least squares method 107
D.2 Inline force fitting 108
D.3 System of equations solved for the vertical force 109
D.4 System of equations solved for the centroidal moment 109

E Plots of the forces obtained in the RAS simulations 111

F Numerical coefficients estimates 117
F.1 Inline force coefficients 117
F.2 Partial inline force coefficients 118
F.3 Vertical force coefficients 119
F.4 Centroidal moment coefficients 120

List of Tables

3.1 Measures and features of the flume set-up used in the experiments. 15

3.2 Scale multiplier to transform the model-scale dimensions into the full scale dimensions. 16

3.3 Description of the 9 test cases involving solitary waves. 18

4.1 Specifications of the OCW3D domain. The information are dependent of the water depth considered. Length of the pressure zone at the outlet of the OCW3D domain for the three water depth considered. The computation follow from the dispersion relation and the period is always 10 seconds as contained in the steering files. 27

4.2 POT values and breaking parameter for the 9 soliton test cases. 27

4.3 Overview of the discretization parameter used for the OCW3D computations relative to test T201 and the respective errors. 29

4.4 Overview of the background mesh grid sizes used for the OpenFOAM computations relative to test T101 and the respective errors. 36

4.5 Wave celerity at WHM6 as computed by the model and as obtained from the experimental records. Breaking cases are reported in red. Test case T303 is not considered as a breaking case because the wave was breaking right after the cap, however, the location of breaking is slightly different in physical model tests and in the numerical simulation and this influences the computation of the wave celerity. 36

5.1 Relation between computed and measured results. The relative error between computed and measured forces is expressed in percentage. The results reported in red corresponds to the test cases in which breaking was observed. 46

5.2 Estimate of the overall disagreement (er) between the 7 offsetted PIV velocity maps and the OpenFOAM results. The time directories corresponding to the moments when the wave is passing over the cap are presented. 48

6.1 Dimensionless numbers relative to the 9 test cases involving solitary waves. 57

6.2 Morison coefficients computed from the raw experimental force records. The errors (ϵ) are expressed as a percentage of the computed signal and are estimated as in equation 6.6. 60

6.3 Vertical force coefficients computed from the raw experimental force records. The errors (ϵ) are expressed as a percentage of the computed signal and are estimated as in equation 6.6. 61

7.1 Description of the 7 additional solitary wave cases. 66

7.2 Description of the 5 additional regular wave cases. 67

7.3 Re, KC and β defined for the additional test cases. The KC number relative to the regular cases, already presented in table 7.2, are here repeated for completeness. 68

7.4 Re, KC and β defined for the two components of the velocity cap. 76

7.5 Main dimensions needed to come to the value of the velocity to apply to the pipe outlet. The scale computed between the model used in this thesis and the model used by Christensen et al. (2015) is 1:72.37. 82

7.6 Drag and inertia coefficients computed for the inline load in the case with and without discharge. 84

9.1 Summary of the force and moment coefficients. The minimum maximum and mean value are computed without considering the three test cases for which breaking was observed. 90

B.1 Description of the 9 test cases involving irregular waves. 99

F.1 Inline force coefficients computed from the OpenFOAM records of the inline loads. The coefficients are the drag and inertia coefficients defined as in equation 2.9. The error (ϵ) are expressed as a percentage of the computed signal and are estimated as in equation 6.6. 117
F.2 Inline hydrodynamics coefficients for the two components of the velocity cap. The error ϵ are express in percentage and are computed as in equation 6.6. 118
F.3 Vertical force coefficients computed from the OpenFOAM records of the vertical loads. The reported coefficients are the lift force coefficients C_L as defined by equation 2.11 and the three new coefficients defined by equation 6.3. 119
F.4 Centroiddal moment coefficients defined from equation 7.1. The errors (ϵ) are expressed as a percentage of the computed signal and are estimated as in equation 6.6. 120

List of Figures

1.1 Diagram showing a velocity cap intake structure. 1
1.2 A photograph of the scale model of the cap. 3
1.3 Phases carried out during the present thesis project. 4

2.1 Decomposition of the total force on a cylinder between inertia and drag (Sumer and Fredsøe, 2006). This case describes the case of regular sinusoidal waves. The phasing has been observed to change in case of other 7
2.2 Variation of the drag (top) and inertia (bottom) coefficients versus KC (called K in the original label) for various values of β (source: Sarpkaya (2010)). 8
2.3 Visualization of the moment caused by the inline and vertical forces and of the centroidal moment. 10
2.4 Drag and inertia coefficients versus the KC number. The data are relative to the two configuration studied by Sarpkaya (1979). 12
2.5 Side cross view and plan view of the diffuser structure used by Mogridge and Jamieson (1978) for the physical model tests. 13
2.6 Typical results of the experiements by Mogridge and Jamieson (1978) on a open diffuser-cap type outfall. 13

3.1 Technical drawing reporting the relation between the three water levels tested and the geometry of the cap. For more specification about the geometry of the cap see appendix A. 17
3.2 To scale sketch of the test set-up. The position of the first wave gauge reported in the experiment log is shown in red. The purple lines show the actual positions of the wave gauges (called WHM) that were used to record the water elevation. The small red segment shows the horizontal section of the bed where the cap was positioned. The indication of the distances of the wave gauges are all referred to the center of this red segment corresponding to the center line of the velocity cap. 18
3.3 Measurements of the surface elevation of test T201. 19
3.4 Sketch of the setup of the force sensors. The dimensions are expressed in mm. 19
3.5 Example of the phasing between loads and surface elevation in the case of test T101. The scale factor is 50 for the inline force and 70 for the vertical one. 20
3.6 Peaks of the inline force per every test case (ensemble average) plotted over the measured H/h. In red the symbols relative to the tests that involved breaking. 20
3.7 Peaks of the vertical force per every test case (ensemble average) plotted over the measured H/h. In red the symbols relative to the tests that involved breaking. 21
3.8 Sketch of the PIV set-up. The laser sheet used to light up the particles was parallel to the direction of propagation of the flow. The scaled model of the velocity cap was realized with a strip of transparent material at the center-line (see figure 1.2) so that the laser beam could pass through and light up the particles right next to the lower support cylinder. 21
3.9 Overlapping parts of interrogation areas. The parameter a is the percentage of overlap. 22
3.10 Ensemble-averaged vertical velocity profile for six representative locations in proximity of the velocity cap. The orange line of the estimate obtained with 20 repetitions is often covered by the one the relative to the estimate obtained with 40 repetitions. 23
3.11 Standard deviation of the horizontal velocity plotted over the vertical for the six locations shown in figure 3.10. The white spaces correspond to the locations where no velocity was measured due to the presence of the cap. 23
3.12 Upper panel: plot of the horizontal velocity component at a given moment in time for test T201. The color of every point in the graph corresponds to a value of the velocity (the horizontal component only). Lower panel: plot of the horizontal velocity over the water column for the position highlighted in red in the upper panel (on the far left). 24

3.13 Example of a PIV velocity reconstruction and synchronization with the forces time series for test case T201. The top panel shows the force signals and red vertical line indicates from which instant the velocity field of the lower panel is taken from. Also here the colours in the lower panel correspond to the magnitude of the horizontal velocity. 24

4.1 The geometry of the velocity cap would pose problems with regards to the spatial discretization to simpler flow solvers. In this extremely simplified sketch of the velocity cap, multiple interfaces between bottom (outside of the domain) and numerical domain can be noted along the red dashed line. 26
4.2 Match between experimental measures and computed surface elevation relative to test T201. The plot includes the lines relative to every wave gauge and the line showing the sixth peak in time represents the data relative to the wave gauge at the velocity cap (used later for the force reconstruction). 28
4.3 Different values of the RMSE for different point per cut-off (test case T201). 28
4.4 Match between experimental measures and computed surface elevation relative to test T103. It can be observed that the wave breaks more or less at WHM4 and that the match at the following wave gauges is quite poor. 30
4.5 Visualization of the several patches which are split in for the purpose of the analysis . In red the bottom of the flume and in gray the side wall. 32
4.6 Schematic of the relaxation zone at the inlet and the outlet 33
4.7 Sketch of the domain size and positions of the wave gauges and of the cap in the test cases regarding solitary waves (excl. T103). 35
4.8 RMSE error computed for the different grid sizes of the background mesh (previous to refinement). Result relative to test T101. 36
4.9 Match between surface elevation computed by the N-S/VOF solver and measured for test case T101. Given the dimension of the OpenFOAM domain only wave gauges WHM3, WHM4, WHM5, WHM6 and WHM7 were included. 37

5.1 Relationships between the time axes of the different time series used during this study. 40
5.2 Comparison of the experimental and numerical estimate of the forces for test case T101. Laminar simulation with slip condition applied on the cap patches. Top panel: water surface elevation at WHM 5, 6 and 7. The thicker lines correspond to the surface elevation at the velociy cap (WHM 6). Mid panel: inline force. Lower panel: vertical force. The OpenFOAM plots show the results both including and excluding the force component on the patch of the base plate. This is done because the inclusion of the base plate has only relevance for the validation of the results in terms of comparison with the experimental measurements. In real applications the base plate is not a part of the velocity cap. 41
5.3 Drawing of the gaps between the base of the cap and the rest of the wooden frame constituting the bottom of the flume. The force sensor were water-proof and all the part of the flume below the wooden frame was also filled with water. 42
5.4 Probed points at the location of the sides of the base plate. For each point a time series of the total pressure is output during the simulation. 42
5.5 Pressure field obtained by interpolating linearly the pressure probed at the contour. 42
5.6 Comparison of the experimental and numerical estimate of the forces for test case T101. Laminar simulation with slip condition applied on the cap patches. In this plot the correction is subtracted form the experimental record. The summation of the orange and red curves results in the plot of the original measurements as plotted in figure 5.2. 43
5.7 In line estimate for the breaking test case T203. Laminar simulation with slip condition applied on the cap patches. 44
5.8 Comparison of the experimental and numerical estimate of the forces for test case T101. Slip condition applied on the cap patches. The error between the measurements (corrected) and the model results reaches 16 % at the negative peak of the force. 44
5.9 Visualization of the value of y^+ computed on the cap patches (screen-shot taken from ParaView). Results relative to test case T301. Any dark red point indicates a location where y^+ is above 30. The maximum value computed for this simulation is 52. 45
5.10 Results of the RAS computations for test case T301. 45

5.11 Plot of the computed peak force against the measured one. The red line is included as a reference for the 1:1 line. 46
5.12 OpenFOAM horizontal velocity estimate for test T201. 47
5.13 Ensemble averaged horizontal velocity computed from the PIV measurements relative to the 40 repetitions of test T201. Test case T201 was taken as a reference because the 40 repetitions of the test allowed to have the best estimate of averaged flow field. 48
5.14 Comparison between the PIV and OpenFOAM velocity estimates for test T201 at time 313.6. The PIV velocity map used in the comparison has an offset of 1 frame (-0.033 seconds). Top panels: comparison of the velocity plotted over the vertical for test T201. The x locations where the velocity where taken from 0.125 m in front and after the velocity cap and they are highlighted in the lower panel by red segments. Lower panel: plot of the mismatch between horizontal velocity estimates computed as in eq. 5.3. 49
5.15 Comparison between the PIV and OpenFOAM velocity estimates for test T201 at time 313.6. The PIV velocity map used in the comparison has an offset of 2 frames (-0.066 seconds). Top panels: comparison of the velocity plotted over the vertical. The x locations where the velocity where taken from 0.125 m in front and after the velocity cap and they are highlighted in the lower panel by red segments. Lower panel: plot of the mismatch between horizontal velocity estimates computed as in eq. 5.3. 50
5.16 Comparison between the PIV and OpenFOAM velocity estimates for test T201 at time 313.6. The PIV velocity map used in the comparison is determined using the original synchronization and therefore it has zero offset. Top panels: comparison of the velocity plotted over the vertical. The x locations where the velocity where taken from 0.125 m in front and after the velocity cap and they are highlighted in the lower panel by red segments. Lower panel: plot of the mismatch between horizontal velocity estimates computed as in eq. 5.3. 50
5.17 Comparison between the PIV and OpenFOAM velocity estimates for test T201 at instant 313.4. This frame corresponds to the beginning of the strong flow separation at the top leading edge of the velocity cap. The PIV velocity map used in the comparison has an offset of 1 frames (-0.033 seconds). 51
5.18 Comparison between the PIV and OpenFOAM velocity estimates for test T201 at instant 313.5. This frame corresponds to the moment when the inline load was at its peak. The PIV velocity map used in the comparison has an offset of 1 frames (-0.033 seconds). 51
5.19 Comparison between the PIV and OpenFOAM velocity estimates for test T201 at instant 313.7. This frame show the development of of the flow and of the wakes 0.1 seconds after the crest of the wave has passed the center of the velocity cap. The PIV velocity map used in the comparison has an offset of 1 frames (-0.033 seconds). 51

6.1 Location of the probed velocity. The dimensions are in meters. 54
6.2 Example of the estimate of the velocity and acceleration obtained from the OpenFOAM computations. In the lower panel, a zoomed detail of the upper plot shows more closely the high frequency wiggles observed. 55
6.3 Comparison between the OCW3D horizontal velocity estimate and the solution computed by the N-S/VOF solver. Data relative to test case T201 56
6.4 Example of the computation of the displacement r. Data relative to test case T201. 57
6.5 Force fit obtained for the inline force recorded during test T201. The decomposition between inertia and drag is also shown. 58
6.6 Force fit obtained for vertical force recorded during test T201. 58
6.7 New force fit obtained with equation 6.3. The decomposition of the total load between the 3 components is also shown. The summation of the dashed lines gives the total data relative to test T101. 59
6.8 New force fit obtained with equation 6.3. The decomposition of the total load between the 3 components is also shown. Data relative to test T301. 60
6.9 Force coefficients for the Morison equation plotted over representative parameters for the flow conditions. In these and in the next plots only the results from the tests that did not involve breaking are included. 61
6.10 Vertical force coefficients plotted over the KC number. 62
6.11 Vertical force coefficients plotted over the ratio H/h. 63

6.12 Vertical inertia coefficients (C_{Mz}) plotted over the ratio $W_{0,max}/U_{0,max}$. 63

7.1 Inline force estimate relative to test case T401_1. The signal is affected by high frequency and low intensity oscillations. 66
7.2 Water surface elevation, inline and vertical force computed by the model for test case R1. In the top panel the surface elevation probed at the location of the 5^{th}, 6^{th} and 7^{th} wave gauge is shown. 67
7.3 Water surface elevation, inline and vertical force computed by the model for test case R5. As in the previous figure, the surface elevation probed at the location of the 5^{th}, 6^{th} and 7^{th} wave gauge is shown in the top panel. 67
7.4 Fit of the inline force for test case R1. The biggest part of the load is determined by the inertia. . 69
7.5 Fit of the inline force for test case T201. Here both drag and inertia are playing a role for determining the amplitude of the inline force peak. 69
7.6 Fit of the vertical force obtained with the original lift force equation 2.11 for test case T201. . . . 70
7.7 Fit of the vertical force obtained with the modified vertical force equation 6.3 for test case T201. The decomposition between the three components that build up the total force are also shown in dashed lines. 70
7.8 Fit of the vertical force obtained with the original lift force equation for test case R5. 71
7.9 Fit of the vertical force obtained with the modified vertical force equation for test case R5. The four force components estimated are also shown. 71
7.10 Comparison between the overturning moment for test T202 computed by the N-S/VOF solver around the center of mass (M_{CoM}), around point O at the base of the structure (see drawing 2.3, M_O) and as computed with the equation 2.12 ($M_{f,O}$). 72
7.11 Comparison between the moment for test R3 computed by the N-S/VOF solver around the center of mass (M_{CoM}), around point O at the base of the structure (see drawing 2.3, M_O) and as computed with equation 2.12 ($M_{f,O}$). 72
7.12 Fit of the centroidal moment obtained for test case R3. 73
7.13 Fit of the centroidal moment obtained for test case T202. 73
7.14 Inline force coefficients plotted against the KC number. 74
7.15 Inline coefficients versus the ratio H/h. 75
7.16 3-dimensional sketch of the locations from which the velocity used for the computation of the partial coefficient was extracted. The dimensions are in meters. 75
7.17 Force decomposition for the two parts of the velocity cap. 76
7.18 Drag and inertia coefficients for the support cylinder of the velocity cap plotted over the local KC number. Given that the diameter of the cylinder is smaller than the one of the top part the values of KC are always bigger. 77
7.19 Drag and inertia coefficients for the top part of the velocity cap plotted over the local KC number. 77
7.20 Force fit for the inline component acting on the support cylinder of the velocity cap. Data relative to test case T301. 78
7.21 Force fit for the inline component acting on the top part of the velocity cap. Data relative to test case T301. 78
7.22 Horizontal drag coefficient versus the KC number. 79
7.23 Vertical drag coefficient (C_{Lz}) versus the KC number. 79
7.24 Vertical inertia coefficient (C_{Mz}) versus the KC number. 79
7.25 Horizontal drag coefficient versus the dimensionless wave height H/h. 80
7.26 Vertical drag coefficient (C_{Lz}) versus the eccentricity of the orbital motion expressed by the parameter $W_{0,max}/U_{0,max}$ 80
7.27 Vertical inertia coefficient (C_{Mz}) versus the eccentricity of the orbital motion expressed by the parameter $W_{0,max}/U_{0,max}$. 80
7.28 Centroidal moment coefficients versus the KC number. 81
7.29 Longitudinal cross-section at the center-line of the new geometry used during a simulation. The red arrows have a dimension proportional to the velocity of the water. At instant depicted in the figure no wave has arrived at the velocity cap yet. 82
7.30 Inline and vertical force for test case T201. The results with and without discharge are plotted together. The simulated time interval extends from second 309.5 until second 315 83
7.31 Inline and vertical force for test case R3. The results with and without discharge are plotted together. The entire simulated time interval is plotted. 83

8.1 Comparison of the inline force coefficients plotted over KC for the six test cases simulated both in physical and numerical model tests. The experimental values are obtained with the corrected force signals (exp. corrected). 87

A.1 Front view of the velocity cap. 97

B.1 Example of the phasing between loads and surface elevation in the case of test JS101. The scale factor is 50 for both the inline and vertical force. 100
B.2 Plot of the maximum inline force due to a single wave for all the nine tests involving irregular waves. 100
B.3 Plot of the maximum uplift due to a single waves. 100
B.4 Surface elevation at the sixth wave gauge as measured during the experiments and as computed by the potential flow solver. Data relative to test case JS102. 101

C.1 Plot of the horizontal velocity approximately 31 cm in front of the cap, at the height of 0.116 m above the floor. Data relative to the ensemble-averaged results obtained from the 40 repetitions of test T201. 104
C.2 Comparison of the first two attempts to compute the undisturbed velocity with the records extracted from the PIV measures. The result of the eq. by Svendsen and Jonsson (1980) dependents of the depth and is plotted in multiple lines. The fraction of water column for which the relative velocities are plotted is the height of the velocity cap above the bottom (16.7 cm). 106
C.3 Comparison of the results for the horizontal velocity at the position of the cap from the first computation attempted, from the PIV measurements and from the OCW3D model. 106

Nomenclature

Abbreviations

CoM	Center of mass
OCW3D	OceanWave3D
PIV	Particle image velocimetry
ppc	Points per cut-off
RAS	Reynolds Averaged Simulation
VOF	Volume of Fluid
WHM	Wave height meter or wave gauge

Symbols

α	Scalar field used to track the free surface in OpenFOAM$^{®}$	[-]
β	Frequency number or Sarpkaya β	[-]
η	Free surface elevation measure from still water level	$[m]$
κ_γ	Surface tension coefficient at 20 °C	0.074 $[kg/s^2]$
μ	dynamic molecular viscosity	0.001 $[kg/(ms)]$
ν	Kinematic viscosity of water	1e-6 $[m^2/s]$
ω	Specific rate of turbulent energy dissipation	$[s^{-1}]$
$\overrightarrow{u_0}$	Vectorial notation of the undisturbed velocity field. $\overrightarrow{u_0} = (U_0, W_0)$	$[m/s]$
ρ	Density of water	1000 $[kg/m^3]$
σ_T	Specific Reynolds stress tensor	
τ_w	Wall shear stress	$[N/m^2]$
ξ	Tuning coefficient for the wave celerity defined in the Sommerfeld condition	[-]
A	Frontal area of the cap	$[m^2]$
a	Amplitude of a regular wave motion	$[m]$
br	Breaking criterion (defined according the formulation implemented in OCW3D)	[-]
C_D	Drag coefficient	[-]
C_L	Lift coefficient	[-]
C_M	Inertia coefficient	[-]
C_{Lx}	Horizontal drag coefficient for the vertical force equation	[-]
C_{Lz}	Vertical drag coefficient for the vertical force equation	[-]
C_{Mx}	Vertical drag coefficient for the vertical force equation	[-]
Fr	Froude number	[-]
g	Acceleration of gravity	m/s^2
H_S	Significant wave height	$[m]$

k	Turbulent kinetic energy	$[m^2/s^2]$
KC	Keulegan-Carpenter number	[-]
KC_s	Keulegan-Carpenter number for solitary waves, following the definition by Chian and Ertekin (1992)	[-]
$M_{f,O}$	Moment determined by inline and vertical forces around a generic center of rotation O	$[Nm]$
p^*	Pressure in excess of the hydrostatic	$[N/m^2]$
r	Total excursion of the fluid particle under the action of a solitary wave	$[m]$
Re	Reynolds number	[-]
U_0	Horizontal component of the undisturbed velocity	$[m/s]$
u_τ	Friction velocity	$[m/s]$
V	Volume of the cap	$[m^3]$
W_0	Vertical component of the undisturbed velocity	$[m/s]$
y^+	Non-dimensional wall distance	[-]

1

Introduction

1.1. Context

Different infrastructures such as a desalination plant or a nuclear power plant, share the feature that they all need a relatively constant discharge of water that is collected from a source, which in many cases is the sea.

One of the intake structures that can be used for this purpose is the so-called velocity cap. These intakes are open seafloor founded constructions mounted at a sufficient water depth and connected to a pipe or a tunnel generally called intake conduit. The particular shape of modern caps derives form the patent of Larson and Downs (1975) and it prevents the formation of a whirlpool from the surface. The collocation of the vents at a certain height over the seafloor makes sure that both floating debris and sediments at the bottom are not discharged together with the water. At the end of the intake conduit the water is collected in a sump where a pump finally sends it to the location of utilization (Pita and Sierra, 2011). Figure 1.1 gives an overview of a typical layout of a velocity cap.
In the case of a power plant the water is then pumped up to the cooling system. For this application, the structure of the velocity cap often has the specific aspect sketched in figure 1.1 and it is typically located 1 to 5 km offshore, in water depths ranging from 10 to 20 meters. In particular, in the case of nuclear power plants, the cooling system assumes importance with regard to human safety as the notorious nuclear accident of Fukushima testifies. In that case, the combined damages to the power supply and to the cooling system caused the meltdown of the three cores (World nuclear association, 2018).

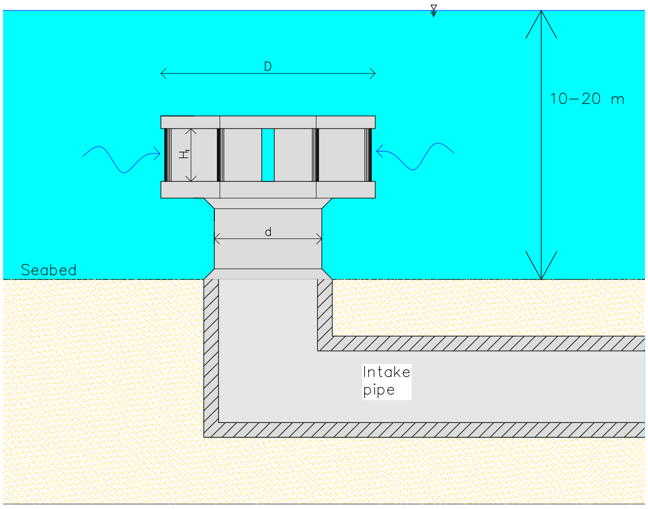

Figure 1.1: Diagram showing a velocity cap intake structure.

In coastal regions, these structures are subject to the offshore environment, which brings about particular design loads. A submerged structure founded at the bottom of the sea will be subject to the forces originating from the surrounding flow field. Without considering geotechnical or other external aspects (such as, for instance, landslides or collision with objects), two main phenomena can generate loads on a velocity cap: currents and waves.

Marine currents can be generated by long period waves such as tides and tsunamis and they can be modelled as a sequence of steady states. The loads generated by steady state currents, however, are not analyzed in this thesis.
Sea waves are mostly described as an irregular field of wind waves fully characterized by a spectrum. The design rules of offshore structures around the world generally take into account the loads generated by these types of waves but for particular locations, such as for instance the Pacific coast of the Asian continent, the loads caused by tsunamis must also be considered. Tsunamis are long period waves that often behave as fast tides inducing relatively fast water level changes and strong currents. In shallow, mildly sloping foreshores, the tsunami wave can shoal and increase its amplitude and steepness resulting either in a solitary wave or, after breaking, in a turbulent bore (Glasbergen, 2018).

In common engineering practice the design loads are often determined by desk studies which follow relatively simple models such as the Morison equation (Morison et al., 1950) or by physical model testing. In case of more complex numerical investigations, the focus has been mostly on simpler shapes (for instance a cylinder, see Paulsen (2013)), while the geometry of the velocity cap has been analyzed only seldom (Christensen et al., 2015).

The present thesis has the aim to derive hydrodynamic force and moment coefficients for the loads on the velocity cap and to validate a numerical CFD tool against experimental evidence for the simulation of laboratory wave condition on this specific geometry. This tool is also used to analyze the differences between the loads generated by solitary waves and regular waves. Regular waves in this context are studied as a simplification of real wind waves and are used to draw conclusion on the nature of the loads on such a structure.

1.2. Physical model tests at Deltares

The knowledge institute Deltares has already investigated by means of physical model tests the loads due to irregular waves on the specific geometry of a velocity cap. In 2017, an additional experimental campaign was carried out with the specific aim of modelling the effect of particular types of waves passing above the cap. The two types of waves that were tested are irregular waves (JONSWAP spectrum) and solitary waves (or solitons). The second typology was analyzed with greater detail and the total number of tests involving solitary waves was much bigger than the one involving irregular waves. Solitons have already been used in the past for modelling tsunamis (Madsen et al., 2008) and the aim of the experimental campaign was to collect data relative to the loads generated by those waves passing or breaking over the velocity cap.

The data-set relative to those experiments consists of measurements of the surface elevation and the forces on the cap and, for some tests of PIV measurements as better described in chapter 3. Part of this thesis project is strongly related to that experimental campaign, because it presents and analyzes the outcome of the campaign. As explained in more detail in section 1.3, the addition of this thesis regards the validation of a CFD model and its utilization to characterize the forces on the cap with more detail and to draw conclusions on the relevance of solitary waves compared to regular waves for the design loads of these structures.

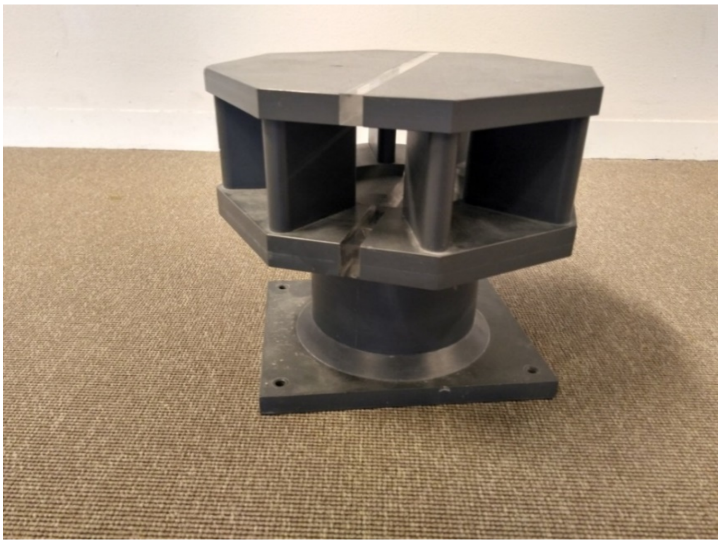

Figure 1.2: A photograph of the scale model of the cap.

1.3. Research question

Having seen the nature of the physical phenomena under analysis and having taken into account how the geometry of a velocity cap was studied in the past, the main research question for this thesis is formulated as:

"How to characterize the forces on a submerged velocity cap in unsteady flows?"

To better explain the path that is followed to answer the main research question, the three following subquestions are formulated:

1. *What are the characteristic flow features with regards to turbulence and to ensemble averaged flow field along the center-line of a velocity cap under unsteady flow (solitary waves)?*
   The availability of PIV measurements on the center-line of the cap for the solitary wave test cases allows an analysis of the velocity field around the velocity cap.
2. *How to characterize the forces and the turning moment on a velocity cap under different types of wave loads by means of the Morison, lift force and the turning moment equation models?*
   The characterization of the loads consists in the derivation of the force coefficients of the relative force or moment equations.
3. *To what extent can the loads and the flow field be reproduced with a detailed CFD model?*
   The calibration and validation of a CFD model using the open-source library OpenFOAM is the most complex objective of this thesis and it is treated in several steps.
   At first, the records of the forces on the velocity cap and water surface elevation and the velocity profiles extracted from the PIV dataset are compared with the results of the numerical model.
   Secondly the numerical estimate of the forces and overturning moment are used to to define force and moment coefficients for several scenarios of KC number and for different types of waves.
   Lastly, the validated numerical model is used to model the case in which the velocity cap is discharging water to an utilization point in the presence of wave loads. The effect of the additional discharge through the cap is addressed only briefly to point out the differences between the loads studied in this analysis and more realistic working conditions.

1.4. Thesis structure

The objective of this thesis is to provide a study of the loads on the velocity cap supported both by experimental evidences and numerical simulations. The experimental and numerical investigations run parallel in this thesis as described in diagram 1.3. The multiple connections between the two are depicted by the horizontal arrows.

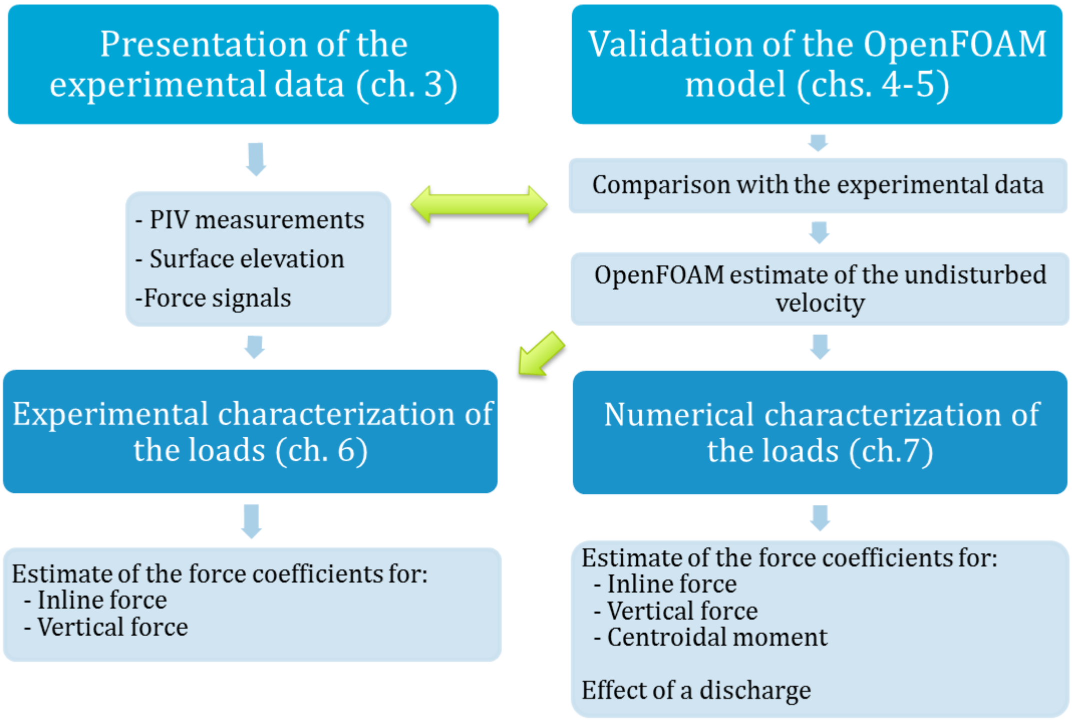

Figure 1.3: Phases carried out during the present thesis project.

After having presented the concepts and the knowledge gained during the literature study in chapter 2, the thesis proceeds in chapter 3 with the presentation of the set-up of the physical model tests and the experimental data collected during the campaign. This data are then used to calibrate and validate the two numerical models used in this thesis and presented in chapter 4: Oceanwave3D (potential flow solver) and OpenFOAM (open-source library for computational fluid dynamics).
The numerical part of the investigation is based on the output of the OpenFOAM model. Therefore, in chapter 5 particular attention is dedicated to the validation of this model. The experimental data presented in chapter 3 are here compared with the output of the model and the observed mismatch are discussed.

The velocity estimate probed in the CFD domain during the numerical simulation is then used in the Morison and vertical force equations to fit the experimental and numerical force signal and to obtain the values of the force coefficients.
The fits and the coefficients obtained are presented in chapter 6 for the experimental force records and in chapter 7 for the numerical force records. Given the capabilities of the OpenFOAM model, in the case of the numerical analysis the overturning moment is also studied.
Additionally at the end of chapter 7, the effect of a discharge passing through the velocity cap is modelled in OpenFOAM and the main results are presented.

Eventually the last two chapters (ch. 8 and ch. 9) present a critical reflection on the significance of the findings and a summary of the answers to the research questions respectively.

2

Literature review on hydrodynamic force characterization

The forces on the intake cap described in the introduction have been studied by means of physical model tests and numerical simulations. What is missing however is a complete characterization of the forces by means of force coefficients and a study on the dependency of these on relevant parameters. This chapter presents the common approaches used to define and characterize the loads on the structures benefiting from publications regarding loads on cylinders and bridge decks as well as intake or diffuser caps.

In the first part of this chapter, the theory used in literature to analyze the loads in unsteady flow on offshore structures is presented. The loads that are analyzed are linear forces (inline and lift) and turning moment. Furthermore a description of the mathematical method used to derive the force coefficients is also given.
At the end of the chapter, examples of analysis of wave loads are presented. In the reviewed literature, the concepts described in the first part have been used to determine force and moment coefficients, both in experimental set-ups and numerical simulations.

2.1. Unsteady flows and forces on an object

The flow field generated by any type of wave motion (excluding tides or other very long period waves) is unsteady. Sumer and Fredsøe (2006) carried out a study of the possible flow regimes in both steady and oscillatory state around a cylindrical object. Cylinders are of big importance for the offshore industries and in the present thesis the formulas generally used for cylindrical objects are adapted and applied to the shape of the velocity cap in order to assess their validity.

The classification of the flows in the oscillatory situation is done by recalling the notion of Reynolds number (Re), the Keulegan-Carpenter number (KC) and their ratio (β). Re describes the ratio between the inertial forces and the viscous force acting on the flow and it is defined as:

$$Re = \frac{DU_{0,max}}{\nu} \tag{2.1}$$

In this expression, D is a representative length for the flow field (in case of the hydrodynamics around a cylinder it is generally assumed equal to the diameter of the cylinder), ν is the kinematic viscosity and $U_{0,max}$ is the maximum horizontal velocity undisturbed by the presence of the object.

In the case of an oscillatory flow, however, Re is not able alone to classify completely the flow and it is generally paired with KC defined as:

$$KC = \frac{U_{0,max}T}{D} \tag{2.2}$$

Where T is the period of the oscillation. In the case of a perfectly sinusoidal wave, it holds that

$$U_{0,max} = \frac{2\pi a}{T} \tag{2.3}$$

Where a is the stroke of the wave motion. In this way the KC number for the sinusoidal case can be written as

$$KC = \frac{2\pi a}{D} \tag{2.4}$$

From this last formulation it is clear that the KC number gives information on the ratio between the oscillatory motion of the water and the dimension of the object immersed in the flow. A large KC number means that the object is small compared to the excursion of water particles during each half-period. In the case analyzed by Sumer and Fredsøe (2006), $KC > 7$ means that the flow is in shedding regime. In that situation, the vortexes that form behind the cylinder in every half period (feature already observed for KC >1.6) start shedding in the downstream part of the cylinder determining an oscillation in the force on the object both in the stream-wise and cross-flow direction.

The formulation of the KC number of eq. 2.2 can be applied also in the case of irregular waves simply assuming that T is a representative period of the wave spectrum. In the case of solitary waves, instead, Chian and Ertekin (1992) reported a different definition of the KC number that is indicated in this thesis with the subscript 's':

$$KC_s = \frac{r}{D} \tag{2.5}$$

$r(t) = \int_{-\infty}^{t} U_0 dt'$ is the total excursion of the fluid particle when the wave is passing, t the time needed to the wave to pass and t' is written with a prime to indicate the time axis and not to generate confusion with the extremes of the integration. In this case the quantity $r(t)$ describes a linear motion only along a line parallel to the x-axis. This definition assumes that the vertical motion of the water particle is negligible. In the solitary waves analyzed in this thesis, this is not considered an appropriate assumption. Especially for the sake of comparison between regular waves and solitons, the definition of KC number for solitary waves is modified. If, in a simplified approach, the total excursion r is posed equal to $2a$ (horizontal excursion in case of a sinusoidal wave) it is easy to see that:

$$KC = \frac{2a\pi}{D} = KC_s\pi \tag{2.6}$$

Therefore in the present study, the KC number for solitary waves is computed according to equation 2.6.

The last dimensionless parameter is known as the frequency number or Sarpkaya β (Sarpkaya, 2005) and is defined as the ratio between Re and KC. Dividing eq. 2.1 and eq. 2.2 it is possible to write this parameter as:

$$\beta = \frac{Re}{KC} = \frac{D^2}{\nu T} \tag{2.7}$$

The parameter β can be interpreted as the frequency of the oscillation that determines a specific flow regime. A given KC, in fact, can be obtained with a high-amplitude, slow oscillation (low u_{max} and high T) or with a short amplitude, fast oscillation (high u_{max} and small T).

The main features of the flow analyzed in this thesis can be well captured by the last two dimensionless number (KC and β). The results of the study are therefore presented according to the classification made through these parameters.

2.1.1. Inline and vertical forces

MORISON EQUATION

In many engineering publications, the characterization of the inline forces on the cylinder in the case of the oscillatory flow follows the concept of the Morrison equation (see for example Sarpkaya (2010), Sumer and Fredsøe (2006), Journée and Massie (2001) and Burrows et al. (1997)). This formula defines the inline total force per unit height as composed by a drag force varying with the square of the velocity and an inertia force varying with the acceleration. Figure 2.1 is taken from Sumer and Fredsøe (2006) and it represents how the force is decomposed in an drag and inertia component in the case of regular waves.

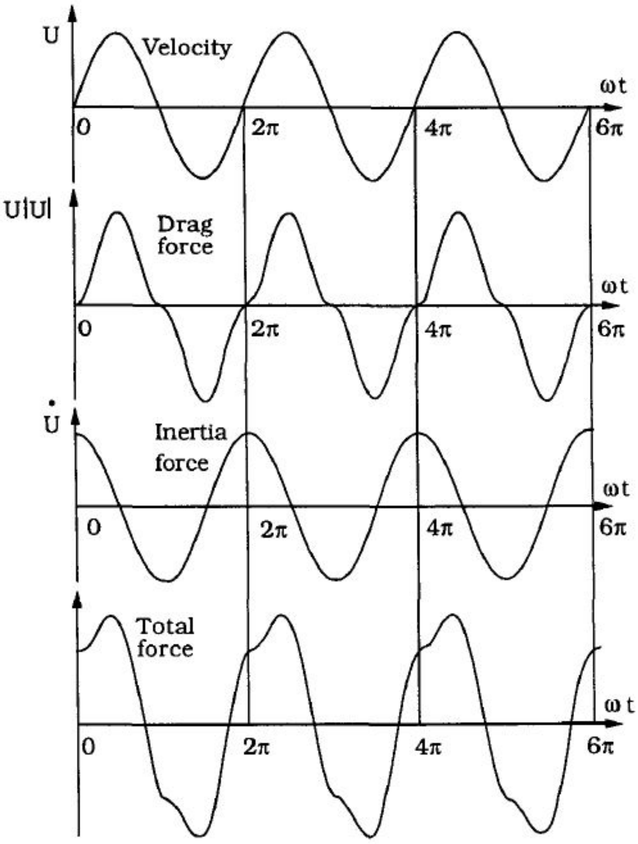

Figure 2.1: Decomposition of the total force on a cylinder between inertia and drag (Sumer and Fredsøe, 2006). This case describes the case of regular sinusoidal waves. The phasing has been observed to change in case of other

The original equation by Morison et al. (1950) was defined for cylindrical objects extending from the bottom up to above the water surface, held stationary under the action of waves. For its determination the assumptions were that the waves needed to be not too steep and the cylinder diameter small compared to the wave length.

Sarpkaya (2010) already highlighted the limitations of the Morison equation in case of steep, nonlinear waves and when flow separation is particularly severe. However the author also pointed out that attempts in finding a better formula for estimating the force history for oscillatory flows have not produced satisfactory results.

If the coordinate system used is such that the inline component is on the the x-direction, the Morison equation is written as:

$$F_{x,cyl} = \frac{1}{2}\rho C_D D U_0 |U_0| + C_M \rho A \frac{\partial U}{\partial t} \tag{2.8}$$

In this equation, $F_{x,cyl}$ is the inline force per unit height, ρ is the density of the water, U_0 is the undisturbed velocity (as it would be measured in absence of the object), A is the cross-sectional area of the cylinder, C_M is the inertia coefficient and C_D the drag coefficient. In particular, C_M and C_D are proven to depend on many parameters such as the geometry of the object, the Keulegan-Carpenter number (KC) and the frequency number (β).

In the work by Sumer and Fredsøe, it was observed that small KC numbers ($0 < KC < 20-30$) are linked to inertia-dominated situations. If the particle motion is small compared to the dimension of the object, in fact, the drag component of the total inline force is negligible compared to the inertia term. On the contrary, when the KC number increases the inertia component was observed to decrease while the drag was becoming more important. The extreme situation of infinite KC can be thought as a stationary flow in only one direction, situation in which the inertia does not play any role at all.

With regards to the estimation of the force coefficients, a theoretical and an experimental method can be pursued.
In the theoretical approach, also known as asymptotic theory (Sumer and Fredsøe, 2006), potential-flow theory is used at first to define the inline load on the cylinder. Subsequently, the oscillating boundary layer on the surface of the object and the perturbation due to this on the outer flow is computed. The final in-line force computed is therefore induced by the perturbed potential flow plus the boundary layer shear stress. The expression of the obtained inline force can be used to derive analytic formulas for the the drag and inertia coefficients.

Experiments show that this theory is valid only for low value of KC (below 1.6 approximately) and low values of β ($\sim O(10^3)$) which correspond to a situation where the flow remains attached (Sarpkaya, 1986). For higher values of KC and β, setting up experiments or a detailed CFD model is necessary to find an estimate for the coefficients.
The experimental results by Sarpkaya (2010) give a picture of the dependency of the inline force coefficients of KC and β for the case of a single cylinder in a harmonically oscillating flow. His research was carried out in a U-shaped water tunnel and the coefficients were obtained by means of Fourier averaging equations. Figure 2.2 shows the dependency of the Morison coefficients for several values of β as a function of KC. In the left-hand part of the lower graph of the figure, the constant value of $C_M = 2$ for all values of β is in agreement with what is found theoretically. The drag is instead totally different from what found in theory.

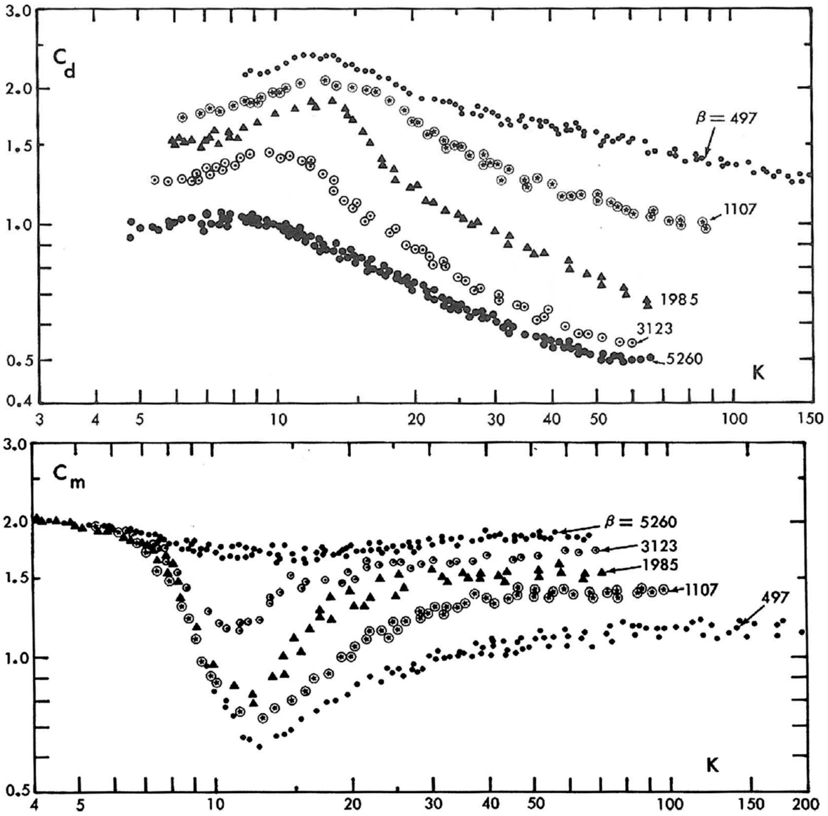

Figure 2.2: Variation of the drag (top) and inertia (bottom) coefficients versus KC (called K in the original label) for various values of β (source: Sarpkaya (2010)).

In this thesis, the characterization of the inline force on the velocity cap follows the approach of the Morison equation, despite its original formulation for cylindrical objects. In the case of the complex geometry, these equations is not expressed per unit height. Considering the total force on the object, the formulas are now written:

$$F_x = \frac{1}{2}\rho C_D A U_0 |U_0| + C_M \rho V \frac{\partial U_0}{\partial t} \tag{2.9}$$

In this formula A is the frontal area of the velocity cap and V is the volume of the cap[1].

Sumer and Fredsøe (2006) analyzed also the influence of diffracting waves on the inertia component of the inline force. It was observed that when the ratio D/L (D= diameter of the cylinder and L= wavelength) becomes larger than 0.2, the waves start diffracting around the cylinder. This influences the inertia coefficient C_M and it introduces a phase lag of the inertial component of the force (Sumer and Fredsøe, 2006). For the present application, the ratio D/L shall be defined to assess whether the diffraction effect must be taken into account.

VERTICAL FORCE EQUATION

Besides the inline force the structure experience also a vertical component. This force, in a way, can be thought as the cross-flow component of the drag force and may be written in the following form:

$$F_{z,cyl} = \frac{1}{2}\rho C_L D U_0^2 \tag{2.10}$$

It has to be noted that the lift force, in the formulation followed here, is still a function of the undisturbed stream-wise velocity squared. $F_{z,cyl}$ is again defined per unit height and C_L is the lift force coefficient.
Other formulations can be found in literature that link the lift force to the undistrubed vertical velocity and the vertical acceleration only. The obtained formula is identical to the Morison equation but defined along the vertical. However in the present study, it was preferred to start the analysis with the traditional lift force equation in order to define coefficients that are more often used in literature and during a design.

Adjusting the formula for the more complex geometry of the velocity cap, the used equation reads:

$$F_z = \frac{1}{2}\rho C_L A U_0^2 \tag{2.11}$$

2.1.2. Overturning moment

The last type of load analyzed is the turning moment. In the case of a structure as slender as the intake cap, it can be expected that overturning might be taken into account for the design verification.

In case of structures subject to dynamic loads caused by the motion of a fluid, the moment can be studied looking at two contributions. In first place, if an estimate of the inline and vertical forces is known, the moment around a point O different from the center of mass (CoM) can be determined by the cross product between the force vector acting ideally on the center of mass of the structure and the arm vector which connects this point and the considered center of rotation. This component can therefore be written as:

$$M_{f,O} = \vec{F} \times \overrightarrow{C_{oM}O} \tag{2.12}$$

By definition, $M_{f,O}$ is equal to 0 when the center of rotation considered is the center of mass. This approach is only based on the estimates of the vertical and inline force and it offers the advantage of simplicity. However, this computation does not give a total estimate of the moment. In fluid dynamics in fact, the center of mass of the structure and the center of pressure in a flow field do not always coincide. In other words, this approach can be too simplistic in some cases, because of the complex pressure distribution on the structure when the wave is passing.

---

[1] More information on how these two constants are defined are included in appendix A

A second component is the moment around the centroid, which can be estimated with more complex techniques such as CFD simulations. This moment, also known as pitching moment, is determined taking into account the distribution of pressure on the surfaces of the structure and its evolution in time. Such estimate can then be related to the undisturbed velocity U_0. In studies regarding bridge design, such as in Kornel Kerenyi and Guo (2009), the pitching moment is determined by the formula:

$$M_{C_{oM},bridge} = \frac{1}{2}\rho C_{mom} U_0^2 (LW^2) \tag{2.13}$$

L indicates the span of the bridge girder and W is its width. The flow is generally assumed to be perpendicular to the length of the bridge. In other publications, the moment is expressed per unit length and L is taken out (Wei Zhang, 2011).

In the case of a submerged cap the proposed formula resembles equation 2.13 and it expresses the total centroidal moment on the structure as:

$$M_{C_{oM}} = \frac{1}{2}\rho C_{mom} U_0^2 (AD) \tag{2.14}$$

The geometrical constants are here the frontal area A and the main diameter D.

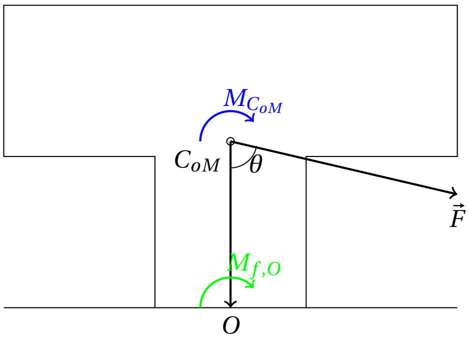

Figure 2.3: Visualization of the moment caused by the inline and vertical forces and of the centroidal moment.

Extending the analysis to the centroidal moment allows to derive information with regards to the rotation of the velocity cap which cannot be obtained by the estimate of the inline and vertical forces only. The turning moment equation 2.14 is defined in a way that captures the moment due to the specific geometry of the structure and pressure distribution in presence of a flow. The total overturning moment $M_{tot,O}$ around a point of rotation O is then determined by the summation between the component $M_{f,O}$ and the centroidal moment M_{CoM} as in equation 2.15.

$$M_{tot,O} = M_{f,O} + M_{CoM} \tag{2.15}$$

2.2. Force coefficients determination

Several force fitting techniques are documented in literature for the determination of the coefficients presented in the previous section (see for instance Journée and Massie (2001)). When time series of the velocity and of the forces are available the most commonly used methods are the least squares method and the weighted least squares method. Examples of the application of the these methods can be found in Chakrabarti (1981), in Hur and Mizutani (2003) and in Hecimovich (2013). In this thesis, the second method is used.

2.2.1. Least Squares

Knowing the geometrical properties of the object under analysis, the determination of the coefficients is possible if the velocity and of the measured forces are known as a function of time. In this case, it is possible to set an over-determined system of equations, solving which the force coefficients can be found. The number of equations corresponds to the number of time-steps in the time window. In offshore engineering this fitting technique is mostly used for determining the coefficients of the Morison equation which has 2 coefficients. It is important to note, however that theoretically the number of coefficients of the fitting equation can be any, provided that the system of equations remains determined.

The specific description of the system of equations obtained as well as the procedure to find the coefficients can be found in appendix D.
For any system specified, the only unknowns are the force of moment coefficients and the systems can be solved directly.
One approach to solve the system is to use the regular least squares method, which minimizes the error obtained as:

$$\epsilon^2 = \frac{1}{N}\sum_{i=1}^{n}\left[F_{fit}(t_i, C_D, C_M) - F_{exp}(t_i)\right]^2 \tag{2.16}$$

where N is the number of time steps considered.

In order to minimize the error, this expression is derived with respect to the unknown C_D and C_M ($\partial\epsilon^2/\partial C_D$, $\partial\epsilon^2/\partial C_M$) and the derivatives are set to zero to find explicit formulas for the unknowns.

2.2.2. Weighted least squares

A variation of the least squares method is the weighted least squares method. The aim of this method is to give a better fit of the force peaks than the original version. Wolfram and Naghipour (1999) performed an exhaustive comparison of several methods of force signal fitting and their conclusion was that the weighted least square method provided the best fits for determining Morison force coefficients.

The error that is minimized in this approach puts extra attention on the experimental force time series and it reads

$$\epsilon^2 = \frac{1}{N}\sum_{i=i}^{n}\left[[F_{fit}(t_i, C_D, C_M) - F_{exp}(t_i)]^2 * F_{exp}(t_i)^2\right]$$

Based on the conclusions by Wolfram and Naghipour (1999), it is preferred to base the estimation of force coefficients on this second method.

The formulas for the force coefficients are derived following the same approach as for the regular least squares ($\partial\epsilon^2/\partial C_D$ and $\partial\epsilon^2/\partial C_M$ set equal to zero to find explicit formulas for the unknown).

In chapter 6 and 7, it is shown that the fitting equations described in the previous section do not provide good fit to the force and measurements signals. Therefore new force and moment equations are proposed and the formulation of the least squares method is adjusted.

2.3. Studies on loads on offshore structures

The theory described in the previous sections is often used in engineering practice to determine the loads on offshore structures. This can generally be done with desk studies (see for example Mogridge and Jamieson (1978) and Capel (2012b)) or with physical model tests (see for example Mogridge and Jamieson (1978) and Cornett et al. (2015)). Besides this approach however, the increasing computational power of modern computers made possible to solve numerically the equations of motion of fluid bodies in relatively large domains. This is the field of computational fluid dynamics (CFD) and examples of application of CDF models can be found in literature (see for example S. Kiran Raju et al. (2014) or Christensen et al. (2015)).

2.3.1. Physical model investigations

BUNDLE OF CYLINDERS

After the publication by Morison et al. (1950), many experimental studies have been performed in order to shed some light on the values of the relative coefficients and their dependency on several parameter describing the flow regimes, the roughness of the cylinder and the proximity of the cylinder to a wall. In the panorama

of the publications analyzed for this thesis, the work by Dr. Turgt Sarpkaya throughout a number of papers and books is remarkable (see Sarpkaya (1979), Sarpkaya (1986), Sarpkaya (2005) and Sarpkaya (2010)).
In particular, in Sarpkaya (1979), the author carried out experiments that involved a circular array of cylinders and a central pipe. The aim of his research was to assess the effect of such a set-up on the force coefficients for *KC* number bigger than 12-15. The interaction of the wakes of the several cylinder was studied varying the diameter of the cylinders in the outer circle and by computing total coefficients for the whole system. It was shown that the drag coefficient correlates negatively with *KC* while the inertia coefficient positively. It was also observed that the value of the inertia coefficient was considerably higher than the values found for a single cylinder. The reason for the high values of the inertia coefficient was linked to the fact that the bundle of cylinders traps a volume of fluid between them and as a consequence the added mass of the system increases (see figure 2.4). The relevance of this findings for the present application lies on the fact that the shape of the intake cap analyzed here consists of a support cylinder and of a top part composed by two horizontal plates and a set of support columns. Therefore, even if the focus here is on a different geometry, the values of the coefficients from the studies from Sarkpaya were used to assess how this work relates to the previous knowledge regarding cylinders.

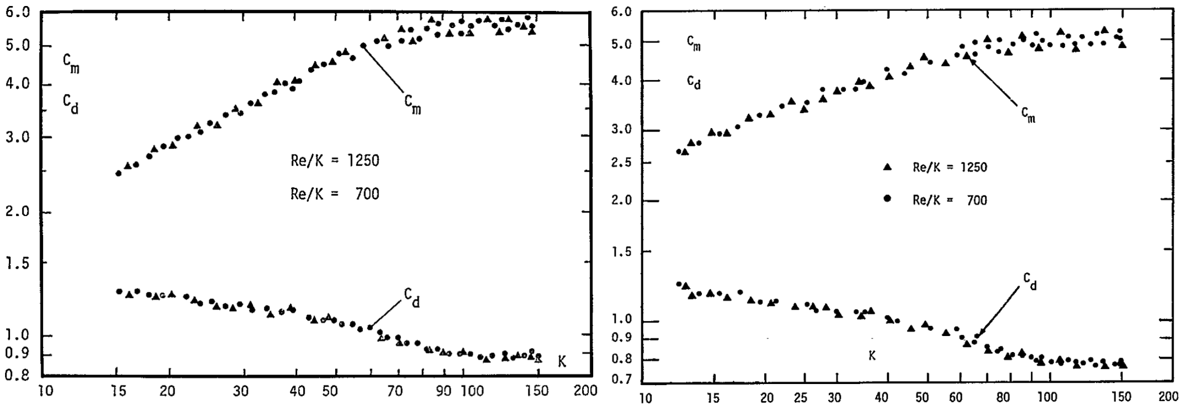

Fig. 2a - Drag and interia coefficients versus K for configuration - I.

Fig. 2b - Drag and interia coefficients versus K for Configuration - II.

Figure 2.4: Drag and inertia coefficients versus the *KC* number. The data are relative to the two configuration studied by Sarpkaya (1979).

DIFFUSER AND INTAKE STRUCTURES

Besides for cylindrical shapes, the approach of the Morison equation has already been tested in experimental campaigns also for the more complex shape of intake or diffuser caps.

Mogridge and Jamieson (1978) analyzed the effect of regular and irregular, breaking and non-breaking waves on a diffuser-cap type outfall attached to the seabed (shown in figure 2.5). The physical model results were compared with the results from the linear numerical diffraction theory, which was applied to the case of a closed cylinder sealed to the bed with size similar to the outer diameter of the diffuser structure. The study showed that there were indeed some differences in the behaviour of the loads (inline and lift force were studied as well as the turning moment) both with regards to the phasing between the loads and the respective amplitudes. In particular with respect to the phasing, it was noted that the peaks in horizontal force and turning moment occur in both cases at approximately the mean water level that precedes the wave peak. The maximum uplift, however, was observed to occur at different times with respect the wave profile: at the wave trough for the sealed cylinder and again at mean water level for the diffuser cap. This suggests that the large openings of the diffuser allow an internal flow that determines a different timing of the loads.
One last topic addressed by Mogridge and Jamieson (1978) is the effect of a discharge. An increase of the vertical force was observed for the case in which a discharge (see figure 2.5) was passing through the openings.

The master thesis by Hecimovich (2013) and the subsequent paper by Cornett et al. (2015) describe the experimental study on an intake-cap structure under the action of regular and irregular waves. The cap studied was made of four support cylindrical columns, a top cap and a central pipe. The set-up used allowed to isolate the parts of the intake structure and define force coefficients for each of these. The result of that study showed

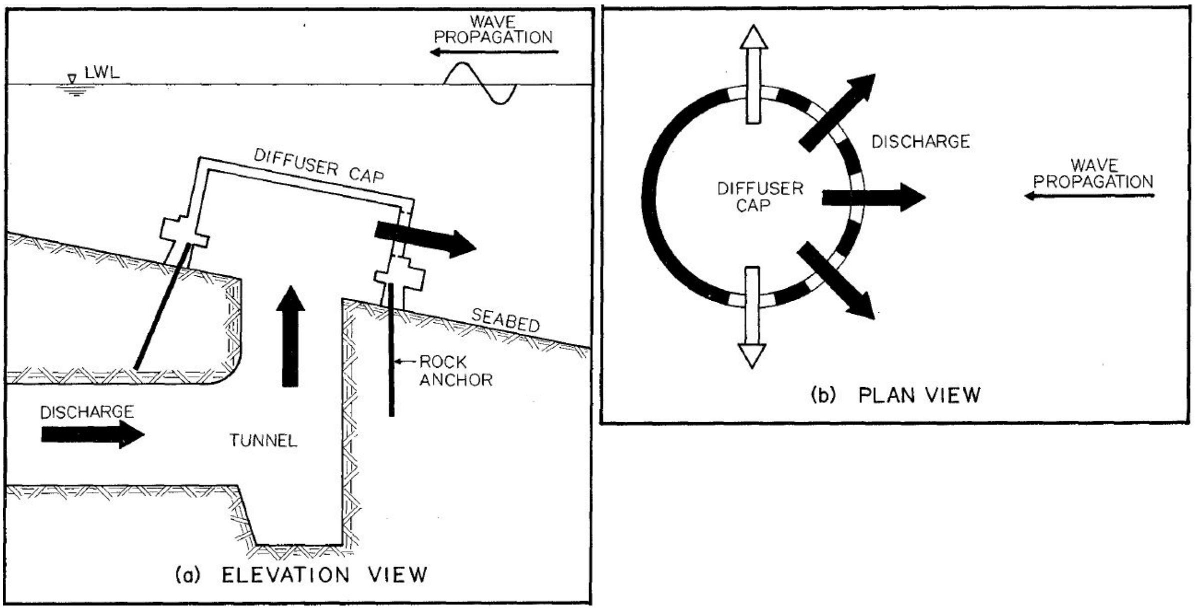

Figure 2.5: Side cross view and plan view of the diffuser structure used by Mogridge and Jamieson (1978) for the physical model tests.

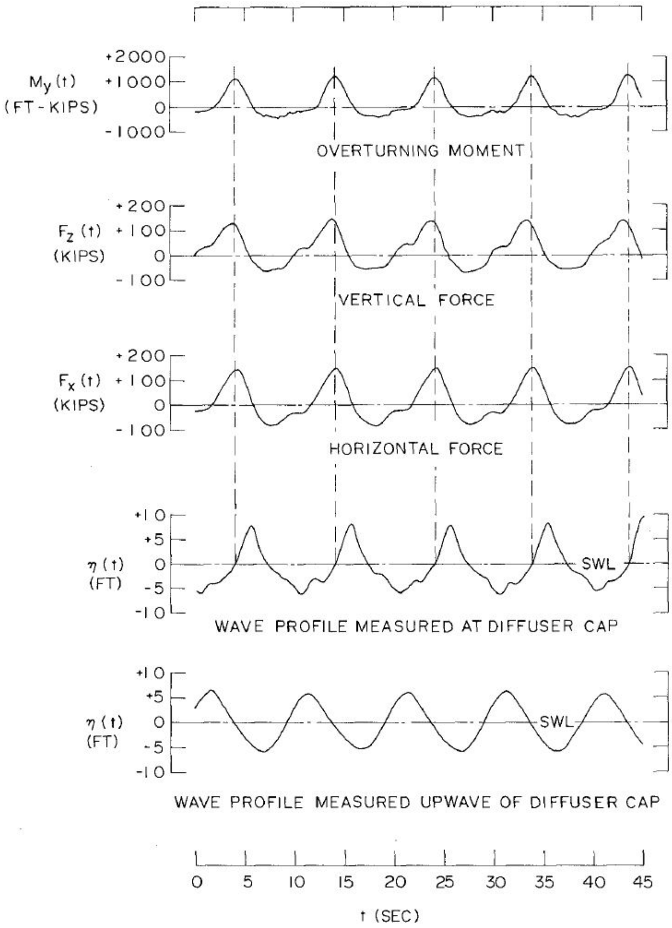

Figure 2.6: Typical results of the experiements by Mogridge and Jamieson (1978) on a open diffuser-cap type outfall.

that the Morrison equation can predict the general character and the timing of the loads. The hydrodynamic coefficients found were in agreement with the research by Sarpkaya (1979) proving the analogy between the bundle of cylinder and the open intake structure. With regards to the magnitude of the loads, however, this approach could only predict the forces caused by smaller amplitude waves. The poor prediction suggested that the method was not reliable in case of high amplitude nonlinear shallow water waves.

2.3.2. Numerical model investigations

Another important way to look at the forces on offshore structures is computational fluid dynamics (abbrv. CFD). The shape of a cylinder is generally of major importance in literature (see Paulsen (2013) and Paulsen et al. (2014)), where validated model are shown to perform well when computing the loads for irregular waves for vertical and horizontal cylindrical structures. Other examples of CFD investigations can be found for caisson types breakwaters (Bricker et al., 2015) or caisson type emerged intake (S. Kiran Raju et al., 2014).

Less literature is available for the specific geometry of the velocity cap. With this regard, it is important to quote the study by Christensen et al. (2015) where the authors set up an OpenFOAM model to study the flow around the velocity cap and to look in more detail at the decomposition of the force between inertia and drag components. The research focused on very low KC numbers, in the range between 0.30 and 1.5. Besides, the dependency of the force coefficients of geometrical ratios of the cap was also analyzed. In their model, the authors were using a symmetrical one-dimensional oscillation (thus without any vertical component). One of the conclusions stated in their paper was that, unlike what found by Sarpkaya (2010), the inertia coefficient increased with KC number instead of decreasing. The possible explanation suggested by the authors was that the complex geometry of the cap was affected differently by the wave motion when changing the KC number, which determined changes in the forces regimes.
Their findings however can also be explained by the "bundle effect" encountered also in Hecimovich (2013). This effect is explained as the increase in added mass of a bundle of pipes due to the large fluid mass trapped between them. Also in Hecimovich (2013), the dependency of C_M shows a positive trend when plotted against KC.

Numerical simulations aimed to the study of turning moment (or pitching moment) have also been performed. This topic is particular important for hydro- and air-foils given the importance of the pitching moment on moving vessels or air crafts. In civil engineering, the topic is often relevant in the case of bridge design when inundation due to river flood (Kornel Kerenyi and Guo, 2009) or tsunami waves needs to be taken into account (see Bricker and Nakayama (2014) and Xu et al. (2017)). Both in the case of a swollen river and a tsunami simulation the flow conditions studied were showing a slowly varying velocity of the current. In this scenarios the inertia was always playing a limited or no effect on the moment and on the loads in general. With this regard, the present study has the double purpose of assessing the values of the turning moment coefficient for cases where inertia is more important and the geometry is different.

2.4. Relevance of this thesis

The literature review confirmed the need of an extension of the research on the behaviour of the force coefficients for a velocity cap for varying numbers of KC.

The determination of force coefficients was often limited to inline force. In this thesis, the analysis on vertical force and moment coefficients aims to extend the characterization of the loads in order to provide simple numerical values and graphs that can be used during the design.

In order to aid this process, the validation of a numerical (CFD) model which can reproduce the actual motion of free surface waves is also carried out and adds to the present state of the research. By means of this model the analysis could be extended in the future with more scenarios. To already contribute to this extension, the effect of a discharge through the cap on the force coefficients is briefly addressed at the end of the numerical analysis.

3

Experimental data

The experiments analyzed in this thesis project were carried out in summer 2017 in the water laboratory of Deltares located in Delft. The aim of the study was to collect more information regarding the loads on the type of velocity cap described in the introduction, focusing particularly on the effect of solitary waves. This chapter summarizes the part of the experimental campaign that constitutes the starting point of the present research. The summary includes a description of the main features of the physical model, the different test cases and the several sources of measurement data.

3.1. Geometry and scaling

The geometry of the cap and the scaling rules applied for this set of experiments were already used in previous physical model tests at Deltares (see Capel (2012a) and Capel (2012b)). In this section the main features of the physical model are presented.

3.1.1. The facility

The tests were performed in the Scheldt Flume of the Deltares Hydrohall. This flume has a width of 1 meter and a length of 110 m and it is provided with a piston-type wave-maker at both ends able to generate regular and irregular wave. For the experiments, the flume was divided in two sections of 55 m, of which only one was used. A wooden frame was prepared to create a 1:50 slope in order to induce shoaling and, in some cases, breaking of the waves. Eventually, given the position of the velocity cap, the useful length for the propagation of the waves was approximately 20 m. The velocity cap was positioned on a horizontal segment of this frame, 0.3 meters long, preceded and followed by the 1:50 slope. No particular measures were taken to prevent wave reflection.

Table 3.1: Measures and features of the flume set-up used in the experiments.

Wave maker	Piston type
Total length of the flume	55 m
Dist. between wave maker and cap	20 m
Dist. between wave maker and start of the slope	2.35 m
length of the slope before the cap	17.5 m
Slope	1:50
Height of the frame at the level of the cap (from the bottom of the flume)	0.35 m

3.1.2. Scaling

The full scale prototype of the velocity cap has a height of approximately 8 meters and the widest part has a diameter of approximately 10 meters. In the present set of physical model tests, the scale factor chosen was 1:46.25.
For free surface wave modeling, inertial and gravitational forces play generally a dominant role (Hughes, 1993). For this reason, Froude scaling, which preserves the ratio between these two forces, was applied (Capel, 2012a). The Froude number (Fr) can be written as follows.

$$Fr^2 = \frac{u^2}{gL} \tag{3.1}$$

The symbols u and L indicate a velocity [m/s] and a length [m] respectively. Table 3.2 gives an overview of the scaling factors used to prepare the model set-up. By using them, it is possible to translate the outputs of the experiments into full scale values. The table also includes conversion factor for forces and velocities. In particular the force scaling factor is corrected with the constant 1.025 in order to account for the different density of the water between prototype and model conditions.

Table 3.2: Scale multiplier to transform the model-scale dimensions into the full scale dimensions.

Model Scale	Length	Time	Velocity	Acceleration	Mass	Force
1:46.25	46.25	$\sqrt{46.25}$ $= 6.8$	$\sqrt{46.25}$ $= 6.8$	1	46.25^3 $= 98931$	$46.25^3 \cdot 1.025$ $= 101413$

The results of the physical model observations, described in the first part of this thesis, are reported in SI model-scale values. The velocity cap used in the experiments measures 0.168 m in height and 0.22 m in diameter (see figure 1.2). Besides, differently from the prototype, the vertical support cylinder of the model is full. More specifications regarding the geometry of the cap as well as the drawings of the scaled model are included in appendix A.

In case of scale models, it is impossible to preserve all the force ratios that can be defined (Heller, 2011). In the experiments described here, scale effects could be due to the fact that force ratios, such as Reynolds number and the Weber number (commonly considered in physical model tests), are not thoroughly preserved. However, in both cases, it can be shown that the scale effects are negligible for the present application. A quick calculation shows that, following the scaling described in table 3.2 and the formulation of the Reynolds number of eq. 2.1, it can be expected that in real-world Re is on the order of $10^7 - 10^8$, while in laboratory it assumed numbers in the order of 10^5 (see section 6.1.3). With these Reynolds numbers, turbulence is already fully developed and the physical features of the viscous forces acting at $Re = 10^5$ are similar to the ones acting at $Re = 10^7 - 10^8$. Therefore, the Re of the laboratory experiment is considered big enough to neglect Reynolds scaling effects.

The Weber number instead describes the ratio between the inertial force and surface tension of the water. Given the intrinsic difficulty of scaling a molecular property of water such as the surface tension, Weber scaling is hardly used. Hughes (1993) suggested simple rules of thumb for preparing free surface wave experiments in which the effect of the surface tension on the wave length is less that 1%. According to these rules the water depth needs to be bigger than 0.02 meters and the period of the waves needs to be bigger than 0.35 seconds. For the cases analyzed here these requirements are met with a large margin (see tables 3.3 and B.1).

The scale effects related to the Weber number might also be considerable in case of wave breaking where air entrainment plays a role in modelling the free surface (Heller, 2011). Some of the tests performed involved wave breaking but the possible influence of the surface tension at the surface is of minor importance. In this thesis, in fact, the focus is on the loads on a submerged structure and these are really little influenced by the air entrainment at the surface.

3.1.3. Water depths

The value of water depth used in the experiments is based on the general conditions in which these caps are found in operation. Three water depths are analyzed and the choice of these is based on the geometry of the cap. Figure 3.1 shows the relation between the height of the opening of the cap and the several water depths. The values shown in the figure correspond in prototype scale to water depths ranging between 10 and 15 meters which represent approximately the conditions in which these structures are installed.

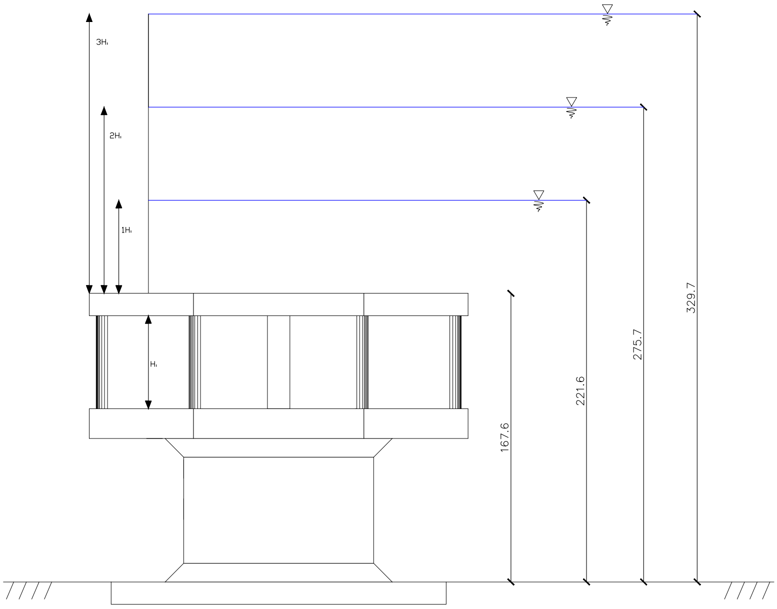

Figure 3.1: Technical drawing reporting the relation between the three water levels tested and the geometry of the cap. For more specification about the geometry of the cap see appendix A.

3.2. Test cases

The tests performed included solitary waves, irregular waves and N-waves. The specific type of wave was generated by the wave-maker by means of steering files prepared to achieve specific target values for wave height (or significant wave height), wave shape and spectrum.
The analysis in this thesis focuses on the solitary wave test cases which were the main focus of the experimental campaign as well. An attempt was also made to extend the analysis to the irregular wave tests but technical complication while setting up the numerical model for these cases suggested to focus the attention on the solitary waves only. More details on the analysis of the irregular waves experimental evidences as well as why these cases were not considered further in the analysis can be found in appendix B.

In this section a brief presentation of the solitary wave test cases is given.

3.2.1. Solitary wave tests

In the case of the solitary waves the combination of three different water depths and three values of the ratio H_0/h_0 (wave height over water depth) originated 9 different tests conditions. The steering files relative to these conditions were generated by means of a MATLAB script developed by Dr. ir. Bas Hofland. The wave period was always set to 10.0 seconds while the dimension of the wave was controlled by the parameter H_0/h_0, which was equal to 0.4, 0.6 and 0.78.
These values were used to generate the steering files used during the experiments, however they have little relevance to the observed conditions. In practice, that value expresses the characteristics of a wave as soon as it travels out of the wave paddle but, as said, the propagation of the wave was immediately affected by the presence of the slope. That is the reason why in this thesis, it is preferred to use the observed ratio between the wave height and the water depth measured by the wave gauge at the velocity cap itself as a reference parameter. H/h is therefore the height of the solitary wave above the cap normalized by the water depth at the cap. Each of these tests was repeated 5 times, except for one condition ('T201') that was tested 40 times to obtain a good estimate of the ensemble averaged flow properties.
The set-up of the several experiments is summarized in table 3.3.

Table 3.3: Description of the 9 test cases involving solitary waves.

Test name (Solitons)	Water depth (h) [m]	H_0/h_0	H/h	Breaking	Test repetitions	Period [s]
T101	0.22	0.4	0.92	no	5	10.0
T102	0.22	0.6	0.97	yes	5	10.0
T103	0.22	0.78	0.82	yes	5	10.0
T201	0.28	0.4	0.68	no	40	10.0
T202	0.28	0.6	1.12	no	5	10.0
T203	0.28	0.78	0.95	yes	5	10.0
T301	0.33	0.4	0.56	no	5	10.0
T302	0.33	0.6	0.95	no	5	10.0
T303	0.33	0.78	1.07	no	5	10.0

The specific combinations of wave height, water depth and slope were aimed in some cases to generate a breaking wave and in the table above a test is characterized by a 'yes' under the field 'breaking' if breaking of the solitary wave was observed at the cap or before reaching the cap.

3.3. Measurements

The measurements taken are of three types. The first two are generally referred to as "Delft measure system". This method consists of using wave gauges to measure the surface elevation at a given locations and force sensors on the object of interest. The sampling rate of these two types of measurements was 60 Hz. The third type of was taken only for the test relative to the solitary waves and consists of Particle Image Velocimetry (PIV) measurements. Considered the general magnitude of the velocity expected during the tests and the big dimension of the PIV files, a sampling rate of 30 Hz was preferred.

3.3.1. Surface elevation measurements

The measurements of the water surface were taken by means of seven wave gauges. The information relative to the position of the first wave gauge (the closest to the wave paddle) was proven wrong by the simulation run with the numerical model OceanWave3D (see section 4.1). The clear mismatch between the prediction by the numerical model and the experimental record showed that the position of that sensor was not the one indicated in the tests log. Adjusting the value to get a better match led to the conclusion that the wave gauge was at 14.45 m from the velocity cap and not at 17.5 m as originally prescribed while setting up the facility. The uncertainty about the position of the sensor however suggested not to use the data from that wave gauge for the force reconstruction described in chapter 6.

Figure 3.2 reports the geometrical details of the set-up, including the positions of the wave gauges. The prescribed position of the first wave gauge (in red) and the estimated new position are also shown. In the picture, as well as in the rest of the document, the several wave gauges are indicated with the abbreviation WHM ('Wave Height Meters').

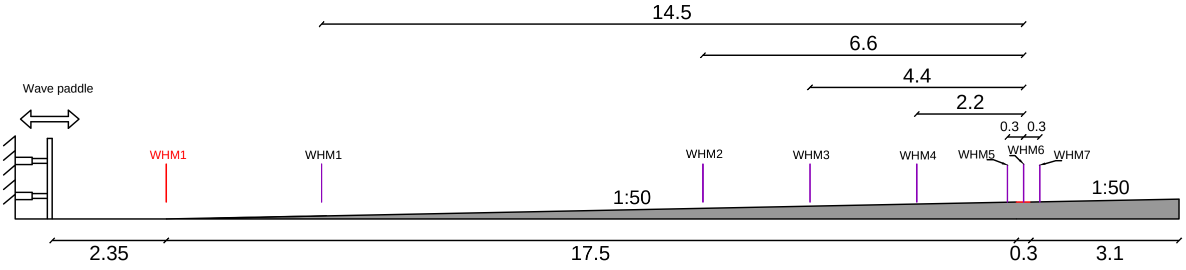

Figure 3.2: To scale sketch of the test set-up. The position of the first wave gauge reported in the experiment log is shown in red. The purple lines show the actual positions of the wave gauges (called WHM) that were used to record the water elevation. The small red segment shows the horizontal section of the bed where the cap was positioned. The indication of the distances of the wave gauges are all referred to the center of this red segment corresponding to the center line of the velocity cap.

With regards to the distance from the center line of the flume, there is a difference between the three wave gauges placed in proximity of the cap and the other four. The three closer to the cap were located at a distance of 10 cm from the side wall of the flume, while the others were placed in the middle of the flume.
These sensors are developed by Deltares and consist of two parallel stainless steel rods mounted underneath a small box containing the electronic component. The wave gauges operate measuring the resistance of the water between the rods and determine the level of the surface elevation based on the principle that the resistance is proportional to the immersion depth of the rods (Deltares, 2016). The calibration records show that the accuracy obtained was on the order of 0.002 m. Figure 3.3 shows the typical plot of the surface elevation recorded by the 7 wave gauges.

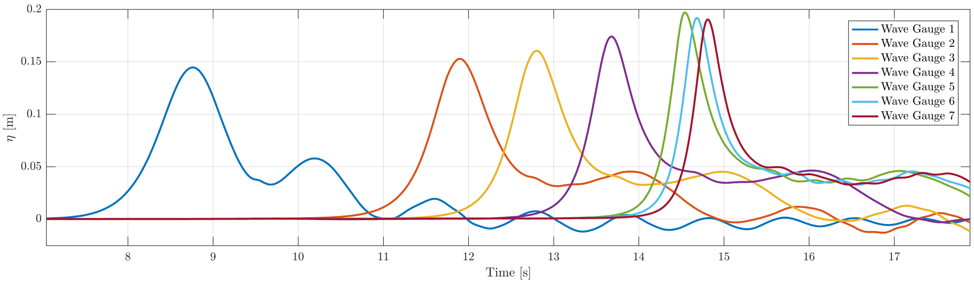

Figure 3.3: Measurements of the surface elevation of test T201.

3.3.2. Force measurements

The force sensors were mounted at the base of the velocity cap as illustrated in figure 3.4 and could measure the linear forces acting on the cap in all directions.

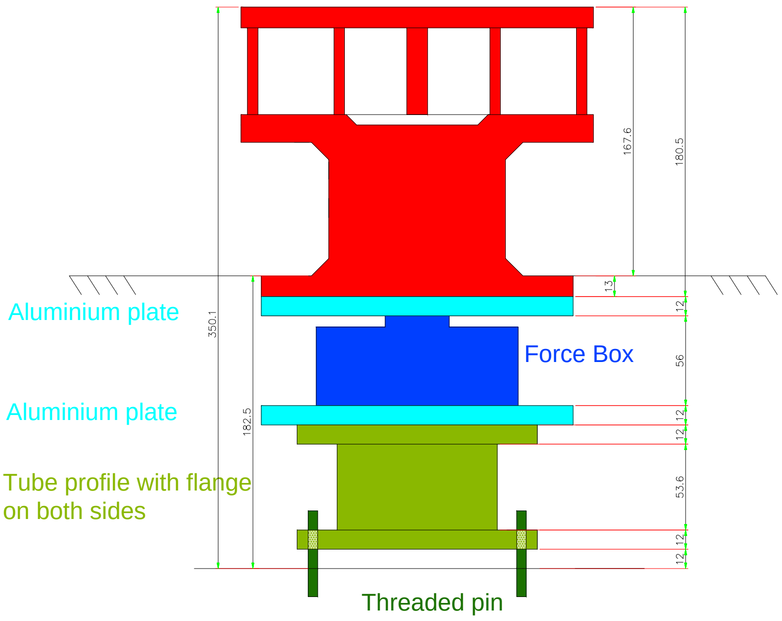

Figure 3.4: Sketch of the setup of the force sensors. The dimensions are expressed in mm.

The sketch shows that the base of the cap was mounted on an aluminum plate then screwed to the force sensor box. In order to let the object free to move, therefore the block formed by the aluminum plate plus the velocity cap was surrounded by water. This caused a mismatch between the results obtained with the CFD model and the experimental records because the numerical model does not take into account penetration of water under the bottom. More detail with this regard are included in chapter 5.

The experiment logs report that, for the set of repetitions of the first 3 tests (namely T101, T102, T103), the force sensors were not correctly calibrated giving records for the forces approximately a factor 2 too high. When the problem was noticed, the tests were not repeated and the force records were replaced with the one obtained with the single repetition of the calibration test[1]. For these tests, the records of the surface elevation instead were correct and were maintained in the final database.
The reason for these incorrect measurements was related to the presence of small plastic floaters found trapped close to the base of the velocity cap which probably caused the cap to be clamped to the floor. With the cap unable to move freely the force transducer did not measure the actual hydrodynamic force acting on it. Draining the flume, cleaning the water and removing the plastic floaters close to the base of the cap prevented this problem from happening again.

Figure 3.5 shows the typical phasing between loads and surface elevation observed in the tests involving solitary waves. It can be noted that the vertical force is directed downwards. From a design point of view therefore the absence of a lift force that could make the structure more unstable works in favour of safety.

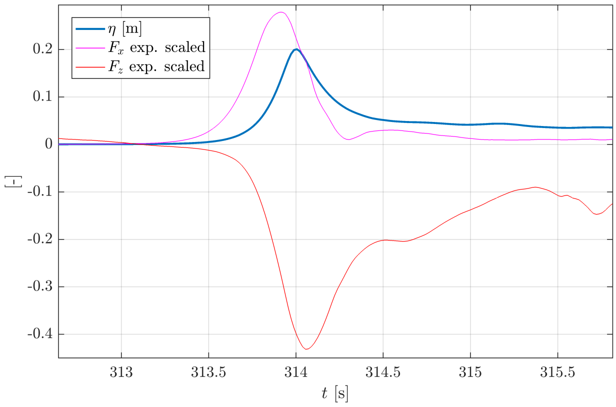

Figure 3.5: Example of the phasing between loads and surface elevation in the case of test T101. The scale factor is 50 for the inline force and 70 for the vertical one.

Figures 3.6 and 3.7 show the plots of the peaks of the inline and lift force for the different test cases over the ratio H/h of table 3.3 (only the ensemble average for every test case is plotted).

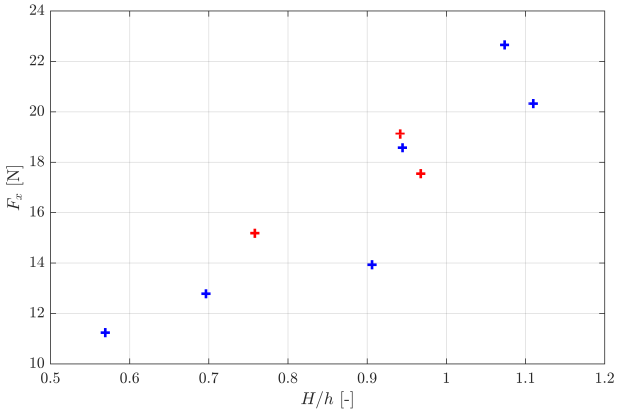

Figure 3.6: Peaks of the inline force per every test case (ensemble average) plotted over the measured H/h. In red the symbols relative to the tests that involved breaking.

---

[1] Every test was simulated in advance with one test repetition (called calibration) with instrumentation running and same parameters to check if the set-up was working properly.

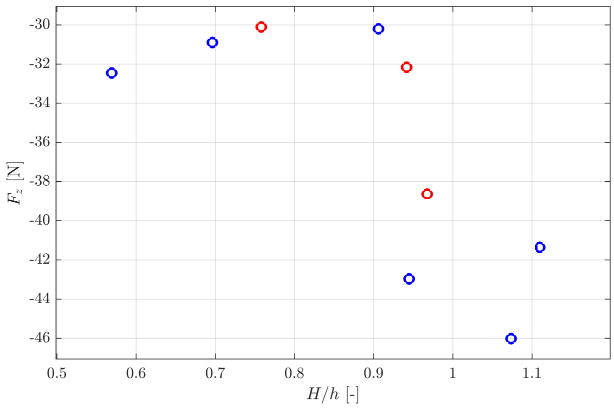

Figure 3.7: Peaks of the vertical force per every test case (ensemble average) plotted over the measured H/h. In red the symbols relative to the tests that involved breaking.

3.3.3. PIV measurements

In addition to the Delft measures, PIV measurements were also taken in the case of the tests involving solitary waves. The sampling rate of the PIV measurements was different from the one of the Delft measures, but during the experiments the two measuring systems were linked in order to obtain a synchronization of the time axes.

The particle image velocimetry technique consists of lighting up the particles present in the water (bubbles or impurities) on a thin plane and then taking pictures at small time intervals of these particles in order to capture their movements in the domain of the camera.

The PIV window (i. e. the domain of the camera) for all the experiments was wide enough to include the free surface (see schematic of figure 3.8). However the processed results were obtained for a smaller window 63 cm wide (the width corresponding to the x-axis of the flume) and variable in height. The height of the window depends on the water depth. In fact, the free surface and the areas with an excessive number of bubbles needed to be cut out. In particular, wave breaking in test T103 caused large areas of the frames captured to be in shadow and therefore no information could be obtained. For this reason no post-processing has been attempted for the PIV measurements of T103.

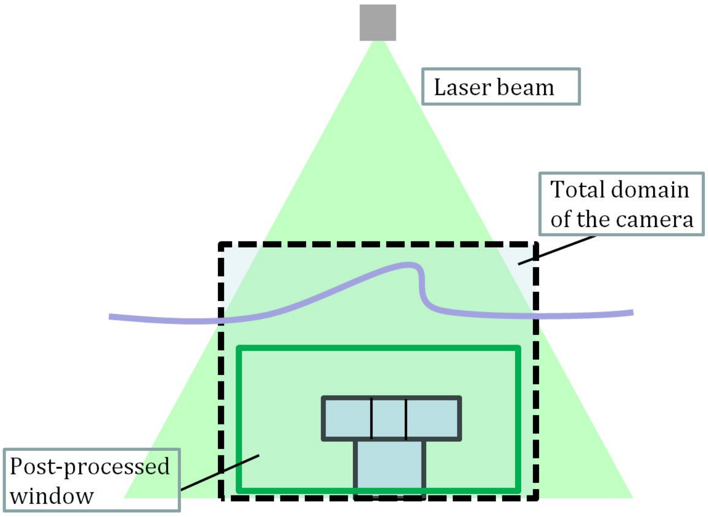

Figure 3.8: Sketch of the PIV set-up. The laser sheet used to light up the particles was parallel to the direction of propagation of the flow. The scaled model of the velocity cap was realized with a strip of transparent material at the center-line (see figure 1.2) so that the laser beam could pass through and light up the particles right next to the lower support cylinder.

PIV POST-PROCESSING

The raw data generated by the camera were post-processed by means of the commercial software DaVis 8 developed by LaVision. The software allows to select the parameters for the velocity vector calculation and the filters to remove incorrect vectors.

While processing the data, the total window is divided in smaller interrogation areas, from each of which a velocity vector is then computed. In order to obtain a good quality velocity field reconstruction, each of these interrogation areas needs to contain a sufficient amount of particles. It is also possible to get a better correlation between areas and an overall finer reconstruction by defining a percentage of overlap between areas. However, this procedure, better described in picture 3.9, also introduces oversampling and in common practice the percentage of overlapping areas should never be greater than 75 %.
In the present study the combination of interrogation area size and overlap originated post-processed results with a resolution between 2.5 and 5 mm.

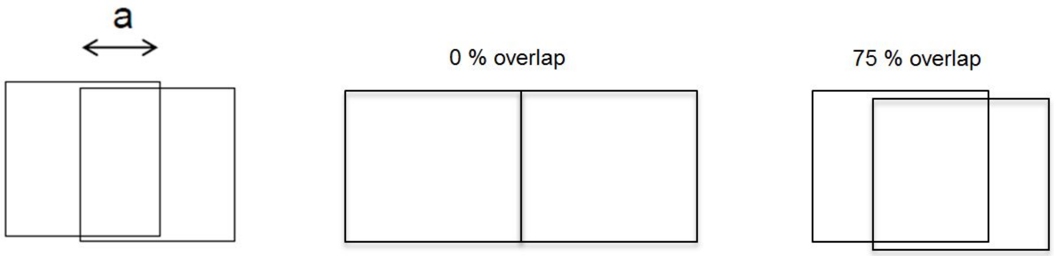

Figure 3.9: Overlapping parts of interrogation areas. The parameter a is the percentage of overlap.

ANALYSIS OF THE VELOCITY FIELD

The flow features are analyzed focusing on ensemble averaged properties. The analysis of the PIV data is based on the results from test case T201 which was repeated 40 times and whose estimate of the ensemble average is therefore the most reliable.

In order to study the convergence of the ensemble average around the velocity cap, the estimate based on 40 test repetitions was compared with the ones obtained considering only 5, 10 and 20 repetitions. The comparison was based on the velocity profile extracted from six vertical transects of the PIV window selected with a spacing of 0.05 m along the x-axis. In this way the vertical profiles of the horizontal velocity according to the several estimate of the ensemble average could be observed. Figure 3.10 shows that nearly everywhere in the PIV domain no appreciable difference could be observed between the estimates obtained with 20 repetition and with 40. This means that already with 20 tests the ensemble average is converging. This is not completely exact in the region of the jet coming out of the velocity cap (see panel in the lower right corner of figure 3.10) where probably more test repetitions would have given slightly different results. Even in this location however the differences are really small ($\mathcal{O}$(cm/s)).

For the same locations shown in figure 3.10, also the standard deviation of the ensemble averaged results is plotted over the vertical. In this way the graphs of figure 3.11 show how much variation in the horizontal velocity is observed between the 40 test repetitions for several locations in space.
The standard deviation of the horizontal velocity is small throughout the entire water column for the only considered location in front of the velocity cap. For the other locations, where the cap is inducing turbulence development, the variation between tests increases considerably. In proximity of the top of the velocity cap and at the location of the jet after it, the standard deviation reaches a value of 0.35 m/s. Knowing from figure 3.10 that the maximum velocity in those locations is approximately 1 m/s, this means that the value of the standard deviation reaches in those locations approximately one third of the total velocity.

An estimate of the undisturbed flow field can be derived from the observation of the left-hand part of the PIV domain. Figure 3.12 shows the ensemble-averaged results for an instant in which the wave was entering the domain of the PIV camera. Colours towards yellow are used for higher velocities and blue for still water. The data points at the far left of the graphs are selected to show the dependency of the horizontal velocity over the vertical. A difference of approximately 10 % can be observed between the top and the bottom of the section

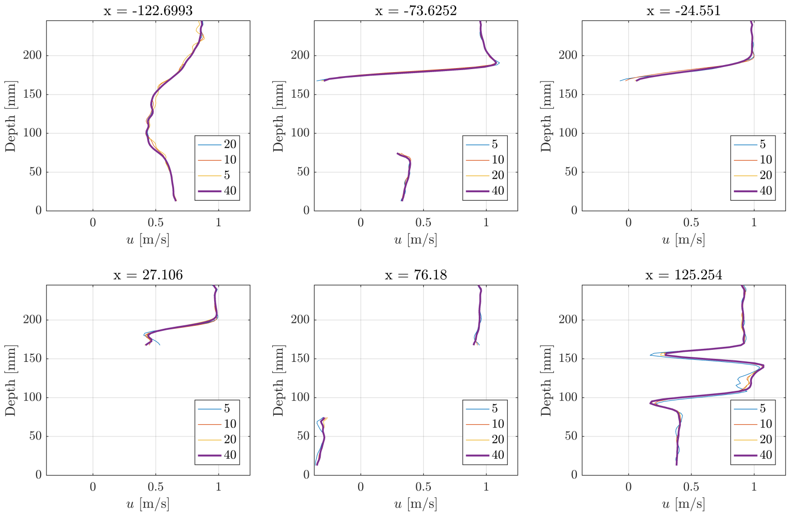

Figure 3.10: Ensemble-averaged vertical velocity profile for six representative locations in proximity of the velocity cap. The orange line of the estimate obtained with 20 repetitions is often covered by the one the relative to the estimate obtained with 40 repetitions.

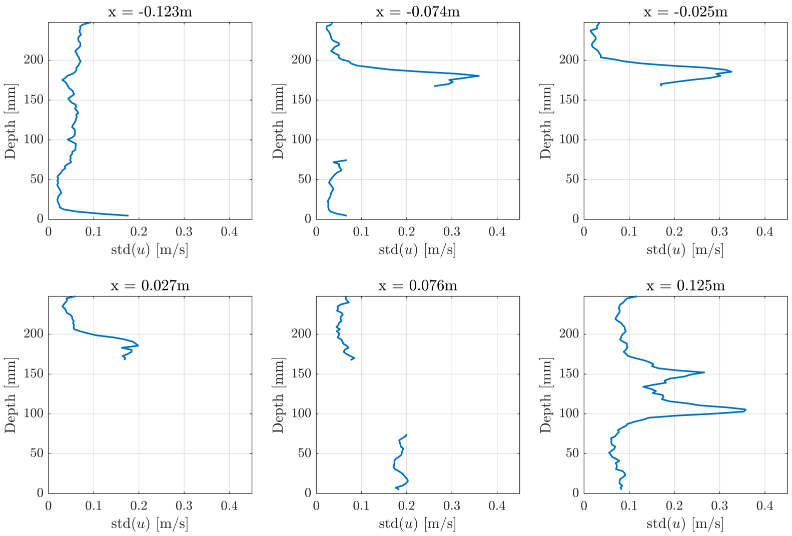

Figure 3.11: Standard deviation of the horizontal velocity plotted over the vertical for the six locations shown in figure 3.10. The white spaces correspond to the locations where no velocity was measured due to the presence of the cap.

of the water column captured in the measurements. This shows that that the wave is behaving as a shallow water wave but the velocity is not completely constant over the vertical.

The velocity field corresponding to the instant of the occurring force peaks, shows specific flow patterns related to the geometry of the velocity cap. Due to the sharp edges of the object, flow separation and recirculation zones are observed on the top surface of the velocity cap and behind it, as soon as the wave approaches the cap. In particular, the recirculation zone at the top leading edge of the velocity cap originates as a small eddy of few centimeters of diameter and grows in time, extending over approximately one half of the top of the cap at the instant that corresponds to the peak of the inline force. Inside the cap, the openings of the structure allow the flow to go through it, as can be seen from the high velocity measured behind the object (see figure 3.13).

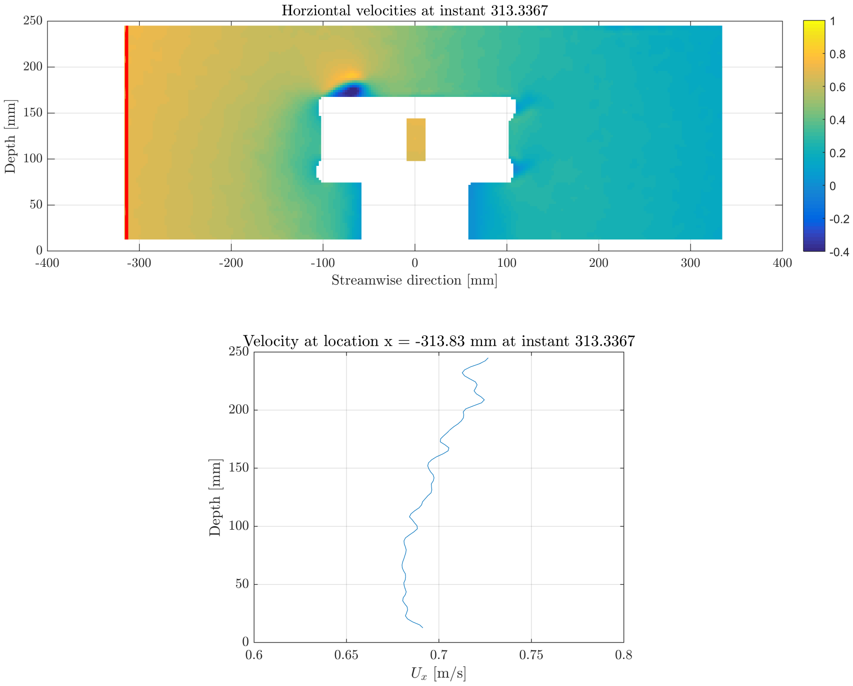

Figure 3.12: Upper panel: plot of the horizontal velocity component at a given moment in time for test T201. The color of every point in the graph corresponds to a value of the velocity (the horizontal component only).
Lower panel: plot of the horizontal velocity over the water column for the position highlighted in red in the upper panel (on the far left).

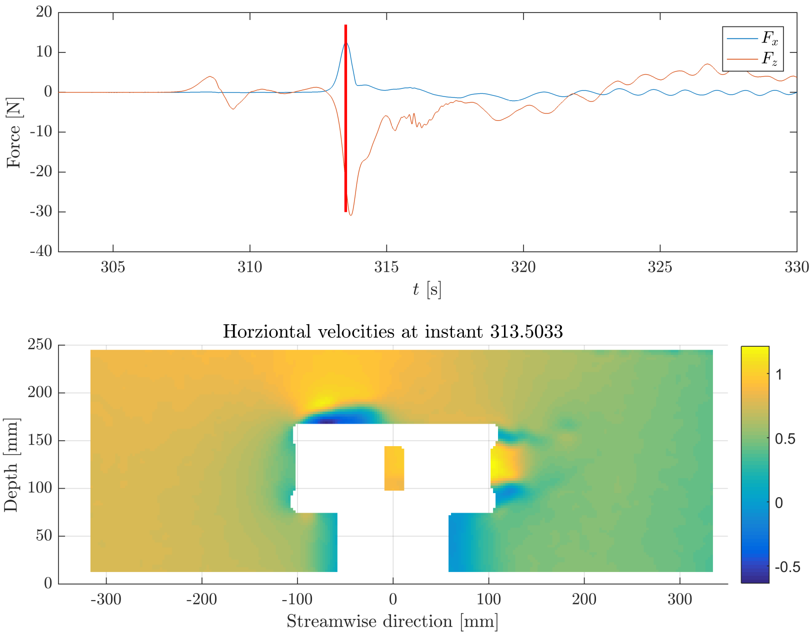

Figure 3.13: Example of a PIV velocity reconstruction and synchronization with the forces time series for test case T201. The top panel shows the force signals and red vertical line indicates from which instant the velocity field of the lower panel is taken from. Also here the colours in the lower panel correspond to the magnitude of the horizontal velocity.

4

Numerical models

In the present chapter, the two numerical models used in the numerical analysis are described. These are the potential flow solver OceanWave3D (abbr. OCW3D) and the Computational Fluid Dynamics (CFD) library OpenFOAM.
The solution of OCW3D is used as a boundary condition to the CFD simulation carried out by means of the open-source library for CFD OpenFOAM, used with the wave generation toolbox wave2Foam. The potential flow solver OCW3D, in fact, is not appropriate to solve the flow just around the velocity cap and compute the loads on it. Therefore, the CDF model is used to study the forces on the velocity cap in more detail.

4.1. OceanWave3D

The OceanWave3D model is presented in Engsig-Karup et al. (2009) and is described as a fully-nonlinear 3D potential flow solver based on finite difference discretion method. It makes use of a robust flexible order scheme that offers fast and accurate computations for offshore applications.

4.1.1. General description

The assumption of potential flow has the limitations of neglecting viscous terms that, in coastal application, may become important close to solid boundaries and in case of wave breaking. However, dealing with a potential flow solver allows the use of numerical higher order schemes (and therefore smaller error) both in space and in time. In oceanic waters, when the flow is not turbulent (i. e. far away from solid boundaries or structures and when severe wave breaking does not occur), therefore, the viscous terms are negligible and the utilization of a numerical model such as OCW3D can be preferred for the sake of accuracy and computational time. The authors themselves specify that when the assumption of potential flow is not true, a more refined viscous flow solver should be used.

In the situation of the physical model tests described in chapter 3, the main phenomena that can be captured by OCW3D are the propagation and the shoaling with the consequent change in shape of the waves. In this perspective, OCW3D solves the propagation of waves in one direction and it is used in this thesis for two purposes. In first place, in chapter 5 the OCW3D solution is used to force the computation of OpenFOAM® in the relaxation zone at the inlet (see section 4.2.3), secondly in chapter 6 and 7, the estimate of the flow dimensionless number (KC and β) is based on the reconstruction of the undisturbed velocity field computed by this model.

The loads on the velocity cap could not be studied directly with OCW3D for two reasons. First of all the geometry of the velocity cap (i. e. the presence of sharp edges) causes the flow to separate and become turbulent even in the case of small Reynolds numbers. Besides that, the finite difference discretization method is not capable to handle geometrical complexities such as multiple interfaces between bottom and numerical domain on one single vertical line (see figure 4.1).

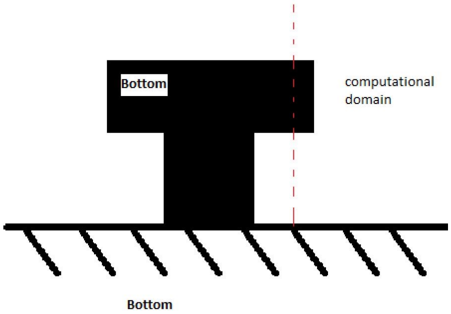

Figure 4.1: The geometry of the velocity cap would pose problems with regards to the spatial discretization to simpler flow solvers. In this extremely simplified sketch of the velocity cap, multiple interfaces between bottom (outside of the domain) and numerical domain can be noted along the red dashed line.

4.1.2. Governing equations

The potential flow problem is solved based on an Eulerian approach where the free surface elevation (η) is a single-valued function of the horizontal coordinates x and y. In the present thesis the full 3D capabilities of the model were not used because the focus was on the 2D propagation of a wave. However, the description that follows includes the terms in the y as described in the original paper by Engsig-Karup et al. (2009).
The fluid is assumed inviscid and irrotational and the velocity field (u, v, w) is defined by the gradient of a scalar velocity potential $\phi(x, y, z, t)$. Kinematic and dynamic boundary conditions (eq. 4.1 and 4.2) determine the evolution of the free surface.

$$\frac{\partial \eta}{\partial t} = -\nabla_H \eta \cdot \nabla_H \tilde{\phi} + \tilde{w}(1 + \nabla_H \eta \cdot \nabla_H \eta) \tag{4.1}$$

$$\frac{\partial \tilde{\phi}}{\partial t} = -g\eta - \frac{1}{2}(\nabla_H \tilde{\phi} \cdot \nabla_H \tilde{\phi} - \tilde{w}^2(1 + \nabla_H \eta \cdot \nabla_H \eta)) \tag{4.2}$$

In these two equations, the operator ∇_H only indicates the gradients on the horizontal plane ($\partial/\partial x$ and $\partial/\partial z$). The potential and the vertical velocity are expressed in terms of the surface elevation so that $\tilde{\phi} = \phi(x, y, \eta, t)$ and $\tilde{w} = \partial\phi/\partial z\Big|_{z=\eta}$.

Solving the Laplace equation for the water column (eq. 4.3) and the kinematic boundary condition at the bottom (eq. 4.4) allows to find the value of $\tilde{w}$ and to proceed in time. The Laplace equation is solved by a flexible-order finite difference scheme.

$$\nabla_H^2 \phi + \frac{\partial^2 \phi}{\partial z^2} = 0, \quad -h \leq z < \eta \tag{4.3}$$

$$\frac{\partial \phi}{\partial z} + \nabla_H h \cdot \nabla_H \phi = 0, \quad z = -h \tag{4.4}$$

In the actual implementation of the problem, the vertical coordinate is modified in order to map the solution to a time-invariant domain. The moving surface elevation in fact would make the vertical grid time dependent which is not convenient for the computations. The vertical coordinate is therefore modified by means of the σ-coordinate transformation expressed as:

$$\sigma = \frac{z + h(x, y)}{\eta(x, y, t) + h(x, y, t)} \tag{4.5}$$

The solution to the Laplace problem is therefore found in a time-invariant (x,σ)-domain. Once the potential is known the velocity field can be derived.

4.1.3. Domain

The length of the flume simulated in OCW3D is approximately 50 meters but its length in the numerical domain is computed automatically by the model depending on the steering file specifications. At the beginning of it, a numerical wave paddle is modelled by means of Dirichlet boundary conditions to impose the velocity profile over the vertical. At the end, a pressure zone guarantees the absorption of the waves and avoids reflection. In the present application, the length of the pressure zone at the end of the domain corresponds to one wave length of a wave whose period is the peak period specified by the steering files. The peak period for solitary waves was always set to 10.0 seconds and the calculation of the corresponding wave length based on the dispersion relation gives the values of the pressure zone. All simulations are two-dimensional and therefore the width is equal to one single cell.

Depth	Length of the domain	Wave length
0.22	48.3	14.7
0.28	52.3	16.4
0.33	55.7	17.9

Table 4.1: Specifications of the OCW3D domain. The information are dependent of the water depth considered. Length of the pressure zone at the outlet of the OCW3D domain for the three water depth considered. The computation follow from the dispersion relation and the period is always 10 seconds as contained in the steering files.

4.1.4. Convergence study

In order to assess the quality of the estimation of the numerical method, the solution is compared with the experimental records from the physical wave gauges. Figure 4.2 and 4.4 show an example of this comparison. The several lines that are observed are the signals of the 7 wave gauges plotted together. All the figures shown in this chapter are relative to solitary wave tests in which only one wave was generated.
When reproducing the conditions obtained during a physical model test, OCW3D can be preferred to many other flow solvers for the possibility of using exactly the same steering files used for the wave paddle during the physical model tests. Importing the steering files leaves to the user only to select the appropriate POT [1] and breaking parameter [2].

Several values of these two parameters have been used in the preliminary simulations. The observation of the results that match the best with the experimental records has led to the selection of the values reported in table 4.2.

Table 4.2: POT values and breaking parameter for the 9 soliton test cases.

Test case	POT	breaking parameter
T101	0.65	0.42
T102	0.65	0.40
T103	0.64	0.42
T201	0.65	0.42
T202	0.65	0.50
T203	0.62	0.42
T301	0.65	0.42
T302	0.65	0.42
T303	0.63	0.65

In OCW3D the refinement of the grid is determined by the number of points per cut-off. This number tells how many grid points are defined per cut-off frequency wavelength, which is the smallest wavelength solved by the model. The cut-off frequency is computed in OCW3D multiplying the peak period of the simulated wave or spectrum times a constant. Modifying the spatial accuracy changes the shape of the computed waves

---

[1] The value of the POT represents a tuning coefficient to determine how much power to give to the wave generator. The default value is 0.8 but after observing a mismatch with the surface elevation recorded during the experiments that value has been changed.

[2] The breaking parameter of OCW3D is defined as $br = -\frac{1}{g} \cdot \frac{\partial w}{\partial t}$, where w is the vertical velocity and generally it holds that $0.4 < br < 1.0$ (Paulsen et al., 2014)

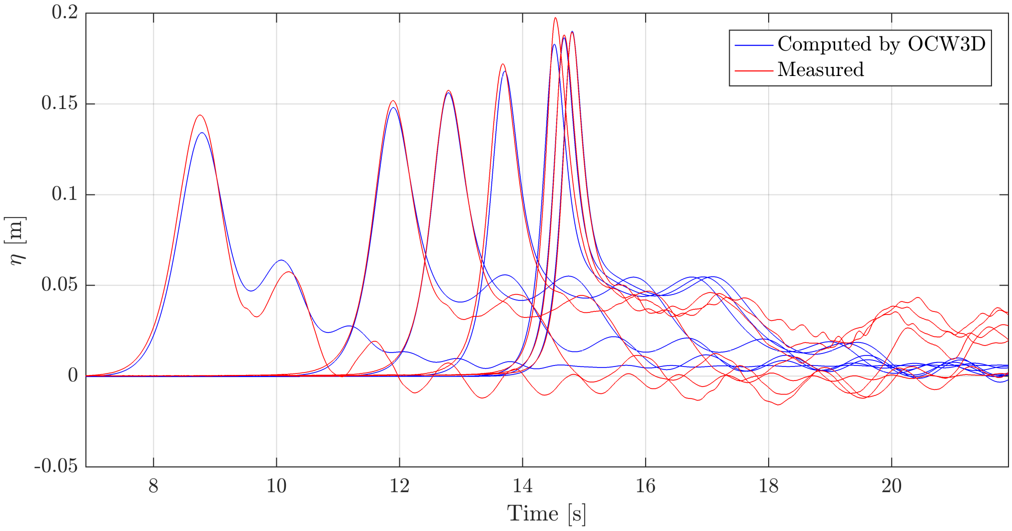

Figure 4.2: Match between experimental measures and computed surface elevation relative to test T201. The plot includes the lines relative to every wave gauge and the line showing the sixth peak in time represents the data relative to the wave gauge at the velocity cap (used later for the force reconstruction).

such that a higher value of grid points is selected to obtain a better convergence. Note that the convergence study described in this section is relative to the test case T201, used as a sample to determine the grid refinement then used for all other the solitary wave test cases. Using several numbers of points per cut-off showed convergence to the final solution obtained for 80 points per cut-off. To show that, the shape error $RMSE_{ppc}$ of the single wave is computed for every run relative to a particular number of points per cut-off (abbr. ppc).

The error is computed as:

$$RMSE_{ppc=x} = \frac{\sqrt{(\eta_{ppc=x} - \eta_{ppc=80})^2}}{\eta_{ppc=80,max}} \tag{4.6}$$

Figure 4.3 shows the graph relative to the convergence study of test T201 used as an example. The value on the vertical axis reports a percentage error: the error between the results of a discretization 80 ppc and 40 ppc is approximately 1.5 % according to the definition of eq. 4.6. Therefore the parameter of 80 points-per-cutoff is used for all the OCW3D runs.

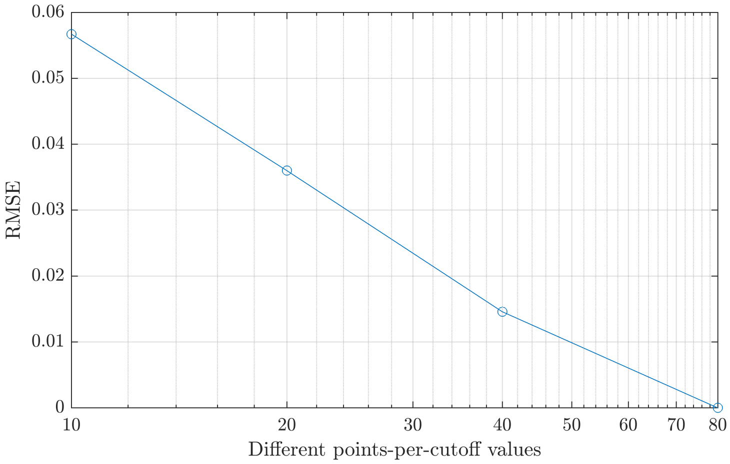

Figure 4.3: Different values of the RMSE for different point per cut-off (test case T201).

Table 4.3 summarizes the number of cells in the x-direction used in the OCW3D computations and the respective errors. It must be noted that the domain of the OCW3D simulation starts at the wave paddle and extends up to a few meters after the velocity cap for a total length of 23.2 meters.

Table 4.3: Overview of the discretization parameter used for the OCW3D computations relative to test T201 and the respective errors.

ppc	10	20	40	80
Δx [cm]	48	24	12	6
Nx	109	217	433	865
$RMSE_{ppc=x}$ [%]	5.67	3.60	1.46	0

In figure 4.2 the match of the surface elevation predicted by the model and the one from the experiments for test T201 is shown. The match was considered good when the shape of the wave up to just after the wave peak and the peak amplitude estimated by the model were showing a good agreement with the experimental record. The remaining part of the signal (i.e. the trailing front of the wave) can hardly be modelled with OCW3D because the structure induced turbulence as well as the wave reflection happening to a certain degree in the physical model could not be included in the numerical simulation.

With regards to the celerity of the solitary wave, a small mismatch is observed between the OCW3D simulations and experimental records. The analysis of the results obtained with the Navier-Stokes/VOF solver shows that a mismatch is still present also for those simulations. In the section treating the OpenFOAM results a quantification of this error is given.

4.1.5. Breaking waves

Oceanwave3D, as said, is a potential flow solver that can solve fully nonlinear wave motions for cases in which the surface elevation does not curl such as in the case of wave breaking. This poses a limit to the use of this model because some solitary wave tests included breaking, since one of the aim of the experimental campaign was to characterize the loads on the cap also in case of breaking solitons.

The already described figure 4.2 and figure 4.4 show two examples of the obtained match of the water surface elevation between experimental measures and results computed by OCW3D. The first one shows a case in which no wave breaking is observed (T201) while the second is relative to a test that originated breaking of the solitary wave (T103).
It can be observed that in the first case the signals from all the 7 wave gauges match reasonably well with the experimental records. The mismatch becomes more considerable in the left hand side of the peaks where turbulence and the interaction with the structure cause a more considerable divergence of the results. This is not affecting much the goodness of the force reconstruction because the biggest attention is on the peaks (of the surface elevation and of the horizontal velocity) and those are fairly well modelled by the numerical simulation.
The second graph shows instead a case in which the model has to take breaking into account. In practice the breaking parameter only sets a limit to the shape of the wave and reduces artificially those that pass that limit. Even using a breaking parameter that predicts breaking at the right location, the match is quite poor and the reconstruction of the velocity is very little reliable. Therefore in the remaining chapters, the tables that contain information derived from the velocity computed by OCW3D show in red the specifications relative to the tests in which breaking is observed.

4.2. OpenFOAM

The CFD model used is the Open Source Field Operation and Manipulation (OpenFOAM®) C++ library[3]. OpenFOAM is described in the user manual as "a framework for developing application executables that use packaged functionality [...]. OpenFOAM is shipped with approximately 250 pre-built applications that fall into two categories: solvers, that are each designed to solve a specific problem in fluid (or continuum) mechanics; and utilities, that are designed to perform tasks that involve data manipulation" (The OpenFOAM Foundation, 2017). In this thesis, the specific solver used was combined with the wave generation toolbox

---

[3] The version of OpenFOAM used in this thesis is v1606+

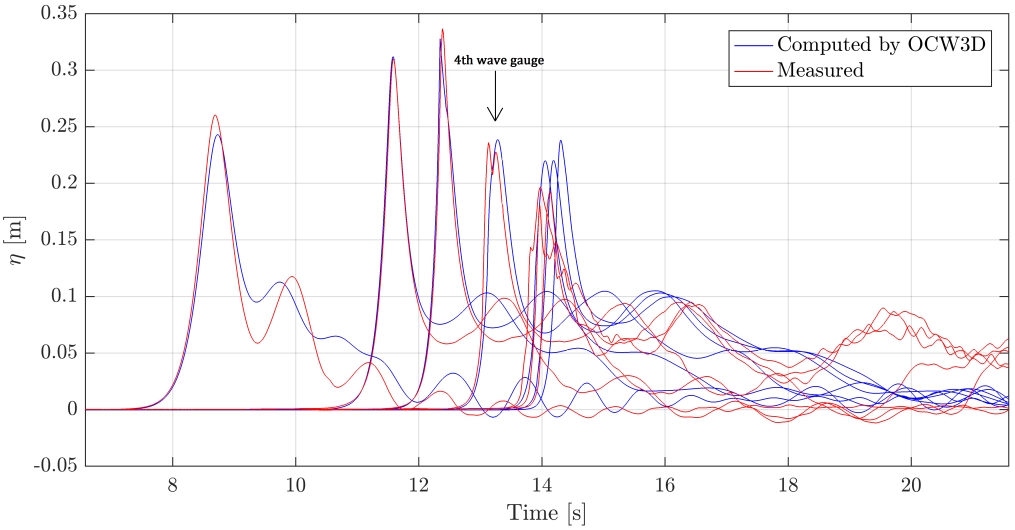

Figure 4.4: Match between experimental measures and computed surface elevation relative to test T103. It can be observed that the wave breaks more or less at WHM4 and that the match at the following wave gauges is quite poor.

waves2Foam developed by Jacobsen et al. (2012). The next sections give a description of the numerical framework of OpenFOAM model and of the wave tank set-up used to analyze the loads on the cap.

4.2.1. Governing equations

The model used in this thesis includes an air and a water phase. The fundamental equations are the Reynolds-averaged Navier-Stokes momentum equations (abbreviated RANS, eq. 4.7) coupled with the continuity equation for incompressible and viscous fluids (eq. 4.8). The solution for the set of equations is sought simultaneously for the two immiscible phases by a fully nonlinear solver. The specific solver used here is waveFoam, an extension of the OpenFOAM basic interFoam two-phase flow solver.

$$\frac{\partial \rho \mathbf{u}}{\partial t} + \nabla \cdot [\rho \mathbf{u}\mathbf{u}^T] = -\nabla p^* - g \cdot x \nabla \rho + \nabla \cdot [\mu \nabla \mathbf{u} + \rho \tau] + \sigma_T \kappa_(\gamma) \nabla \gamma \tag{4.7}$$

$$\nabla \cdot \mathbf{u} = 0 \tag{4.8}$$

$\mathbf{u} = (u,\ v,\ w)$ is the velocity field in Cartesian coordinates, p^* is the pressure in excess of the hydrostatic, g is the acceleration due to gravity, μ is the dynamic molecular viscosity and τ is the specific Reynolds stress tensor. Further information regarding the implementation of the specific Reynolds stress tensor can be found in Jacobsen et al. (2012). The last term takes into account the effect of the surface tension coefficient σ_T and the surface curvature κ_γ but their presence is of minor importance in civil engineering applications.

For the spatial discretization, OpenFOAM uses an Eulerian approach where the grid remains still with the observer and the water particle are free to move through it. In this thesis, the x-axis is positive in the direction of propagation of the waves and the z-axis is positive upwards.

In OpenFOAM the fully non linear Navier-stokes solver is combined with a volume of fluid (VOF) surface tracking scheme, described in Hirt and Nichols (1979). The free surface is tracked using a scalar α which varies between 0 and 1, where 0 corresponds to the air phase and 1 to the water phase. OpenFOAM uses an improved version of this technique where the distribution of this parameter is modelled by means of the equation:

$$\frac{\partial \alpha}{\partial t} + \nabla \cdot [\mathbf{u}\alpha] + \nabla \cdot [\mathbf{u}_r \alpha (1-\alpha)] = 0 \tag{4.9}$$

where u is the previously computed velocity field and u_r is a relative velocity. The last term on the left-hand side is an addition to the original advection equation suggested by Hirt and Nichols (1979) and it aims to reduce the smearing of the interface. This improvement is developed by OpenCFD®, and it is documented in Berberović et al. (2009). Using the α-field one can then determine the variation of a generic fluid property Φ (such as μ and ρ) by means of the expression:

$$\Phi = \alpha\Phi_{water} + (1-\alpha)\Phi_{air} \tag{4.10}$$

This method in any case originates a set of cells in which the value of α is between 0 and 1 excluded. This can constitute a problem if a specific value of the surface elevation is needed but a solution can be obtained for instance by means of the wave gauge functionality introduced by wave2Foam. Numerical wave gauges can be defined at several location of the domain that compute the free surface η as:

$$\eta = \int_{z_0}^{z_1} \alpha \, \mathrm{d}x - h \tag{4.11}$$

Here z_0 and z_1 are the extremes of a vertical line that constitute the wave gauge and h is water level at still water conditions.

4.2.2. Turbulence modeling

Turbulence modeling is a controversial aspect in the case of wave loads for non-breaking irregular waves. As shown in Capel (2012b) and Christensen et al. (2015), the inertia was dominating over the drag for the determination of the total force. The magnitude of the drag coefficient C_D is associated to the development of the turbulent boundary layer on the surface of the object and vortex shedding. Given that the drag force was observed to be small, for those cases turbulence modeling was actually not a crucial aspect. The application of a complex turbulence closure would have not been necessary.
In the case of solitary waves, it is shown in chapter 5 and 6 that the drag plays a more important role. Therefore for part of the simulations presented in this study, a turbulence model is applied for the specific purpose of capturing the loads on the submerged structure.

The turbulence model applied in the present thesis is a variation of the k-ωSST model presented by Menter (1993). Differently from the original version, here, the importance of the density variation between the two immiscible phases is taken into account to avoid severe diffusion of turbulent energy production across the surface. The variables it involves are, (just as in the original version) the turbulent kinetic energy k and the specific rate of turbulent energy dissipation ω.

4.2.3. Boundary conditions

In order to solve the differential equation of the fluid motion, boundary conditions need to be defined for the variables used in the numerical schemes, namely α, p^*, and $\mathbf{u}$.
In OpenFOAM the surfaces that delimit the numerical domain are named patches.
In the present study, the analysis starts with a simple 2-dimensional case in which the only patches are the sides of a flume slice (only one cell in the y-direction), an inlet, an outlet, the atmosphere and the bottom. This set-up is used to define the characteristics of the background mesh and to check the convergence of the model for the wave propagation and shoaling. No turbulence closure is applied here.

Once the convergence study is completed the third dimension and the .stl surface of the velocity cap are added. As shown in figure 4.5, the cap is split in three parts (top part, cylinder and base plate) in order to analyze the forces on the different components.

In the 3-dimensional set-up the boundary conditions for inlet, outlet and side walls stay the same as for the 2-dimensional case. On the patches that constitute the bottom of the flume and the velocity cap, the boundary conditions vary depending on whether a turbulence closure is applied or not.
In the case no turbulence model is used, the boundary conditions are the ones of a rigid wall with slip condition on the bottom and no-slip on the patches of the velocity cap.
In the cases where turbulence is applied, besides the three variables already mentioned, additional variables

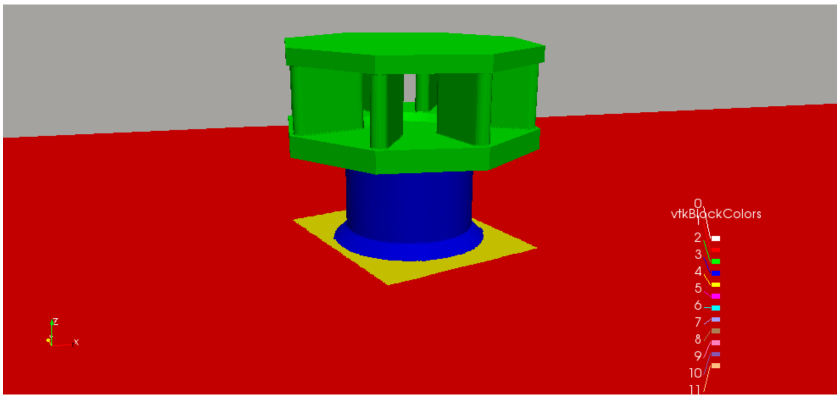

Figure 4.5: Visualization of the several patches which are split in for the purpose of the analysis . In red the bottom of the flume and in gray the side wall.

are given boundary conditions. These are treated with wall functions, which avoid resolving directly the regions closest to the wall (namely the viscous and buffer layers).

The applied boundary conditions can be summarized as follows:

- **Inlet**. At the beginning of the domain, the **u** field and the α parameter are defined by the potential flow solver OceanWave3D.
- **Outlet**. At the end of the domain the waves need to exit avoiding reflection as much as possible. This is implemented with a Sommerfeld boundary conditions recently developed in OpenFOAM by Niels G. Jacobsen (Researcher/advisor at Deltares).
- **Side walls**. The sides of the domain are modelled as rigid walls applying slip condition to the velocity field.
- **Atmosphere**. Atmospheric boundary condition.
- **Bottom and velocity cap**. The correct bathymetry of the flume is generated by means of a .stl surface. The geometry of the cap (also imported in the domain as a .stl surface) is split in three parts (top cap, support cylinder and base plate).
  - *Laminar simulation* The resulting patches are treated again as a rigid wall with slip condition for the velocity field.
  - *Turbulence model applied* The patches are treated as rigid walls with no-slip condition for the velocity field. Turbulent properties are defined with specific wall functions.

The generation and absorption of the waves at the boundaries is done utilizing the toolbox waves2Foam. The particular value of waves2Foam for the present application is that it allows the user to couple the original CFD environment with another solver that works on wave generation and propagation (OCW3D) by means of relaxation zones. The next two sections elaborate more on the conditions applied at the inlet and outlet. Figure 4.6 gives a schematic representation of these two zones.

RELAXATION ZONES

A key feature of the wave toolbox waves2Foam consists in the implementation of relaxation zones able to prevent wave reflection from the outlet boundary or to avoid that internally generated waves interfere with the wave generation at the inlet. In the present model only one rectangular relaxation zone is used at the inlet. In this zone the fields α and the velocity are updated at every time step according to the expression:

$$\Phi = \alpha_R \Phi_{target} + (1-\alpha_R)\Phi_{computed} \tag{4.12}$$

where Φ can be one of these two quantities. In the schematic of figure 4.6 the variation of the α_R parameter is shown as a function of the local coordinate χ_R. The dependency is described by the expression:

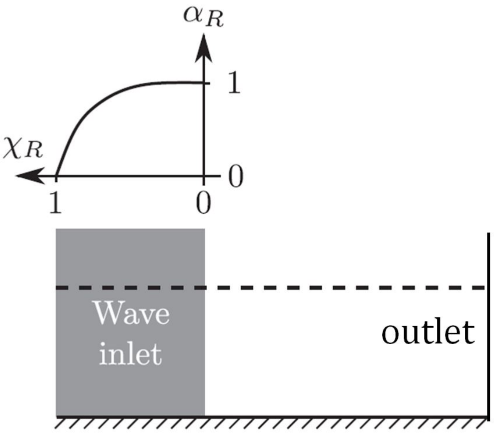

Figure 4.6: Schematic of the relaxation zone at the inlet and the outlet

$$\alpha_R = 1 - \frac{e^{\chi_R^{3.5}} - 1}{e - 1} \tag{4.13}$$

The target values are the ones defined by the potential flow solver OceanWave3D presented in section 4.1, while the computed ones are the numerical results of the Navier-Stokes/VOF solver. The target solution is provided on the time axis generated by OCW3D. By means of waves2Foam, the user can then select a segment of the time axis of OCW3D to start and stop the more expensive CFD simulation.

The introduction of relaxation zones makes the coupling between the two models described in this chapter possible: OCW3D and OpenFOAM. Outside the computational domain of OpenFOAM, the solution is computed by the potential flow solver that is much faster than the Navier-Stokes/VOF solver. Only inside the smaller OpenFOAM domain the solution is computed also by the N-S/VOF solver. The link between the two models is possible through the relaxation zones where gradually the solution computed in the outer domain is used as a target solution for the more complex computations performed by the N-S/VOF solver (Paulsen et al., 2014). This is known as the one-way domain decomposition strategy. Other applications of this strategy can be found in Paulsen (2013) and in Bruinsma (2016).

SOMMERFELD CONDITION

At the outer boundary the definition of a relaxation zone is not necessary. The only requirement is to let the wave exit the VOF domain without reflection. The condition used is a Sommerfeld radiation condition which is defined as weakly reflective. This means that reflection is not fully prevented but as far as the inner VOF domain ends far enough from the structure under analysis, the said condition performs good enough (i.e. the weak reflection of the wave does not influence the loads of the velocity cap). Therefore, the boundary condition applied at the outlet reads:

$$\frac{\partial \phi}{\partial t} + c\frac{\partial \phi}{\partial x} = 0 \tag{4.14}$$

where $c = \xi\sqrt{gh}$. The constant ξ is a parameter introduced to take into account possible discrepancies between the theoretical shallow water wave celerity ($\sqrt{gh}$) and the actual propagation speed of nonlinear waves. In the case of a solitary wave, the wave celerity is defined as $c = \sqrt{g(h+H)}$ where h is the water depth and H is the height of the solitary wave over the mean water level. A sensitivity analysis showed that varying this parameter in the range between 1 and 1.3 did not result in appreciable variations of the loads on the cap in the tested set-up.
In the simulations presented in the following chapters this parameter is set equal to 1.075.

NEAR-WALL TREATMENT

Near-wall regions need to be modelled with particular care in order to generate accurate results from the point of view of turbulent properties. In the simple case of a steady current in an open channel where turbulence is fully developed, the whole water column can be divided in three layers. The closest to the wall is called viscous sub-layer because of the strong importance that molecular viscosity has at this short distance from the wall. Moving away from the wall, the relative importance of molecular viscosity decreases and inertia starts dominating the flow allowing turbulence to develop; this is called logarithmic or log-law region. In between the two regions the so called buffer layer is a region where the first behaviour gradually switches to the second.
In literature, the parameter used to describe the wall distance and therefore the passage from one region to another is y^+ (see for instance Pope (2000)). This parameter expresses the non-dimensional wall distance according to the following equation:

$$y^+ = \frac{y u_\tau}{\nu} \tag{4.15}$$

where u_τ is the friction velocity defined as $\sqrt{\frac{\tau_w}{\rho}}$ with τ_w the wall shear stress. y is the distance to the wall in meters which, in a CFD context, assumes the meaning of the distance of the first cell center from the wall. There is the following agreement between experts (Pope (2000), Nieuwstadt et al. (2016)):

- $\mathbf{y^+ < 5}$ corresponds to the viscous sub-layer.
- $\mathbf{5 < y^+ < 30}$ corresponds to the buffer layer
- $\mathbf{30 < y^+ < 300}$ corresponds to log-law region.

When solving the flow by means of a Navier-Stokes/VOF solver, refining the grid down to the viscous sub-layer thickness can pose a severe limitation to the stability of the solver or to its speed because of the smaller time step needed. This would mean that the fist cell center is at a distance from the wall such that $y^+ < 5$.
The preferred approach is then the use of wall functions. Wall functions are empirical equations used to satisfy the physics of the flow in the near wall region. As a consequence, the first cell center can be placed in the buffer layer. In this way instead of computing directly the turbulence properties and momentum transport down to the wall itself, the wall functions provide boundary conditions that link the fully turbulent region and the inner viscous layer (Tu et al., 2008; 2013).

OpenFOAM offers a number of wall functions defined for different applications. In the present study, the factors that influence the choice are:

- The flow is unsteady and the y^+ changes in space and in time.
- It is computationally expensive to use a mesh fine enough to always retain y^+<5 on all the patches of the velocity cap.

This lead to the choice of the following wall functions for the three different turbulence variables:

- k, $kLowReWallFunction$. This wall function is particularly suitable for the present application. Even though the name can mislead, this function is defined to perform well both in case of low and high local Reynolds number. This means that as far as the first cell center is at least inside the buffer layer ($y^+ <$ 30) the function is able to predict a reliable value of k.
- ω, $omegaWallFunction$. In the case of omega OpenFOAM offers a single wall function which benefits from the fact that this quantity is known for the viscous sub-layer and for the log-law region. The function is based on the blending expression suggested by Menter and Esch (2001).
- $\nu_\mathbf{t}$, $nutUspaldingWallFunction$. This wall function takes advantage of the unique expression for the relation between y^+ and u^+ (non-dimensional velocity) proposed by D. B. Spalding in 1961. This equation fits the behaviour of u^+ in the whole region, from the log-layer down to the viscous sub-layer. Note that ν_t is not needed as a variable for the computations but is tracked because of the importance for the OpenFOAM utility $yPlus$. This uses the estimate of y^+ determined by the wall function specified for the ν_t field.

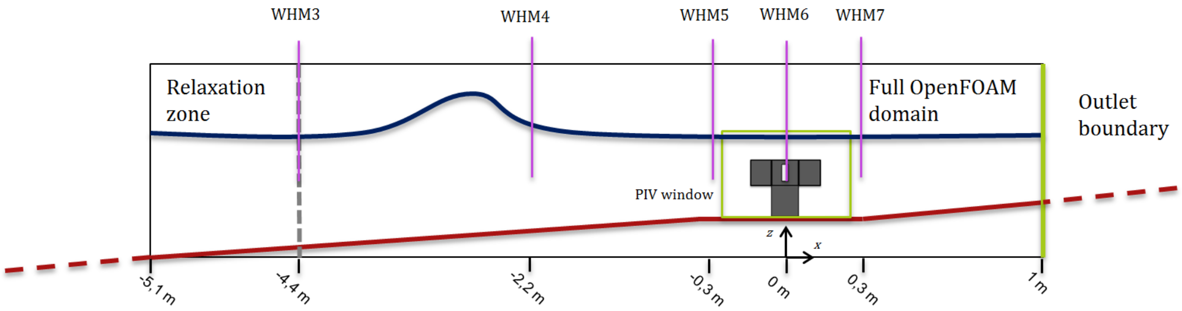

Figure 4.7: Sketch of the domain size and positions of the wave gauges and of the cap in the test cases regarding solitary waves (excl. T103).

These wall functions could predict well the turbulence properties in situation where y^+ was ranging between 0 and 30 approximately. More information about the implementation of the specific wall functions can be found online at openfoam.org or in the paper by Liu (2016).

4.2.4. Domain size

The coupling with the solver OCW3D allows to make the domain as small as possible so to reduce the computation time. The propagation of the waves along the flume in fact can be better modelled in a potential flow solver for the sake of time. The only constraint is that OCW3D cannot reproduce turbulence due to the interaction with the structure nor due to wave breaking. Hence, the space around the velocity cap from the location where breaking was observed to approximately five diameters ($5 \cdot D$) after the cap are discretized and solved in OpenFOAM.

The test during which breaking was observed the farthest from the structure was T103, when the solitary wave broke at approximately the fourth wave gauge (see fig. 4.4). Given that that wave gauge is at - 4.4 m in front of the cap, in order to include some margin for the relaxation zone, the offshore boundary is located at - 5.1 meters. Only for the test case T103, does placing the offshore boundary at -7.1 m improve the prediction of the location of breaking. Therefore for that test case, the domain is longer.
The boundary ideally closer to the shore is instead 1 meter after the cap in order to make sure that the weak reflection associated to the Sommerfeld condition does not affect the loads.

At the position of the flume where wave gauges were used in the physical model tests, numerical wave gauges are also defined in order to have a direct comparison with the experiments.

4.2.5. Convergence study

The finite volume discretisation used in OpenFOAM® is based on unstructured grids consisting of arbitrary convex polyhedrals. In the present work, it can be made a distinction between background mesh and refined mesh. The former is generated by the utility *blockMesh* and it has the coarsest dimension of the grid cells far from the structure, while the latter is the finer mesh obtained by means of the utility *snappyHexMesh* refining the background mesh. The criterion used to determine the dimension of the background mesh is the convergence by grid refinement of the propagation of the solitary wave and the comparison with the surface elevation measured during the experiments.
The aspect ratio of the hexahedral cells generated by *blockMesh* is maintained equal to 1 because, as observed by Jacobsen et al. (2012), a higher ratio is responsible for a wrong prediction of the position of wave breaking.

The convergence study is based on test case T101. Figure 4.8 shows the relative error obtained with different refinement of the background mesh.

In a similar way to the computation of the RMSE in the case of the OCW3D, the error is computed as:

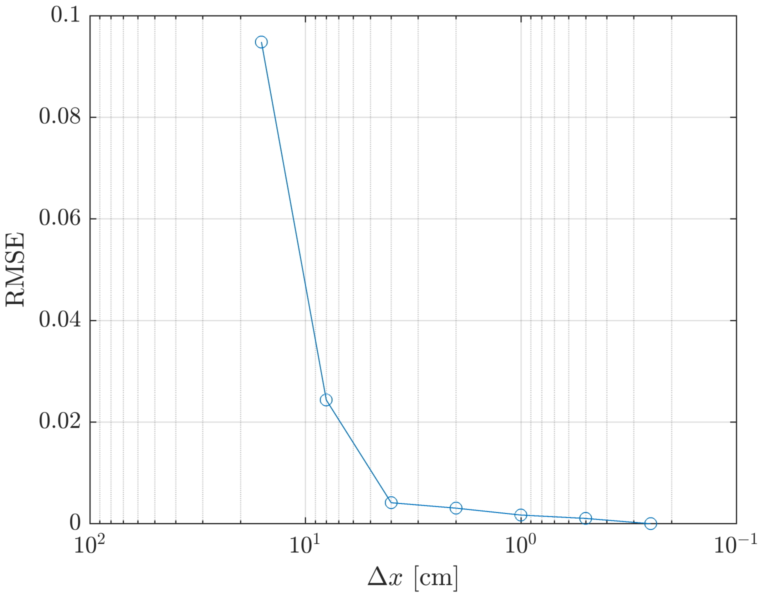

Figure 4.8: RMSE error computed for the different grid sizes of the background mesh (previous to refinement). Result relative to test T101.

$$RMSE_{\Delta s=x} = \frac{\sqrt{(\eta_{\Delta s=x} - \eta_{\Delta s=2.5})^2}}{\eta_{\Delta s=2.5,max}} \tag{4.16}$$

where Δs is the side of the hexahedral cell.

As shown in table 4.4, the error is already approximately 0.3 % with a background mesh with Δs of 2 cm. A finer mesh is therefore considered unnecessary. On the other hand, a coarser mesh of 4 cm, also attractive from the point of view of the small error, is discarded. The reason is that, as explained in chapter 5, the refinement of the mesh around the cap determines a big variation of the cell size between near and far from the structure. A too big variation could have consequences in the reconstruction of the flow field and therefore it is avoided.

Table 4.4: Overview of the background mesh grid sizes used for the OpenFOAM computations relative to test T101 and the respective errors.

Δs [mm]	160	80	40	20	10	5	2.5
$RMSE_{\Delta s=x}$ [%]	9.5	2.4	0.4	0.3	0.2	0.1	0

4.2.6. Wave celerity prediction

It has been noted that the wave celerity is not perfectly computed by the potential flow solver OCW3D. Also in the case of the N-S/VOF solver the wave celerity is slightly different from what recorded during the experiments. Table 4.5 reports the wave celerity computed at WHM6 for both the experimental records and the OpenFOAM results. The celerity is estimated as the ratio between the distance between WHM5 and WHM 7 and the time needed to the wave crest to travel from WHM5 to WHM7.

Table 4.5: Wave celerity at WHM6 as computed by the model and as obtained from the experimental records. Breaking cases are reported in red. Test case T303 is not considered as a breaking case because the wave was breaking right after the cap, however, the location of breaking is slightly different in physical model tests and in the numerical simulation and this influences the computation of the wave celerity.

	T101	T102	T103	T201	T202	T203	T301	T302	T303
Experiments	2.33	2.64	4.95	2.47	2.83	2.47	2.64	2.83	3.05
OpenFOAM	2.20	3.14	3.67	2.27	2.75	3.88	2.36	2.64	2.64

The analysis of the surface elevation plots clarifies that the dynamics at the wave crest are not perfectly predicted even if the match between the numerical and the experimental records is overall good (see figure 4.9). In the non-breaking cases the wave at the velocity cap is undergoing a small decrease in wave height which is not captured by the model. It is probably due to this discrepancy that the local wave celerity at the sixth wave gauge is also showing a small difference.

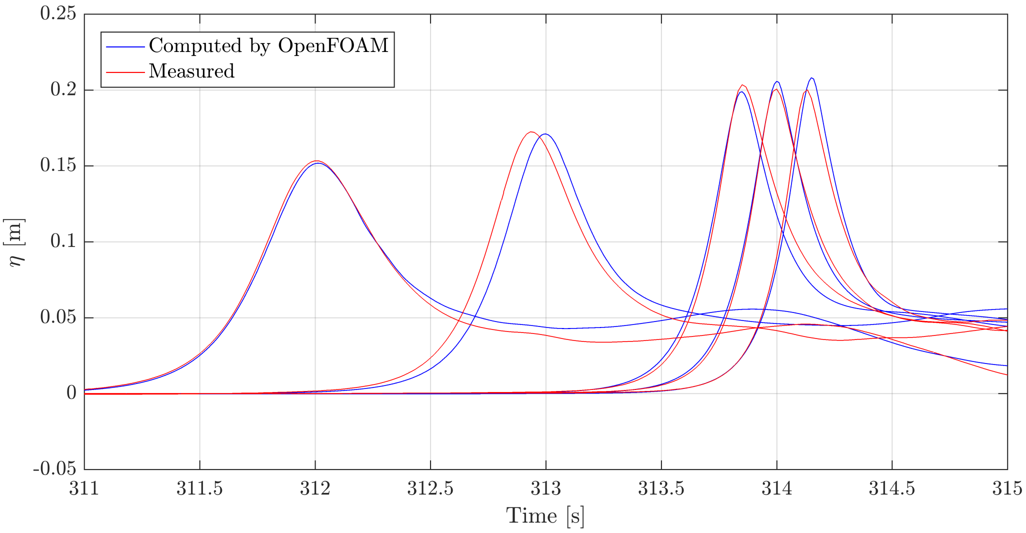

Figure 4.9: Match between surface elevation computed by the N-S/VOF solver and measured for test case T101. Given the dimension of the OpenFOAM domain only wave gauges WHM3, WHM4, WHM5, WHM6 and WHM7 were included.

5

Validation of the OpenFOAM model

In chapter 4, the water surface elevation predicted by the model has been validated in terms of convergence by grid refinement and by comparison to the experimental records. Here, the validation is extended to the force signals. A good agreement between numerical results and measurements is found for the inline force. The lift force prediction shows perfect agreement with regards to the phasing, but the peak value is not accurately predicted, possibly due to a bias in the experimental records.

At the end of the chapter a direct comparison between PIV measurements and OpenFOAM results is also presented. The velocity field from the model (analyzed in the x-component only) compares well with the measurements except for the prediction of the boundary layer development at the top leading edge of the velocity cap and in some locations in the jet coming out of it at the trailing side.

5.1. Synchronization

The comparison with the experimental measures is the key aspect used in this chapter to achieve the validation of the model. In order to enable a comparison, the numerical and the experimental time axis are synchronized to match the shape of the wave profile (surface elevation) at the location of the velocity cap (sixth wave gauge).

This synchronization is implemented in two steps. First, the time axes are roughly synchronized by matching the peak of the surface elevations. Secondly, the correlation function is computed between the numerical and experimental curve for a range of positive and negative offsets. The synchronization that results in the highest correlation is then selected for the rest of the analysis. Basing the synchronization only on matching the peaks of the surface elevation results sometimes on a relatively poor correlation between measurements and numerical results. This happens because in some cases the computed and measured wave profile has a slightly different steepness and skewness, which leads to a mismatch of the location of the wave crest in the wave profile.

5.1.1. Limitation of the synchronization method

Matching the time axes only based on the property of the wave at the sixth wave gauge has the limitation of neglecting wave celerity differences between experiments and numerical models, which in section 4.2.6 were shown to be present.

However this type of synchronization makes sure that the comparison between numerical results and experiments is consistent for any phase of the wave. This is particularly important when comparing the velocity field of the wave (see section 5.4) but above all it is important when studying the decomposition of the forces between drag and inertia components which is presented in chapter 6.

5.1.2. Links between time axes

Once the surface elevation computed by the N-s/VOF solver is synchronized with the experimental measures, all other field variables such as velocity estimate and forces are automatically synchronized as well. As described in figure 5.1, all the experimental time axes are already adjusted to correlate with each other during the experimental phase (see ch. 3). The numerical time series instead are all based on the OCW3D computations. The N-S/VOF solver in fact uses the segment of the time axis of OCW3D specified by the user, as described in section 4.2.3.

It is important to note that this procedure was needed to correlate two sets of time series otherwise unrelated: on one side the experimental ones and on the other the numerical ones. The diagram of figure 5.1 shows more visually the relationships between the several time axis.

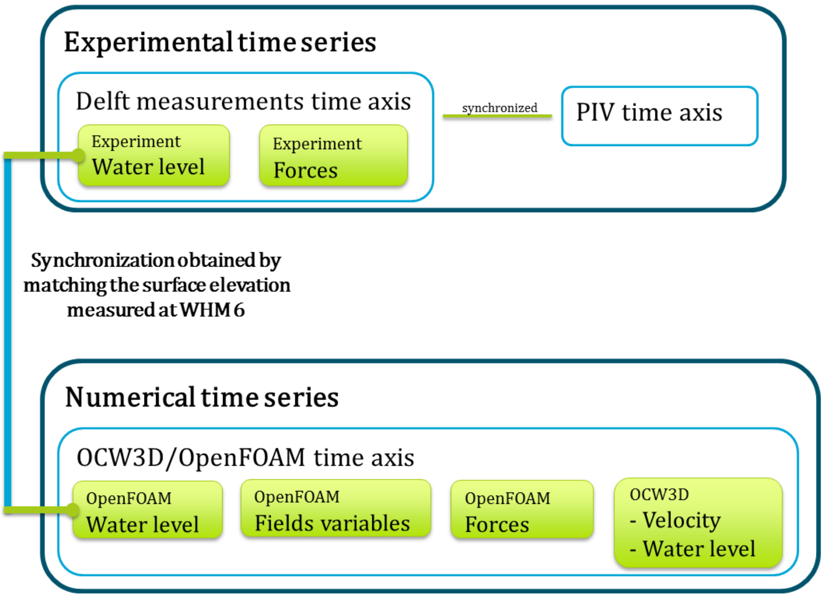

Figure 5.1: Relationships between the time axes of the different time series used during this study.

5.2. Laminar simulations

The numerical investigation started without including any turbulent closures and applying slip conditions on all wall patches (side walls, bottom and cap patches). In this way the flow is assumed to be laminar everywhere in the domain and the viscous boundary layers are neglected.

This is done because the development of turbulence does not significantly affect the load prediction in case of inertia-dominated regimes. In order to have such a regime, the KC number needs to be small ($0 < KC < 20-30$ (Sumer and Fredsøe, 2006)), which means that the excursion of the water particles is small compared to the dimensions of the structure under analysis. If this is the case, vortex development around the structure and their shedding stay contained and do not influence the loads. For the sea states analyzed for civil engineering purposes, KC mostly falls in this range.

Moreover, a turbulence closure requires often a very fine mesh near the solid boundaries, which increases considerably the computational time, and this explains why running laminar simulations is a common approach in offshore applications (see for instance Paulsen et al. (2014) and Bruinsma (2016)).

5.2.1. Experimental bias and pressure correction

The raw OpenFOAM outputs include the hydrostatic pressure component and therefore even before the wave is arriving, the vertical force has a constant negative value. During the physical model tests, the force sensors were zeroed in presence of water and this component is not visible in the records. Hence, in order to compare the results, the initial value of the vertical force of the OpenFOAM results is subtracted from the total signal.

The first obtained results show a consistent underestimation of the inline force peak and overestimation of the vertical force as can be seen in the graphs of figure and 5.2.

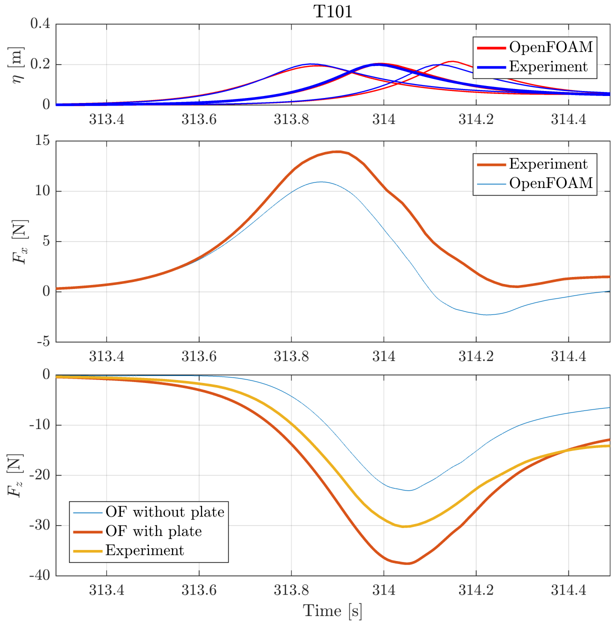

Figure 5.2: Comparison of the experimental and numerical estimate of the forces for test case T101. Laminar simulation with slip condition applied on the cap patches.
Top panel: water surface elevation at WHM 5, 6 and 7. The thicker lines correspond to the surface elevation at the velociy cap (WHM 6).
Mid panel: inline force.
Lower panel: vertical force. The OpenFOAM plots show the results both including and excluding the force component on the patch of the base plate. This is done because the inclusion of the base plate has only relevance for the validation of the results in terms of comparison with the experimental measurements. In real applications the base plate is not a part of the velocity cap.

The reason for this mismatch is partly attributable to a bias in the experimental measures. As already introduced in section 3.3.1, the velocity cap needed to be free to move slightly in order for the force sensor to register a force. The small openings between the base of the cap and the rest of the wooden frame, however, could have allowed a flow of water or at least the transmission of the pressure from above to beneath the base plate.

Figure 5.3 is a detail of the force sensors set-up shown in figure 3.4. The blue arrows show the possible infiltration of water in the opening. Therefore, an algorithm is implemented in order to determine what the additional effect of the water pressure on the sides of the base plate and on the lower surface is.

The pressure computed with the Navier-Stokes/VOF solver is probed on 200 equally spaced points along the sides of the base plate as shown in figure 5.4. The outputs of the probes are then used in MATLAB to determine two components of the pressure correction:

1. A force component parallel to the plane of the base plate (inline) computed as the integration of the probed pressure over the thickness of the base plate (25 mm, see fig. 5.3).
2. A complete pressure field under the cap computed by means of linear interpolation of the scattered points (see figure 5.5). The integral of this field over the colored area of figure 5.5 gives the force component perpendicular to the base plate (vertical). The white area that is not considered corresponds approximately to the width of the force sensors box.

The definition of the area under the velocity cap (white area in figure 5.5) is potentially a tuning parameter to get a better match for the vertical force. However in the present study, it is preferred to focus on the validation based on the inline force which is more relevant for the design and whose measurements are less affected by the set-up bias during the experiments.

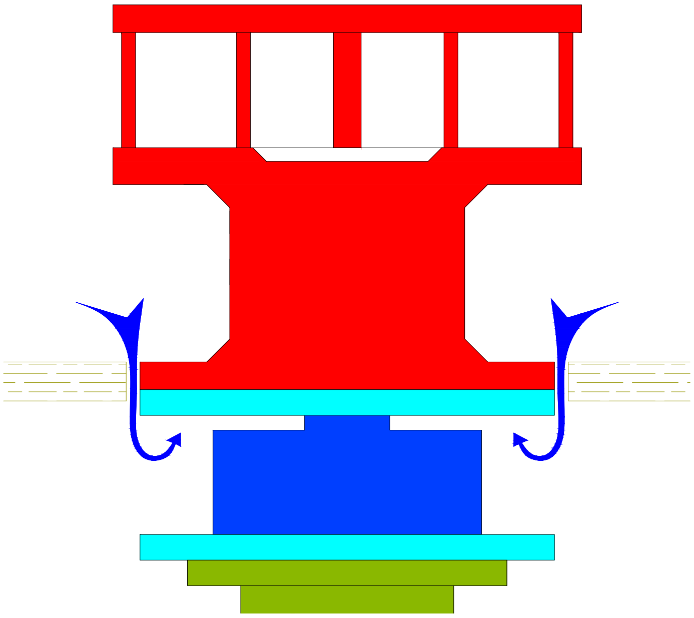

Figure 5.3: Drawing of the gaps between the base of the cap and the rest of the wooden frame constituting the bottom of the flume. The force sensor were water-proof and all the part of the flume below the wooden frame was also filled with water.

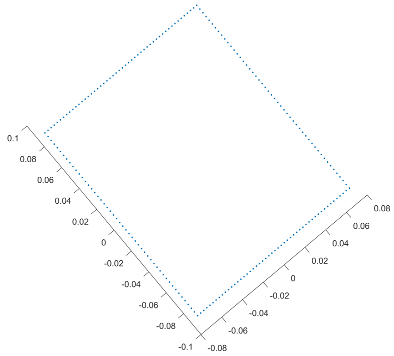

Figure 5.4: Probed points at the location of the sides of the base plate. For each point a time series of the total pressure is output during the simulation.

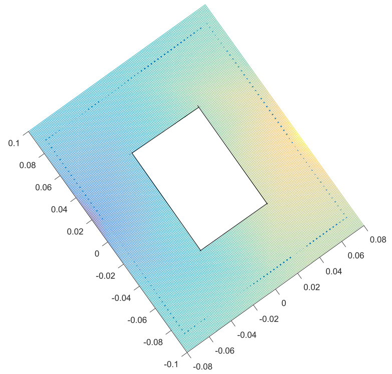

Figure 5.5: Pressure field obtained by interpolating linearly the pressure probed at the contour.

5.2.2. Force estimate

In the rest of the document the force estimates obtained by subtracting this correction to the raw force measurements are called corrected force estimates. In figure 5.2 and in the next plots the corrected force estimates can be observed. The improvement is considerable for both horizontal and vertical component. However, even if for case T101 the match of the predicted downward force between numerical and experimental estimate is particularly good, the observation of other test cases shows that using the same algorithm for the pressure correction still produces an error in the prediction (see lower panel of figure 5.8).

Looking at the shape of the mid panel of graph 5.6, it can be noted that not only the peak of the model prediction is underestimating the measurements, but it also occurs slightly earlier. In particular, the prediction of the force evolution is fairly good when the force is increasing, but really poor with underestimation of 50 % or more when the load is past the peak.
Recalling the phasing between inertia and drag component in the Morrison equation, in the case of a per-

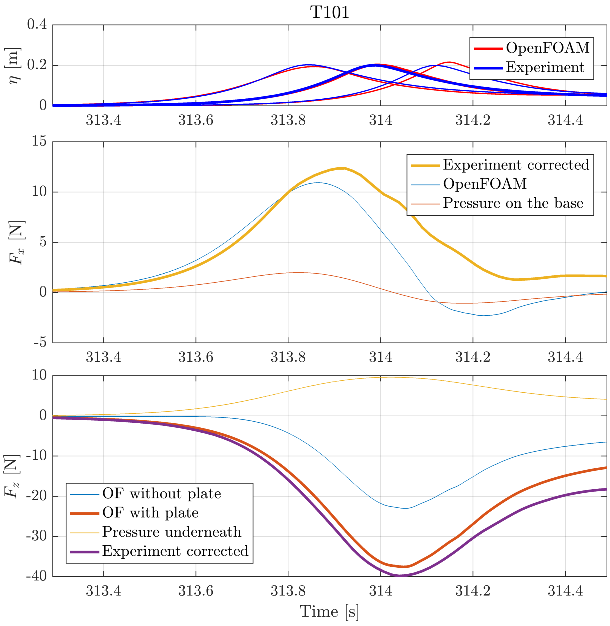

Figure 5.6: Comparison of the experimental and numerical estimate of the forces for test case T101. Laminar simulation with slip condition applied on the cap patches. In this plot the correction is subtracted form the experimental record. The summation of the orange and red curves results in the plot of the original measurements as plotted in figure 5.2.

fectly sinusoidal wave the inertia precedes the drag with a quarter of a period (see fig. 2.1).
The particular shape of the OpenFOAM results leads to the hypothesis that the inertia is captured in an appropriate way but the drag is not. Assuming that the flow is laminar means accepting that the viscous forces that constitute most of the drag component are not captured accurately, given the lack of a turbulence closure and the application of slip conditions. If the inertial loads are dominant over the drag, the assumption of laminar flow can still give good results but In the case of solitary waves it is observed that a turbulent closure is needed.

A more careful observation of the relation between the shape of the incoming wave and the force prediction supported the idea that inertia is well predicted by the model while drag is underestimated. When the solitons assume the shape of a steep breaking wave or of a bore with a steep front, in fact, the acceleration is higher than in the case of a smooth wave. Case T203, where the wave was breaking right at the cap, shows that if the loads are dominated by the acceleration, the laminar model gives fairly good estimate of the inline force peak (see figure 5.7).

On the contrary test T301 generated the smoothest wave of the set and the underestimation of the force peak is the most considerable (see mid panel of figure 5.8).

5.3. Reynolds Averaged simulations

The last step towards the validation of the present CFD model consists in running Reynolds averaged simulations (RAS) using the formulation of the k-ωSST turbulence closure described in chapter 4. Test case T301 that which showed the largest error for the force prediction in the laminar simulations, is used here as example. Appendix E shows the plots for all the test cases.

5.3.1. The importance of the grid refinement

In order to meet the requirements described in section 4.2 with regards to y^+, a mesh fine enough close to the structure needs to be generated. The OpenFOAM utility used for the mesh refinement is *snappyHexMesh*. This utility allows to define the levels of background mesh refinement and the addition of cell layers close to

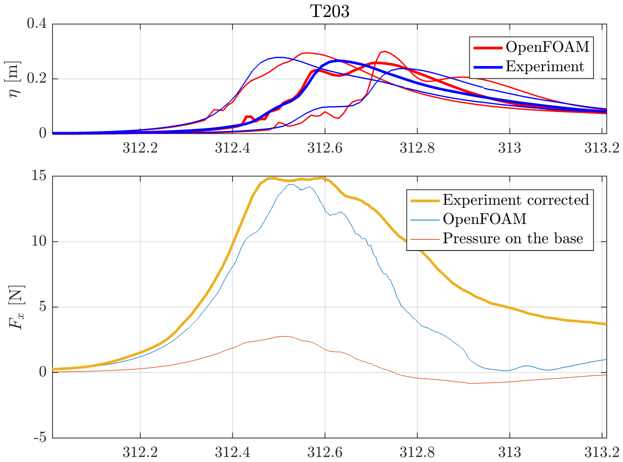

Figure 5.7: In line estimate for the breaking test case T203. Laminar simulation with slip condition applied on the cap patches.

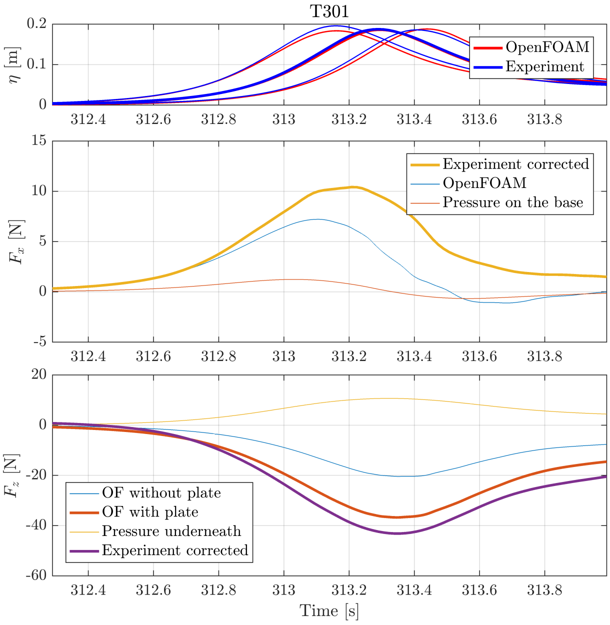

Figure 5.8: Comparison of the experimental and numerical estimate of the forces for test case T101. Slip condition applied on the cap patches. The error between the measurements (corrected) and the model results reaches 16 % at the negative peak of the force.

a structure in order to be precise in the definition of the dimension of the first cell center height. The first cell thickness was set to 0.12 mm. Such a mesh is suitable to estimate the viscous forces on the structure, is shown in the next section. However it must be noted that the requirements for y^+ are not met everywhere on the patches of the cap.

Figure 5.9 shows visually where y^+ is below 30 during an instant of the T301 simulation. On oblique sharp edges and on curved surfaces in fact *snappyHexMesh* fails in adding the cell layers. The reason for this behaviour of the utility is not analyzed further seen the overall good level of layer addition.

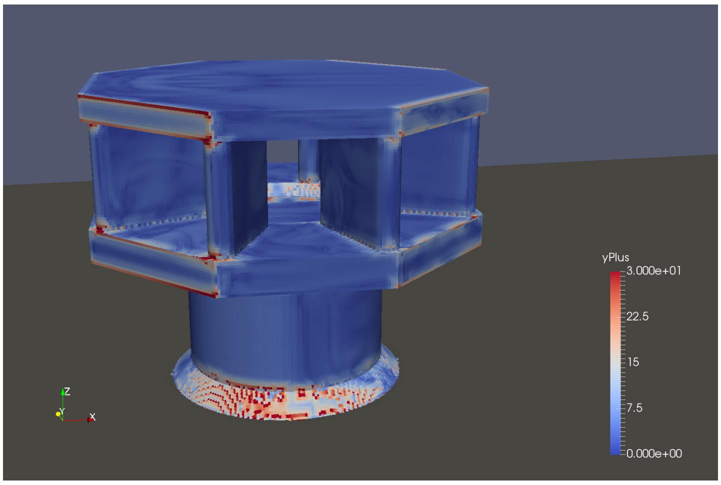

Figure 5.9: Visualization of the value of y^+ computed on the cap patches (screen-shot taken from ParaView). Results relative to test case T301. Any dark red point indicates a location where y^+ is above 30. The maximum value computed for this simulation is 52.

5.3.2. Force results

The use of the k-ωSST turbulence closure gives a much better convergence of the results in terms of match with the experimental (corrected) evidence. Figure 5.10 shows the results for test T301

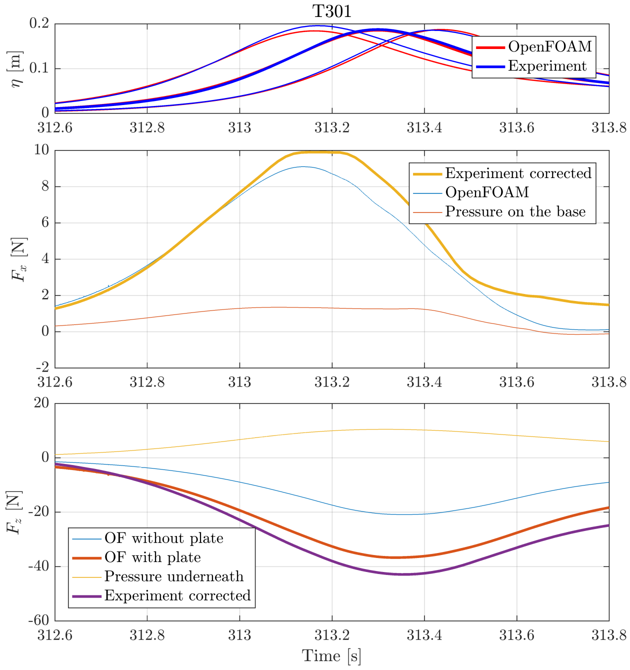

Figure 5.10: Results of the RAS computations for test case T301.

Figure 5.11 and table 5.1 give an overview of the relation between the computed and measured corrected forces. The error between these two estimates is computed as

$$\epsilon = \frac{\sqrt{(F_{exp,peak} - F_{OF,peak})^2}}{|F_{exp,peak}|} \tag{5.1}$$

The magnitude of the relative error for the inline force estimate is overall smaller than the case of the vertical force. However, very little can be said with regards to the breaking cases (T102, T103, T203). Even if the location of breaking is in relatively good agreement with the experimental measures, the hydrodynamics are too chaotic to be able to compare the prediction of the model with the measurements. One last note is that T103 and T203, which are the cases where the wave was already breaking in front of the cap, are better modelled in the laminar simulation than in the RAS.

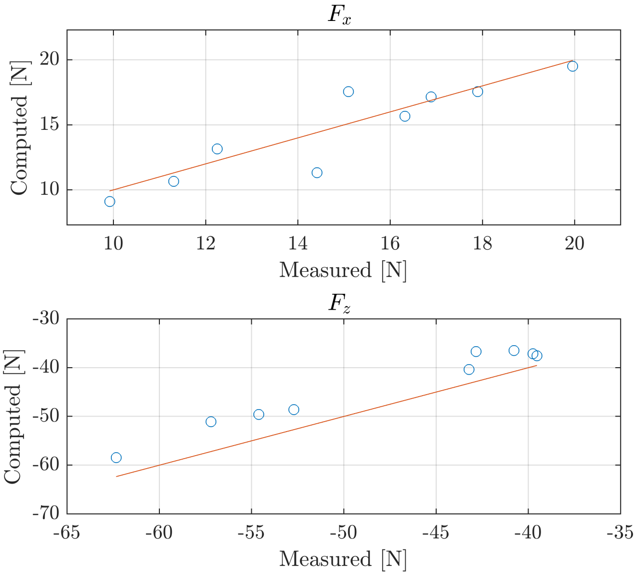

Figure 5.11: Plot of the computed peak force against the measured one. The red line is included as a reference for the 1:1 line.

Table 5.1: Relation between computed and measured results. The relative error between computed and measured forces is expressed in percentage. The results reported in red corresponds to the test cases in which breaking was observed.

Test case	$\epsilon(F_x)$ [%]	$\epsilon(F_z)$ [%]
T101	7.37	5.04
T102	1.61	6.63
T103	21.43	6.53
T201	5.92	10.51
T202	1.89	9.18
T203	16.31	7.79
T301	8.24	14.34
T302	4.00	10.72
T303	2.21	6.27

5.4. Comparison with the PIV measurements

In order to visualize and present the numerical results, the data analysis and visualization application ParaView[1] is used. Among the functionality of this software, the user can choose to cut the domain and visualizing slices of the flow field plotting any of the variables computed by the solver.
Such a feature can be used to operate a direct comparison between the PIV measurements taken during the experiments and the numerical results. For this purpose the full fields (p^*, $\mathbf{U}$, α, k, ω, ν_t) saved every 0.1 seconds in the OpenFOAM time directories could be processed in ParaView. In particular, the results regarding the u component of the velocity field, on the same plane where the PIV measurements were taken, were exported as .csv tables for further manipulation in MATLAB.

The different spatial discretization of the information differs for the two data sets (uniform grid with spacing 2 or 4 mm for the PIV measurement and variable grid depending on the level of refinement for the model

---

[1] Version 4.4.0 64-bit

results). This problem is overcome by interpolating the results on a uniform grid with spacing 3 mm for plotting purposes.
This procedure allows plotting figures such as 5.12 and 5.13. These two plots represent velocity maps for a domain as wide as the PIV window.

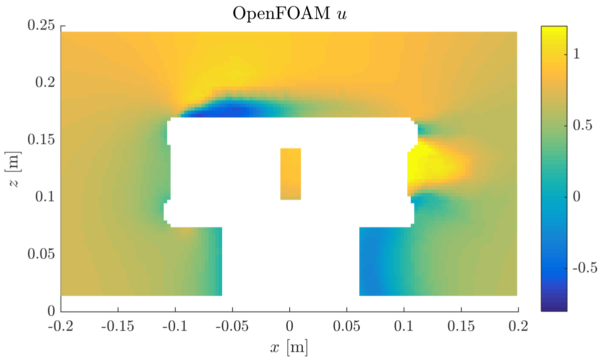

Figure 5.12: OpenFOAM horizontal velocity estimate for test T201.

5.4.1. Synchronization analysis

The effort of interpolating the results on the same grid and synchronizing the time axes allows subtracting the two velocity estimates in order to have a direct impression of which flow structures are captured by the model and where the discrepancies are the most evident.

The accuracy of the synchronization is analyzed by applying a range of time offset to the newly defined PIV time axis. Therefore, once the velocity map is extracted from one OpenFOAM time directory, the PIV velocity maps corresponding to the instants immediately preceding and following are also extracted.
The error between the numerical velocity prediction and the PIV measurements is computed in two ways for each offset considered. The first one (referred to as *er*), is a scalar and it indicates the overall disagreement between the two velocity maps, while the other one (*mismatch*) is an error field and is used in the following plots to show where this disagreement was the largest. The scalar value *er* is computed as

$$er = \iint_{PIV\,window} |u_{PIV}(x,z) - u_{OF}(x,z)|\,dx\,dz \tag{5.2}$$

The error field *mismatch* is computed as:

$$mismatch(x,z) = u_{PIV}(x,z) - u_{OF}(x,z) \tag{5.3}$$

These two error estimates are evaluated for every time offset. In particular, the minimum value of *er* is used to select which time offset gives the best correlation between PIV and OpenFOAM estimates. Shifting the time axis of the PIV measurements of three frames backwards and forwards in time allowed computing the values of *er* for a number of time directories, which are reported in table 5.2. The minimum value of the error is always found for an offset of PIV time axis of one frame. Given that the sampling frequency of the PIV measurements was 30 Hz, this corresponds to a shift in the time axis equal to 0.033 seconds.

The reason for this offset can be related to the sampling rate of the PIV. An offset of ± 1 frame can be just due to the synchronization used to align the different time axis. The fact that the best correlation between numerical results and PIV data is always found with an offset of one frame confirms that this offset is needed because of the procedure used for the synchronization and not because the model is predicting a different speed in the evolution of the velocity field.

Time directory 313.6 is now used as an example to show the comparison between numerical and experimental data. This moment in the simulation corresponds to the passage of the wave crest over the cap. The PIV velocity map to be compared with the OpenFOAM data is extracted from the frame preceding in time the one obtained with the original synchronization and it is presented in figure 5.13.

	Time offset (nr. frames)						
Time directory	-3	-2	-1	0	1	2	3
313.4	0.0066	0.0029	0.0014	0.0047	0.0082	0.0116	0.0147
313.5	0.0061	0.0030	0.0021	0.0048	0.0072	0.0088	0.0101
313.6	0.0051	0.0034	0.0033	0.0042	0.0056	0.0074	0.0094
313.7	0.0063	0.0046	0.0033	0.0042	0.0069	0.0103	0.0138

Table 5.2: Estimate of the overall disagreement (*er*) between the 7 offsetted PIV velocity maps and the OpenFOAM results. The time directories corresponding to the moments when the wave is passing over the cap are presented.

Figure 5.14 shows, in the lower panel, the error field *mismatch* computed as the subtraction between the velocity field shown in figure 5.14 and the one shown in 5.12. Warm colours are associated to zones where the model is underestimating the velocity as measured by the PIV and cold colours to the zones where it is overestimating it. The discrepancy between the experimental and numerical measures are also analyzed by plotting the velocity profiles in top two panels for representative locations in the PIV windows (just upstream of the cap and just downstream). More observations on the comparison between numerical results and PIV measurements are included in section 5.4.2.

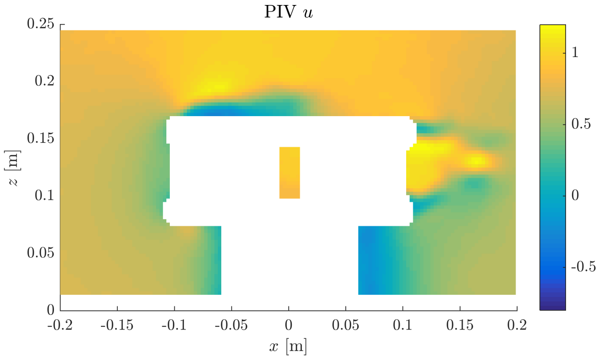

Figure 5.13: Ensemble averaged horizontal velocity computed from the PIV measurements relative to the 40 repetitions of test T201. Test case T201 was taken as a reference because the 40 repetitions of the test allowed to have the best estimate of averaged flow field.

If different time offsets are considered, the disagreement increases as shown in figures 5.15 and 5.16. This is clearly visible in the top panels that show the velocity profiles over the vertical. In the plot of the error field the difference can be seen in the slight change of the background colour.

5.4.2. Observation on the velocity field prediction

After discussing the validity of the synchronization on which the comparison is based, this section discusses how the numerical predictions of the velocity field compare with the PIV measurements. The prediction of the flow patterns is investigated analyzing the mismatch between numerical and PIV results for time directories 313.4, 313.5, 313.6 and 313.7.

The relevance of studying these time directories in the case of test T201 can be understood by considering the following information:

- 313.4 is the instant in which the flow detachment at the top leading edge of the velocity cap starts being clearly visible.
- 313.5 corresponds approximately to the peak of the inline load.
- 313.6 is the instant in which the wave crest is above the velocity cap. The peak of the undisturbed velocity at the location of the cap occurs approximately at this instant.
- 313.7 is used to show the evolution of the flow patterns right after the passage of the wave.

Figure 5.14 already showed the mismatch between measurements and numerical model for the instant corresponding to the passage of the wave on top of the cap. The analysis of this plot shows an almost prefect

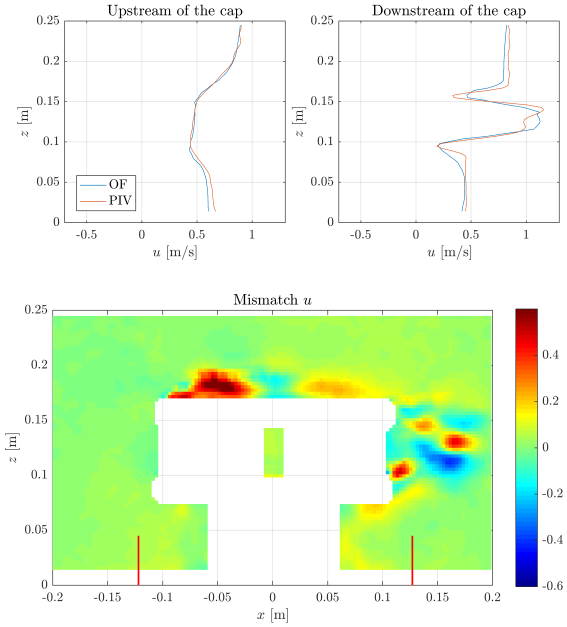

Figure 5.14: Comparison between the PIV and OpenFOAM velocity estimates for test T201 at time 313.6. The PIV velocity map used in the comparison has an offset of 1 frame (-0.033 seconds).
Top panels: comparison of the velocity plotted over the vertical for test T201. The x locations where the velocity where taken from 0.125 m in front and after the velocity cap and they are highlighted in the lower panel by red segments.
Lower panel: plot of the mismatch between horizontal velocity estimates computed as in eq. 5.3.

match between model results and the PIV measurements in the region preceding the velocity cap (see top left panel of figure 5.14) and and for distances larger than approximately 4 cm above the cap.
The velocity field at the top leading edge of the velocity cap is instead not correctly solved by the N-S/VOF solver. The red stain of the lower panel of figure 5.14 shows clearly that the interface between the recirculation zone and the outer layer is not predicted accurately by the model. The big value of the mismatch is due to the fact that in that region the numerical simulation estimated a negative velocity, while the PIV measured positive velocities. The numerical simulations are therefore predicting a wider extension of the recirculation zone at this location.
The prediction of the velocities at the location of the jet coming out from the opening of the cap at the trailing side is also showing some inaccuracy. This area is characterized by high turbulence development and the numerical results are slightly different from the PIV measurements. However for the present application it can be assumed that an accurate prediction of the flow downstream of the cap is of little interests when determining hydraulic loads on the structure. What is more relevant is the prediction of the flow field close to and inside the cap and even if the jet outside the structure is not perfectly captured by the model the velocity captured inside it is instead in good agreement.

In order to assess the accuracy of the model in capturing the development of the boundary layer separation, the error fields *mismatch* computed from the two previous time directories are also presented (313.4 and 313.5).

Figures 5.17 and 5.18 show that the a small mismatch in the prediction of the recirculation zone extension is present at the top leading edge of the velocity cap since the beginning of the flow separation. However the velocity in proximity of the structure is in good agreement with the PIV measurements. Figure 5.18 in particular shows the velocity field disagreement for the instant that corresponded to the peak of the inline force. The analysis of this picture is useful to understand that, even if the Reynolds-averaged flow patterns around the velocity cap are in general not perfectly captured, the values of the velocities near the cap are in overall good agreement with the PIV data. This explains how the comparison between experimental and numerical estimate of the inline force shows a reasonable agreement. Extending the analysis to instant 313.7 (see figure 5.19), it is visible how the flow on top of the cap is predicted in a considerably different way by the

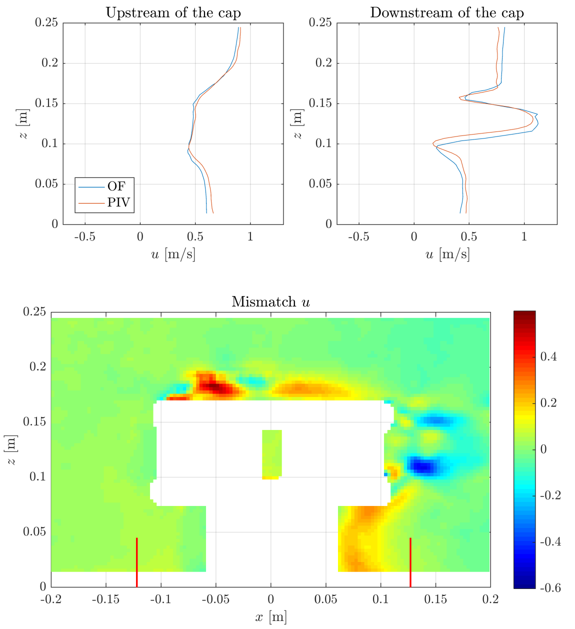

Figure 5.15: Comparison between the PIV and OpenFOAM velocity estimates for test T201 at time 313.6. The PIV velocity map used in the comparison has an offset of 2 frames (-0.066 seconds).
Top panels: comparison of the velocity plotted over the vertical. The x locations where the velocity where taken from 0.125 m in front and after the velocity cap and they are highlighted in the lower panel by red segments.
Lower panel: plot of the mismatch between horizontal velocity estimates computed as in eq. 5.3.

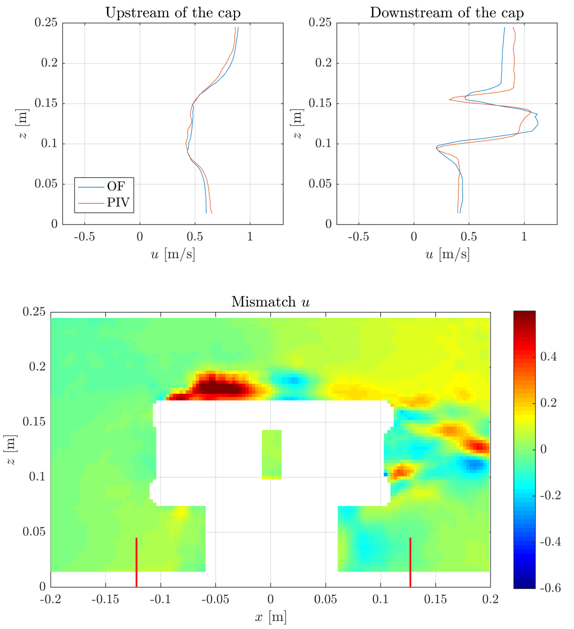

Figure 5.16: Comparison between the PIV and OpenFOAM velocity estimates for test T201 at time 313.6. The PIV velocity map used in the comparison is determined using the original synchronization and therefore it has zero offset.
Top panels: comparison of the velocity plotted over the vertical. The x locations where the velocity where taken from 0.125 m in front and after the velocity cap and they are highlighted in the lower panel by red segments.
Lower panel: plot of the mismatch between horizontal velocity estimates computed as in eq. 5.3.

model with respect to the PIV results. After the wave has passed, flow separation and wakes shedding from the structure are not captured correctly by the OpenFOAM model.

The velocity field prediction can explain the mismatch observed earlier between numerical results of the inline load and corrected experimental records. The plots of the inline force predicted by the model can be found in appendix E, which shows an accurate prediction of the front part of the force signal by the model. From the peak until the tail of the force signal the OpenFOAM estimates are generally lower than the corrected experimental records. This inaccuracy is foremost present when the peak of the wave has passed the cap.
From the point of view of the determination of the loads, this affects the distribution of the the viscous shear stress and of pressure on the cap patches. The former was observed to be accountable for only 2-3% of the total inline force and is therefore considered of lesser importance. The latter is instead determining the greatest part of the load. The incorrect pressure field distribution must have therefore caused the mismatch between the corrected experimental records and the numerical results.
In chapters 6 and 7, the experimental and the numerical estimates of the inline load are decomposed following the Morison equation model between inertia and drag components. The obtained differences between the experimental and numerical estimates help understanding the limitations of the OpenFOAM model with regards to the load prediction. This is described in chapter 8.

5.5. Summary

The results obtained with the N-S/VOF solver including a k-ωSST turbulent closure have been compared with the experimental measures presented in chapter 3. An important finding is that the set-up of the velocity cap during the physical model tests determined an experimental bias on the force measurements. The numerical

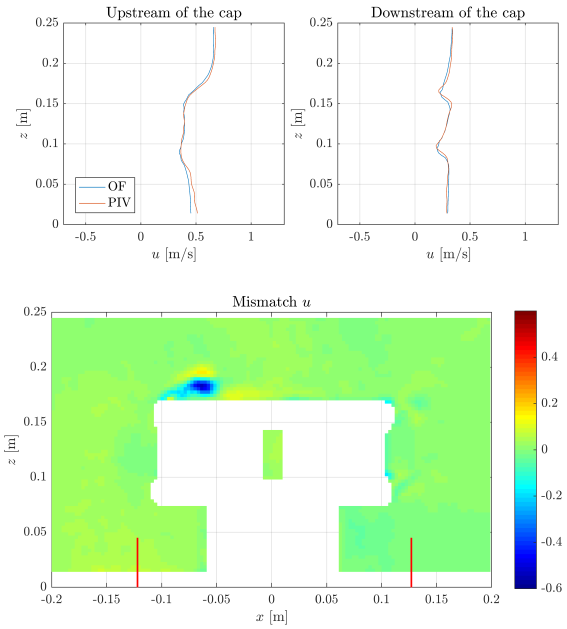

Figure 5.17: Comparison between the PIV and OpenFOAM velocity estimates for test T201 at instant 313.4. This frame corresponds to the beginning of the strong flow separation at the top leading edge of the velocity cap. The PIV velocity map used in the comparison has an offset of 1 frames (-0.033 seconds).

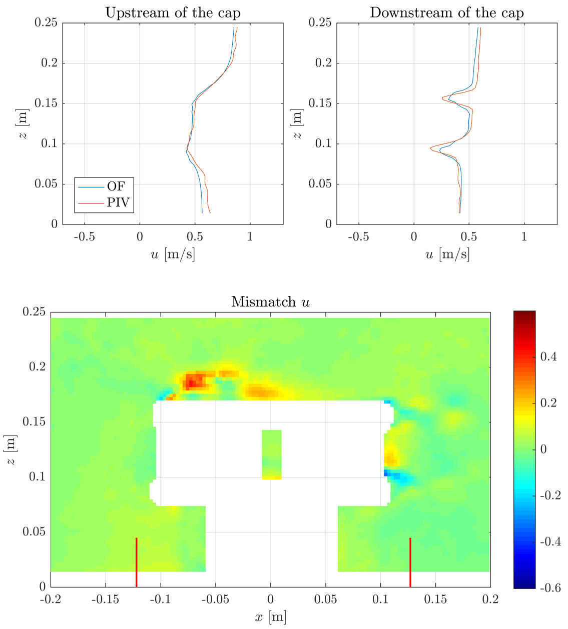

Figure 5.18: Comparison between the PIV and OpenFOAM velocity estimates for test T201 at instant 313.5. This frame corresponds to the moment when the inline load was at its peak. The PIV velocity map used in the comparison has an offset of 1 frames (-0.033 seconds).

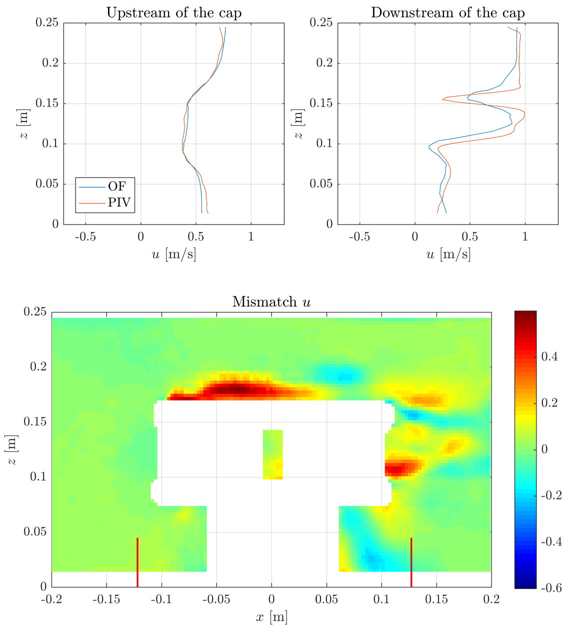

Figure 5.19: Comparison between the PIV and OpenFOAM velocity estimates for test T201 at instant 313.7. This frame show the development of of the flow and of the wakes 0.1 seconds after the crest of the wave has passed the center of the velocity cap. The PIV velocity map used in the comparison has an offset of 1 frames (-0.033 seconds).

model is used to estimate a pressure correction which has been applied to the raw experimental records in order to allow a comparison with the numerical output.

The inclusion of the turbulent closure is found to be necessary to come to a match between numerical results and corrected experimental records for the inline force. In the case of the vertical force, instead, the model results underestimate the corrected experimental records.

At the end of the chapter a comparison between the PIV measurements and the OpenFOAM estimate of the velocity field has been presented. This comparison has resulted in the detection of the regions where the model failes in predicting the velocity field. These regions are characterized by flow seperation and high turbulent development. The incorrect prediction regards the extension of the recirculation region and the wakes behind the cap.

In the next two chapters the force records obtained experimentally and numerically are fitted in order to define force coefficients. Eventually the comparison between the two estimates of the coefficients is presented in chapter 8.

6

Experimental characterization of the loads for solitary waves

In this chapter, the characterization of the inline and vertical forces acting on the cap as measured during the experiments is presented. In this perspective, the chapter is organized as follows.

- First of all, it is shown how an accurate estimate of the undisturbed velocity at the position of the cap is obtained.
- Once the velocity is known, the experimental force signal are fitted in order to estimate the force coefficients. The fitting equation used are the Morison equation in the case of the inline force, while for the vertical force both the original lift force equation and a modified vertical force equation are used.
  The use of a modified vertical force equation is shown to be necessary in order to capture the evolution of the vertical force. The new equation consists of three terms and take into account the velocity components along the horizontal and vertical axis and the vertical acceleration.
- At the end of the chapter the coefficients are plotted against the KC number and other dimensionless numbers used to characterize the flow.

During the numerical study it has been observed that the raw force signals analyzed in this chapter are affected by an experimental bias (see section 5.2.1). Nevertheless, this chapter focuses on those records. The relevance of the findings is then analyzed in detail in the discussion (chapter 8).

6.1. Undisturbed velocity

The equations used to characterize the forces in this chapter link the force to the undisturbed velocity ($\overrightarrow{u_0} = (U_0, W_0)$) and its derivatives by using specific coefficients. These coefficients are not known a priori for the geometry of the velocity cap and getting a first estimate of those is the aim of this chapter.
In the definition of the force equations, the undisturbed velocity is the velocity that would be measured in absence of the structure (in this case the velocity cap) but the experiments did not include any test with this set-up. Therefore, in order to know the force coefficients, in first place, a good estimate of this velocity was sought.

The undisturbed velocity estimation has been focused at first on the horizontal component only (U_0) and has followed five different approaches, which are:

- Extraction from the PIV measurements.
- Continuity equation integration from the surface elevation.
- Analytic equation for the horizontal velocity derived from the solitary wave theory (Svendsen and Jonsson, 1980).

- Results from the OCW3D model.
- Results from the OpenFOAM model.

Eventually, the OpenFOAM reconstruction of the velocity is used to derive the force coefficients. The results from OCW3D, which are in good agreement with the OpenFOAM results, are only used to determine the dimensionless numbers that characterize the flow for the reason described in section 6.1.3. A brief presentation of how the velocity estimate is obtained according to the first four approaches is included in appendix C.

6.1.1. Velocity and acceleration from the N-S/VOF solver

The velocity signal estimated by the N-S/VOF solver and probed during the RAS simulations is used as an estimate of the undisturbed velocity to apply the weighted least squares method and to estimate the force coefficients. The probed signal is a vector that includes the components along the x, y and z axis. Therefore, even if the results described here regard the horizontal component (U_0), exactly the same procedure is used for the vertical component (W_0).

The location selected for the extraction of the OpenFOAM velocity time series is 0.115 m above the bottom level and 0.05 m from the side of the wall. The height of this position corresponds approximately to the height of the center of mass (0.116 m). It is useful to remember that the flume was one meter wide, the velocity cap was at the center and its bigger diameter was 0.22 m. The distance between the probed location and the closest point of the structure is therefore 0.34 m (see figure 6.1). This specific location allows to have directly an estimate of the horizontal velocity synchronized with the flow and forces computations but unaffected by the presence of the cap due to its distance from the center-line.

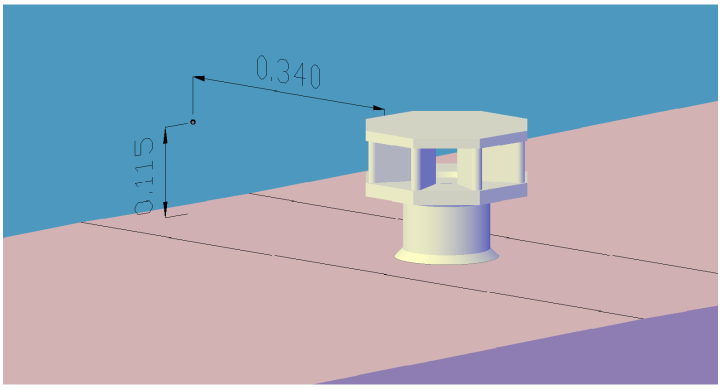

Figure 6.1: Location of the probed velocity. The dimensions are in meters.

The derivative of such a signal gives the acceleration of the water. The first attempts to find an estimate of the velocity gradient from the OpenFOAM probed output, however, resulted in a signal that was at times very coarsened by the noise (high frequency wiggles, see figure 6.2). In order to improve the estimate, the following algorithm is used to obtain the acceleration:

1. The velocity signal is interpolated to an equally-spaced time axis
2. The gradient of the obtained signal is computed
3. The noise of the raw gradient is filtered by means of a moving-average filter with window size seven[1]

A final remark on the OpenFOAM reconstruction of the velocity is that the validation of the OpenFOAM model has not been possible for the test cases involving wave breaking as presented in chapter 5. Therefore the velocity estimate computed for those cases is not considered accurate enough for the coefficients computation. Therefore the dimensionless parameter and the force coefficient estimated for the breaking cases are reported in red in the tables and are not included in the final plots of the coefficients presented in the next sections.

---

[1] The filter is applied in MATLAB by means of the built-in function *filter*.

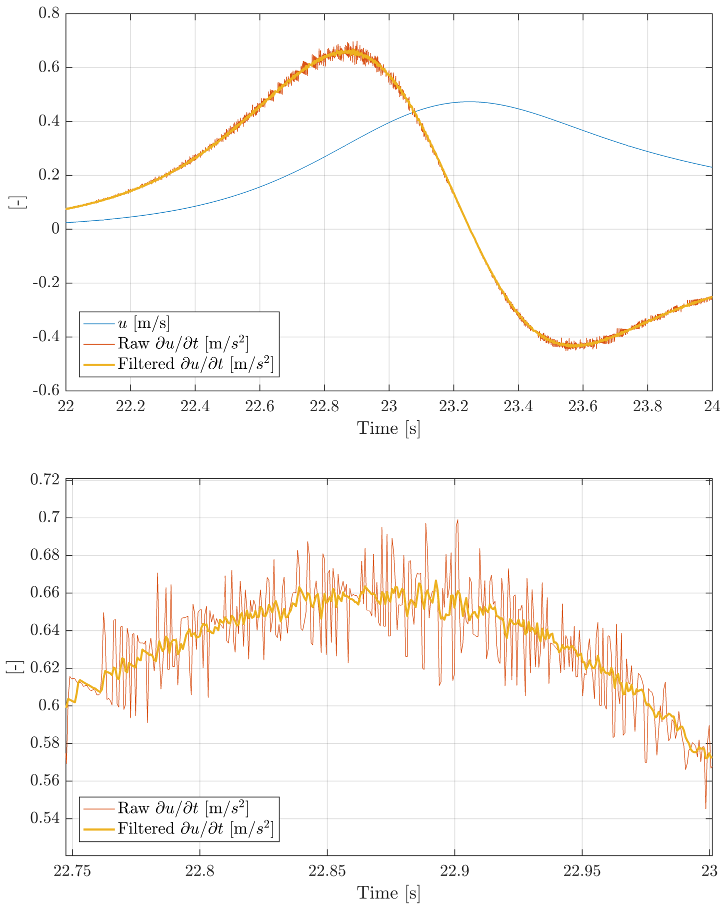

Figure 6.2: Example of the estimate of the velocity and acceleration obtained from the OpenFOAM computations. In the lower panel, a zoomed detail of the upper plot shows more closely the high frequency wiggles observed.

6.1.2. Differences between OCW3D and OpenFOAM estimate of the undisturbed velocity

Both models described in this thesis can give an estimate of the undisturbed horizontal component of the velocity.

Even if the equations solved are different between the two, for all non-breaking cases, a good agreement in the velocity estimation is observed. The reason for this is that for non-breaking waves the flow remains irrotational and therefore the Laplace equation solved by the potential flow solver is a good approximation of the complete N-S equations. The OpenFAOM estimate shows an overestimation of the peak velocity of 2-3 % with respect to the OCW3D results. Figure 6.3 shows an example of the comparison for test T201. The substantial difference between the estimates is that the set-up used in OCW3D is 2-dimensional and it does not include the presence of the cap while the OpenFOAM one is 3-dimensional and it includes the presence of the cap.

The overestimation of N-S/VOF solver is thought to be mainly due to the fact that the presence of the cap in the flume was inducing flow contraction and therefore an acceleration of the water at the sides of the cap. The forces recorded with that set-up were therefore perturbed by the flow contraction. In order to take this into account, the coefficients estimation is based on a velocity reconstruction that is also accounting for this small contraction of the flow (i.e. the one from OpenFOAM).

6.1.3. Characterization of the flow field

In order to classify the flow (always unsteady), two dimensionless numbers are used as introduced in section 2.1: the Keulegan-Carpenter number (KC) and the frequency number (β). The computation of the latter parameter is obtained by computing the ratio of the Reynolds number (Re) and the KC number.

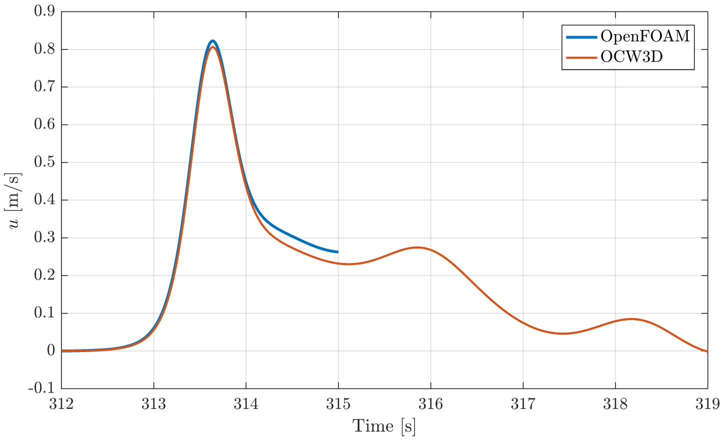

Figure 6.3: Comparison between the OCW3D horizontal velocity estimate and the solution computed by the N-S/VOF solver. Data relative to test case T201

The Reynolds number (Re) is defined as:

$$Re = \frac{DU_{0,max}}{\nu} \tag{6.1}$$

The numerator is the product of the diameter of the structure and a velocity that, in this case, is taken as the maximum of the horizontal velocity obtained from OCW3D when the waves are passing. The denominator represents the kinematic viscosity (ν).

The Keulegan-Carpenter number is described in equation 2.6. That formula can be rewritten as:

$$KC = \frac{r\pi}{D} \tag{6.2}$$

From a computational point of view, r is calculated integrating the velocity U_0, obtained with the model OceanWave3D, over the time in which the velocity is bigger than 0.001 m/s. Looking at the integration of the velocity signal (see figure 6.4) one can see that the model predicts an initial part of the test with a slow negative displacement of the particles (towards the left if the wave is propagating towards the right). When the wave arrives, the direction of the movement reverses suddenly and the particles are quickly brought back to their original position. Integrating the velocity signal after this flow reversal gives the total displacement of a particle in one direction. In Figure 6.4, the top panel shows the velocity computed for test T201. The lower panel presents the integral of the same signal (computed by means of cumulated trapezoidal integration). In this panel, it is possible to see the slow drift of the particles for approximately 2 meters at the beginning of the simulation and the sudden movement in the positive direction when the velocity in the top panel is positive. The red lines highlight the period of time between the arrival of the wave and the following maximum in the horizontal displacement. This period is then used as t in the expression $r = \int_t U_0 dt'$.

Using the N-S/VOF solution for the undisturbed velocity discussed earlier in this chapter is not possible because the duration of the simulation in the cases of a solitary wave was too short to apply the procedure just described. The velocity signal, in fact, needs to be known for the whole time interval in which it remains higher than 0.001 m/s. Simulating a longer time interval in OpenFOAM for every test cases would have increased considerably the computational time. Moreover, the OCW3D estimate of the velocity does not differs in a significant way from the N-S/VOF solver estimate in the simulated interval (see figure 6.3).

After Re and KC are defined, the last relevant parameter β can be defined as the ratio between the two. Table 6.1 shows the values of the dimensionless numbers described above for the several test cases.

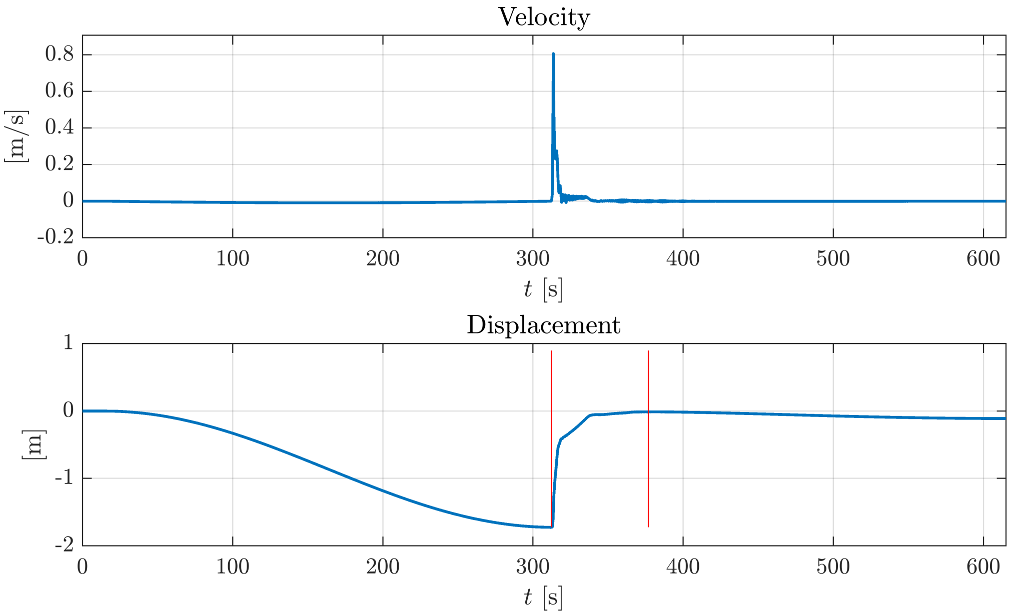

Figure 6.4: Example of the computation of the displacement r. Data relative to test case T201.

Table 6.1: Dimensionless numbers relative to the 9 test cases involving solitary waves.

Test case	Re $\times 10^5$	KC	Re/KC $\times 10^3$
T101	1.89	27.24	6.94
T102	2.08	36.04	5.77
T103	2.29	43.00	5.33
T201	1.77	24.47	7.25
T202	2.33	32.21	7.22
T203	2.36	36.68	6.44
T301	1.69	22.61	7.46
T302	2.30	29.83	7.72
T303	2.49	34.34	7.26

6.2. Force fits

The aim of this chapter is to determine the force coefficients of Morison and vertical force equations 2.9 and 2.11 based on the raw experimental records obtained during the experiments. In engineering practice, those coefficients are known for a number of geometries and are heavily used in desk studies that often come with a design.

The coefficients are derived fitting the force signal in a time window of 1.2 seconds centered at the peak of the considered force (the positive inline force peak and the negative vertical force peak). The algorithm used was implemented in MATLAB and it is based on the weighted least squares method described in chapter 2. The implementation of the metrod is described in appendix D.

It has to be noted that the set-up used during the experimental campaign introduced an additional pressure component due to the penetration of water under the base plate and presence of the base plate itself. These two factors are obviously not observed in the case of a real installation, where the foundations extend below the bed level and do not work as a gravity base. The presence of this bias was observable only when setting up the numerical model, which was prepared in a way that allows to include or exclude these components. In chapter 7, the force coefficients are computed making use of the OpenFOAM estimates.

6.2.1. Inline force fits

In the present application, the Morison equation offers a relatively good fit to the measured force records both with regards to the peak of the force and general shape of the signal as shown in figure 6.5. In the figure, the decomposition between inertia and drag component of the force obtained with the force coefficients that give the best fit is also shown. In all test cases the peak of the force is approximately for one half due to inertia and for the other half to the drag.

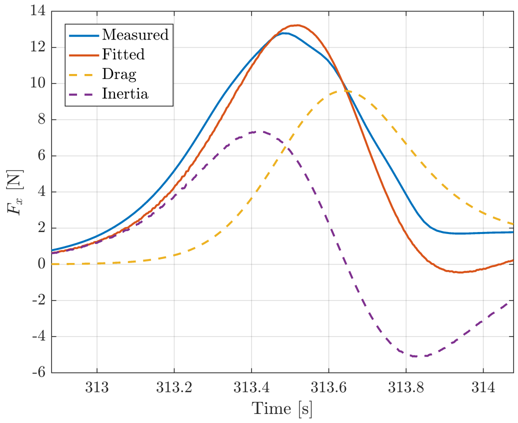

Figure 6.5: Force fit obtained for the inline force recorded during test T201. The decomposition between inertia and drag is also shown.

Even if some discrepancies are visible in the plots no attempts to fit the inline force signal with a different equation are done. The main reasons are that the Morison equation is well known and broadly used in engineering applications and, besides, that the overall fit obtained with this equation is already satisfying.

6.2.2. Vertical force fits

In the case of the vertical force, it is observed that the fits obtained with the simple lift force equation show a clear mismatch both with regards to the general shape of the signal and the peak amplitude.

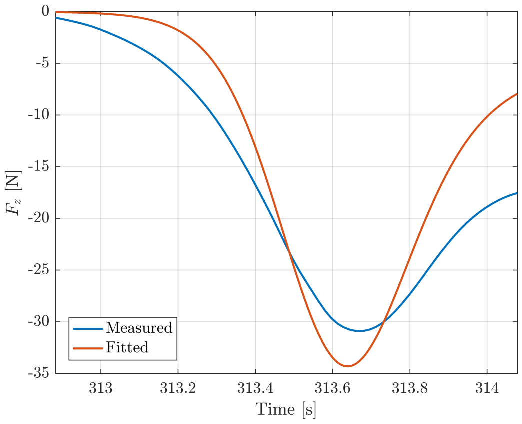

Figure 6.6: Force fit obtained for vertical force recorded during test T201.

The dependency of the said force is therefore studied with regards to other components as well. It is clear that the simple formulation of the lift force equation, defined for steady and one-dimensional flows, is unable to characterize accurately the evolution of the vertical force in this application. In order to suggest a formulation that could capture better the evolution of the vertical force in time new terms are added to the original lift force equation.

It is observed that the velocity field is unsteady and 2-dimensional. In In the physical model tests, the ratio

H/h reached values up to 1.1, meaning that the surface elevation in some tests became more than twice as high as in the case of calm surface. This suggested that the vertical velocity and the vertical acceleration should also be taken into account.
The improvement in the quality of the fits obtained with the new vertical force equation bolstered the validity of the observation just made. In this way the original horizontal drag component is coupled with a vertical drag component and a vertical inertia component.

The resulting equation expresses the evolution of the vertical force as:

$$F_{vertical} = \frac{1}{2}\rho C_{Lx} A U_0 \sqrt{U_0^2 + W_0^2} + \frac{1}{2}\rho C_{Lz} A W_0 \sqrt{U_0^2 + W_0^2} + C_{Mz}\rho V \frac{\partial W_0}{\partial t} \tag{6.3}$$

Where C_{Lx} is the horizontal drag coefficient, C_{Lz} is the vertical drag coefficient and C_{Mz} is the vertical inertia coefficient.

The formulation of the drag components needs a specific description in this case. Given the 2-dimensional feature of the flow, the undisturbed velocity is written in vectorial form as $\overrightarrow{u_0} = (U_0, W_0)$. In the case of such a velocity field, if it holds that the force on an object is $F \propto u_0 \left\|\overrightarrow{u_0}\right\|$ then the decomposition between x and z component of the force can be written as:

$$\begin{pmatrix} F_x \\ F_z \end{pmatrix} \propto \left\|\overrightarrow{u_0}\right\| \begin{pmatrix} U_0 \\ W_0 \end{pmatrix} \tag{6.4}$$

Focusing on the vertical force and writing explicitly the norm of the velocity vector, it holds that:

$$F_z \propto W_0 \sqrt{U_0^2 + W_0^2} \tag{6.5}$$

For some test cases all three force components play a role in determining the total load, as shown by the fit obtained with the new vertical force equation of figure 6.7. The component of the drag due to the horizontal velocity is clearly the most important term. However, for all test cases the contribution of the vertical acceleration is needed to come to estimate the right shape and peak amplitude of the force signal.

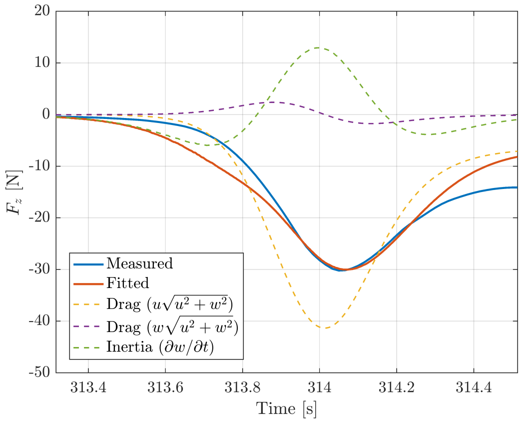

Figure 6.7: New force fit obtained with equation 6.3. The decomposition of the total load between the 3 components is also shown. The summation of the dashed lines gives the total data relative to test T101.

With regards to vertical drag, its importance varies considerably from test to test. Figure 6.7 shows the case of test T101 for which the vertical drag is contributing in a significant way to the final shape of the fit. The relevance of including this term is instead very low for test T301 (see figure 6.8) because its amplitude remains close to zero. Including this term is shown to be relevant also when characterizing the vertical forces obtained by means of the numerical model as discussed in chapter 7.

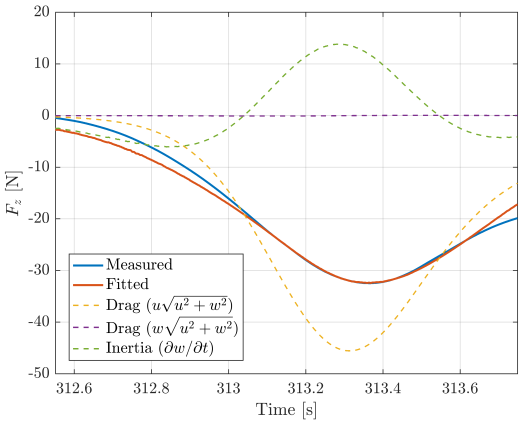

Figure 6.8: New force fit obtained with equation 6.3. The decomposition of the total load between the 3 components is also shown. Data relative to test T301.

6.3. Coefficients results

This section describes the results of the fitting procedure presented above. The coefficients are presented both in tabular form and by means of graphs that represent the relationship between the force coefficients and the dimensionless parameters (Re, KC and β).
In order to study the match of the fit to the measurements, a shape error is computed as the standard deviation of the difference between the experimental record and the fitted signal normalized by the peak of the relative force (see equation 6.6).

$$\epsilon = \frac{std(F_{exp} - F_{fitted})}{|F_{peak,exp}|} \tag{6.6}$$

6.3.1. Inline force coefficients

The coefficients presented in table 6.2 are estimated by fitting the inline force signal by means of the Morison equation (see equation 2.9). The analysis of the fit shown in the previous section as well as the quantification of the error on the estimation of the peak force shows that the original formulation of the Morison equation is suitable to fit the force signal in the case of solitary waves.

Table 6.2: Morison coefficients computed from the raw experimental force records. The errors (ϵ) are expressed as a percentage of the computed signal and are estimated as in equation 6.6.

	Inline force		
Test case	C_D	C_M	$\epsilon(F_x)$ [%]
T101	1.16	0.71	6.02
T102	1.04	0.78	6.90
T103	1.75	0.13	27.50
T201	1.24	0.88	6.85
T202	1.07	0.86	7.86
T203	0.89	0.88	10.67
T301	1.35	0.85	4.96
T302	1.19	0.81	5.89
T303	1.06	0.89	7.54

The first plots of figures 6.9 regard the coefficients of the Morison equation for the inline force. The inertia coefficient remains relatively constant, while the drag shows a slight negative trend when plotted against KC. The parameter β is between 2000 and 7000 approximately.

Even if the number of the data points on which to rely on is limited, the behaviour of the drag and inertia coefficients is in analogy with what found in Sarpkaya (2010) for the case of a single cylinder for similar values of KC and β.
What is considerably different is the magnitude of the coefficients. The inertia coefficient found for the geometry of the velocity cap is between 0.80 and 0.90 with only one exception around 0.70, while values for a single cylinder are close to the theoretical value of 2. With regards to the drag, the coefficient predicted here is between 1.05 and 1.35 while for similar values of β ($\beta = 5260$) Sarpkaya (2010) found values between 0.60 and 0.80.

The differences can probably be explained considering how the frontal area and the volume of the cap are computed in this study. As described in appendix A, the visible area in the front view is used in the Morison equation. Therefore the area of the support columns on the trailing side of the open part of the cap are not taken into account in the computation of the area. The flow however might feel this back part of the cap as well. Therefore the low estimate of the frontal area is balanced by a higher drag coefficient.

In the case of the volume instead, the estimate of the top part of the velocity cap is obtained without subtracting the internal hollow part. The used estimate is therefore overestimating the actual volume of the cap and as a consequence the inertia coefficient decreases.

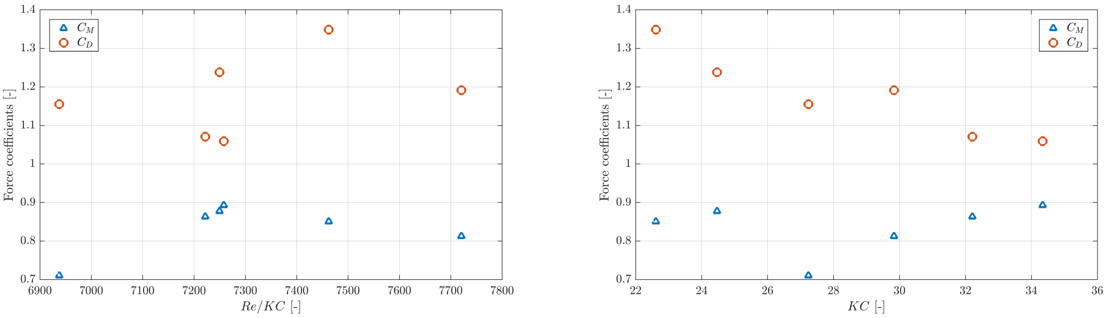

Figure 6.9: Force coefficients for the Morison equation plotted over representative parameters for the flow conditions. In these and in the next plots only the results from the tests that did not involve breaking are included.

6.3.2. Vertical force coefficients

In the case of the vertical force, the raw experimental signal was fitted in two different ways. First with the original lift force equation (eq. 2.11) and secondly with the modified formula 6.3. Table 6.3 reports the coefficients estimated in both ways but given the better quality of the fit obtained with the new vertical force equation, the graphs only focus on the three coefficients of equation 6.3.

Table 6.3: Vertical force coefficients computed from the raw experimental force records. The errors (ϵ) are expressed as a percentage of the computed signal and are estimated as in equation 6.6.

	Original eq.		New vertical force eq.			
Test case	C_L	$\epsilon(F_z)(1)$ [%]	C_Lx	C_Lz	C_Mz	$\epsilon(F_z)(2)$ [%]
T101	-3.76	14.54	-4.70	2.47	-2.79	9.07
T102	-3.40	11.49	-4.46	-4.24	-3.50	19.35
T103	-4.43	20.05	-4.92	1.90	-2.11	12.73
T201	-4.42	11.66	-5.61	-0.55	-5.15	3.95
T202	-3.47	11.72	-4.36	-1.12	-3.53	8.48
T203	-3.39	12.14	-3.89	-7.04	-3.22	8.84
T301	-5.10	11.52	-6.49	-0.17	-8.47	3.84
T302	-3.66	13.70	-4.76	0.57	-6.34	7.78
T303	-3.22	11.32	-4.09	-3.26	-5.16	8.98

The three vertical force coefficients do not show a particular trend when plotted over Re/KC (graph not included) while the relation with KC only and with the value H/h (already presented in table 3.3) are more explicative (see figures 6.10 and 6.11). All three coefficients show a considerable variation in the range of KC analyzed . The horizontal drag shows a positive trend when plotted against the KC number and against H/h. The two other coefficients instead do not show a clear dependency of these dimensionless numbers.

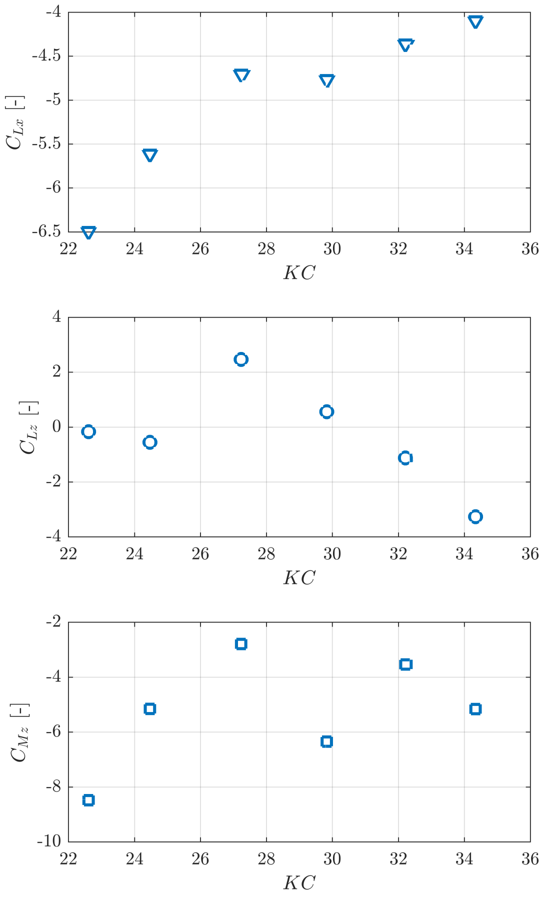

Figure 6.10: Vertical force coefficients plotted over the KC number.

Given the importance of the vertical inertia coefficient, its dependency has been studied with respect to several parameters. The strongest relation found is shown in figure 6.12, where the coefficient is plotted over the ratio $W_{0,max}/U_{0,max}$. This parameter is found in literature to define the level of eccentricity of the orbital motion of the water particle (Sumer and Fredsøe, 2006). When the orbital motion is particularly flat (low $W_{0,max}/U_{0,max}$) the vertical inertia coefficient has a high negative value, while, for more round orbital motions (high $W_{0,max}/U_{0,max}$), it becomes smaller in absolute value .

6.4. Summary

The aim of this chapter was to give an analysis of the forces and of the force coefficients based on the raw experimental records. It was observed that the Morison equation is able to model the inline force signal shape and amplitude in the case of solitary waves if a good estimate of the undisturbed velocity is known. In the case of the lift force, the original formula (eq. 2.10) is not sufficient to characterize the vertical force when the vertical component of the velocity field is not negligible and for unsteady flows, as in the case of large solitary waves. The new equation (see eq. 6.3) modifies slightly the horizontal drag component and takes into account the contributions of the vertical drag and of the vertical inertia. The better fits obtained with this new formula suggest indeed that these extra terms cannot be neglected.

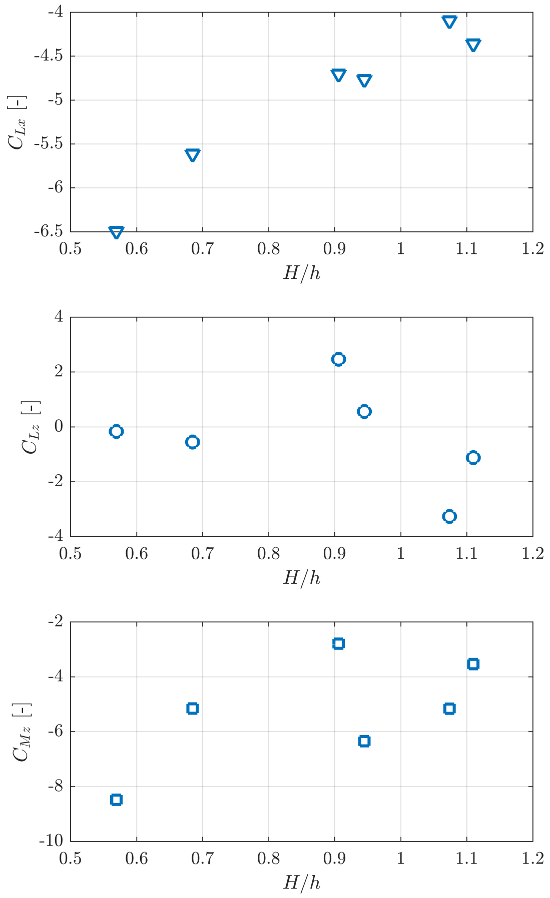

Figure 6.11: Vertical force coefficients plotted over the ratio H/h.

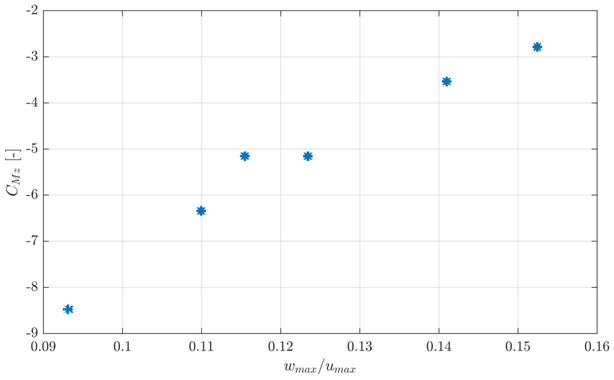

Figure 6.12: Vertical inertia coefficients (C_{Mz}) plotted over the ratio $W_{0,max}/U_{0,max}$.

The analysis of the inline force fits showed that the drag and inertia component are equally important in determining the value of the peak force. The computed coefficients for the inline force show approximately the same dependency of the KC number as found in literature but a different magnitude. This difference can be due to the way the frontal area and the total volume of the structure were computed.

In the case of the vertical force fits, it was observed that the three terms included in the new vertical force equation are not contributing in equal way and that their relative importance changes among the test cases. The component due to the horizontal drag is shown to be the most important for determining the amplitude of the peak of the vertical load. The relative value of the coefficient (C_{Lx}) is always negative and it increases with increasing KC number. The contribution of the other terms is however very important to determine the right value and evolution of the vertical force. All vertical force coefficients show a considerable variation. The correlation with KC and H/h is however not clear in the case of the two other coefficients (C_{Lz}, C_{Mz}). In particular, the change of the vertical inertia coefficient (C_{Mz}) seems to be related to the eccentricity of the orbital motion estimated by computing the ratio $W_{0,max}/U_{0,max}$.

7

Numerical characterization of the loads

In this chapter the numerical model validated in chapter 5 is used to define force and moment coefficients for the geometry of the velocity cap. Here the analysis focuses on the set-up of the cap that excludes the presence of a base plate and therefore of any pressure corrections. In particular, the plots of the vertical force in this chapter correspond to the lines that are labelled "OF without plate" in chapter 5. The model used is the last presented in the chapter 5, which includes the k-ωSST turbulent closure and the use of wall functions.

The database of the numerical investigation is expanded and does not only include the original test cases simulated during the experimental campaign. The reason is to gain more information for cases with a KC number lower than in the original soliton tests. The test cases analyzed are therefore:

- nine original test cases on solitary waves used in the previous chapter for the validation of the model
- seven new cases on solitary waves
- five new test cases on regular waves

The coefficients found are then plotted against the Keulegan-Carpenter number, since this parameter has already been proven useful in literature to compare different configurations of single or groups of cylinders in oscillating flows.

The test cases that involved wave breaking are also modelled in OpenFOAM. However, the mismatch between inline force signal computed and measured and a preliminary assessment of the dynamics of the wave breaking predicted by the model show that the wave breaking is not predicted in an accurate way. This leads to the decision of not including the force coefficients relative to those tests cases (T102, T103, T203) in the final plots of the results. The data regarding those tests are reported in red elsewhere.

7.1. Additional test cases

The nine test cases involving solitary waves allow drawing conclusions on the values of the force coefficients for a range of KC numbers between 20 and 40 approximately. In order to expand this range and to compare the results with different types of waves, additional tests cases are prepared. The seven new test cases on solitary waves are prepared using the same bathymetry as the experiments while the five regular wave cases are modelled using a flat bed.

7.1.1. Additional solitary wave tests

The boundary conditions for the solitary wave cases are once again provided by the solver OCW3D. The steering files for these computations are generated ad hoc making use of the same script by Dr. ir. Bas Hofland

Table 7.1: Description of the 7 additional solitary wave cases.

Test name (Solitons)	Bed type	h [m]	H_0/h_0	H/h	Breaking	Period [s]
T201_5	orig. bathymetry	0.27	0.3	0.51	no	10.0
T301_4	orig. bathymetry	0.33	0.2	0.30	no	10.0
T301_5	orig. bathymetry	0.33	0.3	0.44	no	10.0
T301_6	orig. bathymetry	0.33	0.35	0.73	no	10.0
T401_1	orig. bathymetry	0.38	0.03	0.04	no	10.0
T401_2	orig. bathymetry	0.38	0.05	0.07	no	10.0
T401_3	orig. bathymetry	0.38	0.10	0.14	no	10.0

presented in chapter 3. In order to obtain values of KC number lower than 20, the ratios H_0/h_0 used to generated these new steering files are 0.03, 0.05, 0.1, 0.2, 0.3 and 0.35 (in the original cases they were 0.4, 0.6 and 0.78). Table 7.1 presents the features of the additional solitary wave cases.

The obtained waves are of smaller amplitude and longer wavelength when compared to the original test cases. In the case of the T401_1, T401_1 and T401_3, the outputs of force and moment signals by the model show wiggles as can be seen in figure 7.1. The reason of these behaviour is still unknown but fitting the signal with the relative equation could in any case provide an estimate of the coefficients and the fit are of good quality.

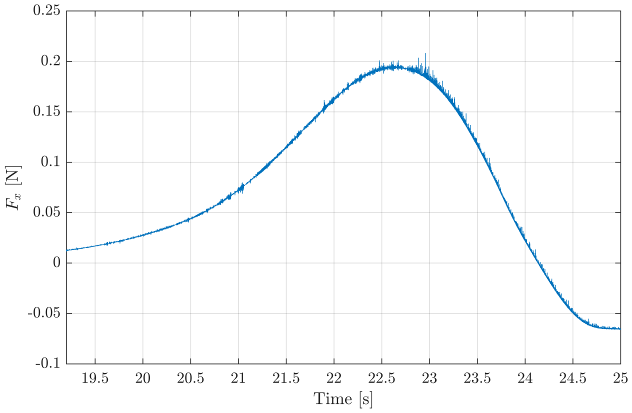

Figure 7.1: Inline force estimate relative to test case T401_1. The signal is affected by high frequency and low intensity oscillations.

7.1.2. Regular waves

The model used for the regular waves differs from the one used for solitary waves with regards to the inlet and outlet boundary conditions. Instead of applying the relaxation zone at the inlet, waves2Foam also offers a range of wave theories that can be used to generate a boundary field for the variables used in the computations. In the present application the regular waves are modelled by means of the stream function wave theory.

The estimates of the target KC numbers for various values of the period (T) and wave height (H) have been computed by means of the linear wave theory.
Even if the stream function wave theory is based on a nonlinear formulation, the obtained results (reported in table 7.2) differ only slightly from the target computations. Table 7.2 gives an overview of the characteristic parameters of the regular wave cases.

The duration of each simulation is adjusted in order to include at least three full wave periods in the simulation. The stream function used generated waves with an increasing level of asymmetry for growing KC as can be seen from the comparison between figure 7.2 and figure 7.3.
With regards to the phasing between loads and surface elevation, the peak of the inline force occurs approx-

Table 7.2: Description of the 5 additional regular wave cases.

Test name (Regular waves)	Bed type	h [m]	T [s]	H [m]	Duration of the simulation	KC
R1	flat	0.4	1.27	0.06	8.0	0.60
R2	flat	0.4	1.27	0.10	8.0	0.97
R3	flat	0.4	1.60	0.10	8.0	1.41
R4	flat	0.4	2.07	0.10	12.0	2.09
R5	flat	0.4	2.47	0.12	15.0	3.33

imately when the wave profile is at the still water level and the peak of the uplift occurs approximately at the wave through. The loads follow therefore the same phasing found in Mogridge and Jamieson (1978) for the case of the sealed cylinder. The phasing between uplift and inline force shows therefore that for the intake cap studied in this thesis the analogy is bigger with a closed cylinder sealed to the bottom than to the very open structure studied experimentally by Mogridge and Jamieson (1978).

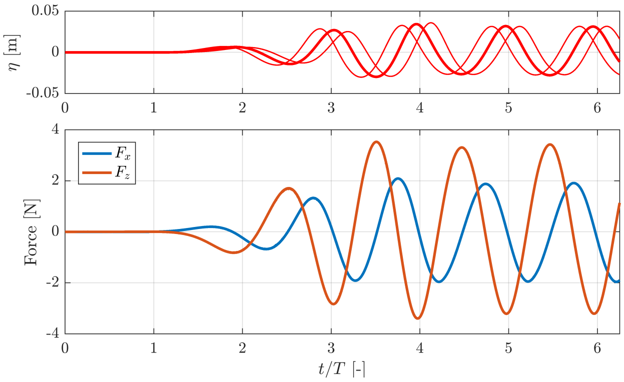

Figure 7.2: Water surface elevation, inline and vertical force computed by the model for test case R1. In the top panel the surface elevation probed at the location of the 5^{th}, 6^{th} and 7^{th} wave gauge is shown.

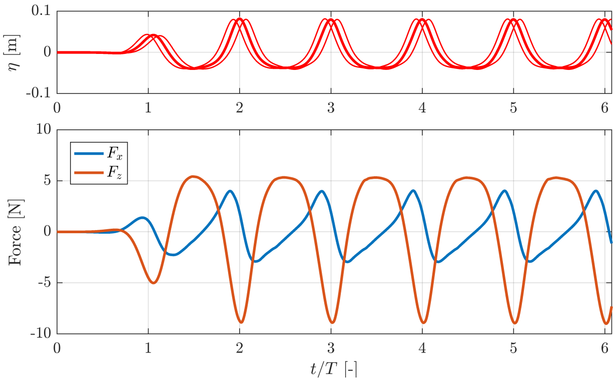

Figure 7.3: Water surface elevation, inline and vertical force computed by the model for test case R5. As in the previous figure, the surface elevation probed at the location of the 5^{th}, 6^{th} and 7^{th} wave gauge is shown in the top panel.

7.1.3. Characterization of the flow field

The characterization of the flow field is done as in chapter 6, by computing the main dimensionless parameters: KC, Re, and their ratio β. The KC number is computed as in eq. 2.2 for the regular test cases and as in eq. 2.6 for solitary wave cases.

The OCW3D estimate of the velocity is used to evaluate these parameters for all cases except for the regular wave cases. The reasons, as explained in chapter 6, are that the OpenFOAM velocity signal is too short for the procedure to be implemented and that OpenFOAM and OCW3D velocity reconstructions are in good agreement.

Table 7.3: Re, KC and β defined for the additional test cases. The KC number relative to the regular cases, already presented in table 7.2, are here repeated for completeness.

Test case	Re $\times 10^5$	KC	Re/KC $\times 10^3$
T201_5	1.46	11.64	12.58
T301_4	1.02	10.70	9.56
T301_5	1.41	12.28	11.45
T301_6	2.01	15.74	12.77
T401_1	0.19	4.93	3.77
T401_2	0.30	6.29	4.77
T401_3	0.56	8.53	6.58
R1	0.22	0.59	37.82
R2	0.36	0.94	38.07
R3	0.44	1.39	31.35
R4	0.51	2.07	24.71
R5	0.68	3.30	20.51

7.2. Force and moment fits

This section describes how the force and moment signals are fitted in order to find the force coefficients presented in section 7.3. The fits and the estimates of the total coefficients are found by applying the weighted least squares method described in chapter 2 and applied in chapter 6. The detailed description of the implementation of this method is included in appendix D.
The time window considered consists of the whole simulation in the case of the regular wave cases and of an interval of variable size in the case of the solitary waves. For the nine original test cases, the time window is the same used in the experimental characterization (1.2 seconds centered at the peak of the inline force). For the additional solitary wave test cases, the time window is increased in order to account for the longer wave length.

The force signal analyzed is the summation of the components acting on the top part of the velocity cap and the support cylinder. Any other force components defined earlier is dropped. In section 7.4 the analysis of the inline forces is extended by looking at the distribution of the loads between top part and support cylinder and by computing partial coefficients for the two different parts of the structure.

7.2.1. Inline force fits

The relative importance of drag and inertia can be determined by looking at the fits obtained. As described by Sumer and Fredsøe (2006), the smaller the KC number the more important the inertia component. Figure 7.4 and 7.5 show the fit obtained in the case of a regular wave test and of a soliton test. The test cases on regular waves show the lowest values of KC number and, in those cases, the bigger part of the load is due to the inertia. For the bigger KC number computed for solitary wave cases the peak of the force is generally due for one half to inertia and to the other half to drag.

7.2.2. Vertical force fits

The vertical force for the solitary waves always determines a pressure downwards on the velocity cap. This load is therefore working in favour of stability. The vertical load generated by regular waves instead has both a positive (upwards) and negative (downwards) peak.
With regards to the fitting equation to use the case of the vertical force both the original lift force equation and the new vertical force equation defined in chapter 6 are used.

In the case of the solitary wave simulations, it is observed that the original lift force equation (eq. 2.11) could

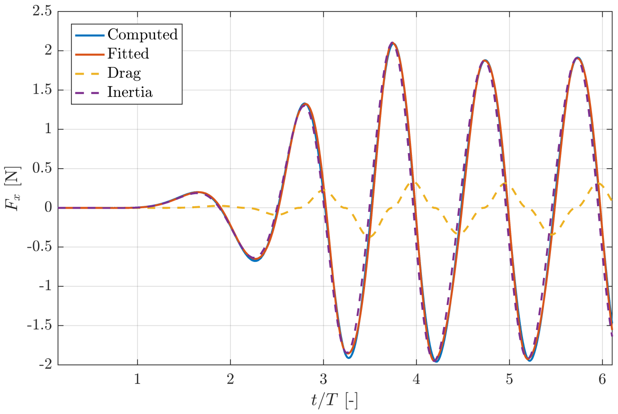

Figure 7.4: Fit of the inline force for test case R1. The biggest part of the load is determined by the inertia.

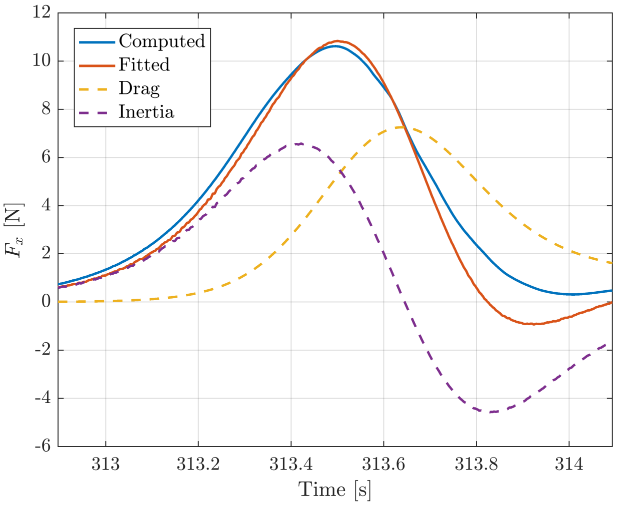

Figure 7.5: Fit of the inline force for test case T201. Here both drag and inertia are playing a role for determining the amplitude of the inline force peak.

give a better fit to the new force signal computed by the N-S/VOF solver than the raw experimental force record. Even if the peak and the general shape of the force signal remains not accurately predicted, the overall fit improves.

It can be assumed that some physical features of the vertical force change by neglecting the pressure components on the base plate. In a real installation, this part of the cap is not present and, therefore, the force signal computed by the model for the case that does not include the base plate is assumed to be more representative to conditions of the real world.

In all solitary wave cases however, the new vertical force equation (eq. 6.3) continues to give a better peak force fit. Figures 7.6 and 7.7 present the vertical force fits relative to test case T202 chosen since it is well representing the overall features observed for all non-breaking solitary waves force signals. The decomposition between the three components (horizontal drag, vertical drag and vertical inertia) showed that the biggest part of the load is attributable to the horizontal drag. The vertical inertia is counteracting the drag force and has a relative smaller importance, while the last component hardly influences the value of the peak force contributing in particular way to the force fit when the force is increasing and decreasing.

Also for the test cases involving regular waves the force is first fitted with the original lift force equation and then with the new vertical force equation. It is noted that the more the wave becomes asymmetrical with respect to the horizontal axis the poorer the peaks are predicted by the original lift force equation. By using this equation, the uplift peaks are underestimated and the downwards peak overestimated. The highest level of asymmetry is observed for test case R5. Figures 7.8 and 7.9 show the fits to the relative force signal obtained

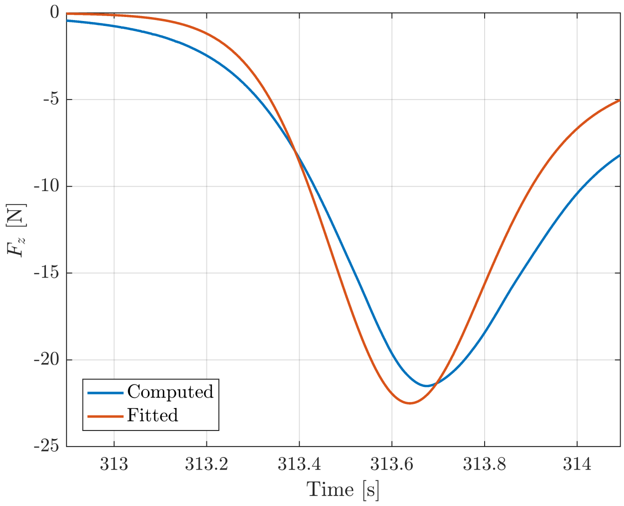

Figure 7.6: Fit of the vertical force obtained with the original lift force equation 2.11 for test case T201.

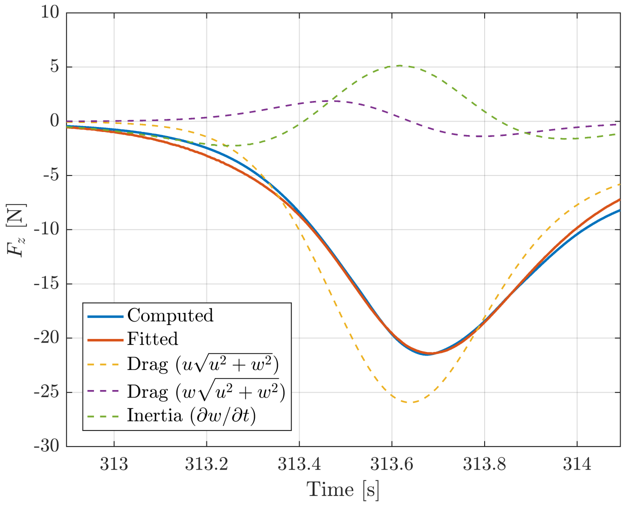

Figure 7.7: Fit of the vertical force obtained with the modified vertical force equation 6.3 for test case T201. The decomposition between the three components that build up the total force are also shown in dashed lines.

with the two equations.

The fits obtained with the new vertical force equation instead predict much better both the positive and the negative force peaks (see figure 7.9) even if the overall shape of the force signal is not in perfect agreement.

Focusing the attention on figure 7.9 it can be observed that horizontal drag and vertical inertia play the most important role in defining the peaks of the fitted signals.

7.2.3. Centroidal moment fits

The first estimates of the moment signal are obtained by means of the CFD model. The selected center of rotation is the center of mass of the velocity cap. The convention of the signs is that the turning moment is positive when clockwise.

The analysis of the centroidal moment offers the advantage of determining that component of the moment due to specific geometrical properties of the object and not due to the forces acting on the cap. In order to show the amplitude of the centroidal moment, this is compared with the linear moment (M_l) around the base

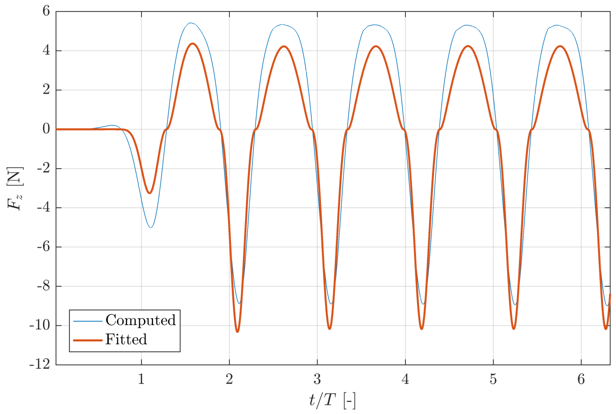

Figure 7.8: Fit of the vertical force obtained with the original lift force equation for test case R5.

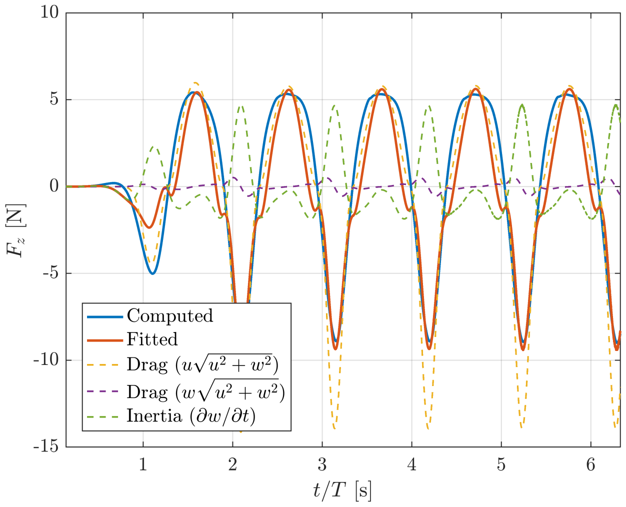

Figure 7.9: Fit of the vertical force obtained with the modified vertical force equation for test case R5. The four force components estimated are also shown.

of cap computed as in equation 2.12. Multiplying the inline force times the moment arm (the distance of the center of mass from the bottom, 0.116 m) the linear moment around the projection of the center of mass at the level of the bottom could be obtained.

In the case of the solitary wave tests, it is found that the centroidal moment computed is always between 10 and 20 % percent as big as the linear moment. This means that neglecting the centroidal moment in a design would cause an underestimation of the moment around the base of approximately 10 to 20 % (see figure 7.10).

In the case of the regular wave tests the centroidal moment is in counterphase with the moment measured at the base. Therefore the contribution of the centroidal moment reduces the total moment acting at the base (see figure 7.11).

The shift of phase between the cetroidal moment and the moment at the base M_O is observed to be decreasing with KC. From approximately 180° in the case of the regular waves to approximately 0° for the high KC solitary wave tests.
Comparing figure 7.10 and 7.11, it is observed that the evolution of the centroidal moment signal shows a clear difference in the case of solitary waves and regular waves. In the former case, the signal often shows two positive peaks while in the cases of regular waves one peak per wave period is observed.

As far as the fitting procedure is concerned, it is clear that the nature of the centroidal moment appears more complex than a simple dependency of the inline velocity and the geometry as suggested by the the moment

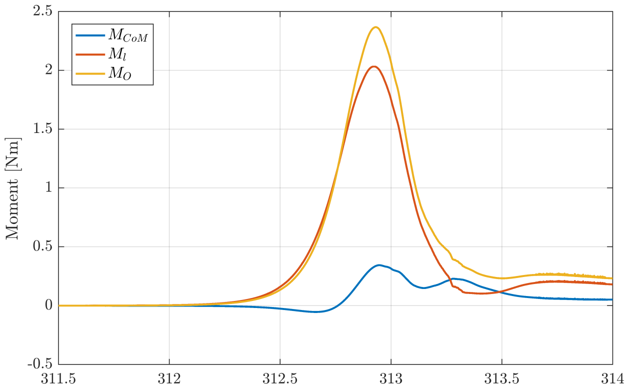

Figure 7.10: Comparison between the overturning moment for test T202 computed by the N-S/VOF solver around the center of mass (M_{CoM}), around point O at the base of the structure (see drawing 2.3, M_O) and as computed with the equation 2.12 ($M_{f,O}$).

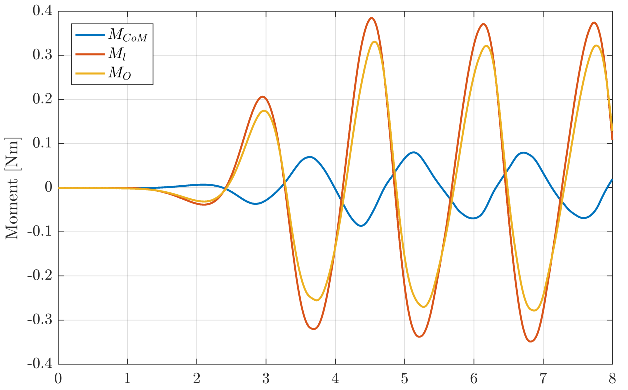

Figure 7.11: Comparison between the moment for test R3 computed by the N-S/VOF solver around the center of mass (M_{CoM}), around point O at the base of the structure (see drawing 2.3, M_O) and as computed with equation 2.12 ($M_{f,O}$).

equation 2.14 described in chapter 2.
In fact, the first attempts to fit the centroidal moment signal show that equation 2.14 fails in predicting the overall shape and peak of the computed signal, and the results are not presented in this report.

As in the case of the lift force equation, the dependency of the centroidal moment is studied also with regards to other component. What is generating the greatest part of the moment around the centroid is the distribution of the pressures on the surfaces of the cap which also determines the largest part of the inline force and vertical force[1]. In order to characterize the centroidal moment with higher accuracy therefore a new fitting equation is used to include all the terms that have been proven relevant for inline and vertical force characterization. These are horizontal drag, vertical drag, horizontal inertia and vertical inertia.
The newly defined formula reads:

$$M_{CoM,new} = \frac{1}{2}\rho C_{D,mom,x} A D U_0 \sqrt{U_0^2 + W_0^2} + \frac{1}{2}\rho C_{D,mom,z} A D W_0 \sqrt{U_0^2 + W_0^2} + \\ + C_{M,mom,x}\rho V D \frac{\partial U_0}{\partial t} + C_{M,mom,z}\rho V D \frac{\partial W_0}{\partial t} \quad (7.1)$$

In this equation, coefficients $C_{D,mom,x}$, $C_{D,mom,z}$ are defined as drag coefficients and $C_{M,mom,x}$, $C_{M,mom,z}$ as inertia coefficients. Figures 7.12 and 7.13 show the fits obtained with the new expression for regular wave and

---

[1] A minor part is also due to the viscous shear stress.

soliton test cases. The dashed lines show the four components of the total overturning centroidal moment equation.

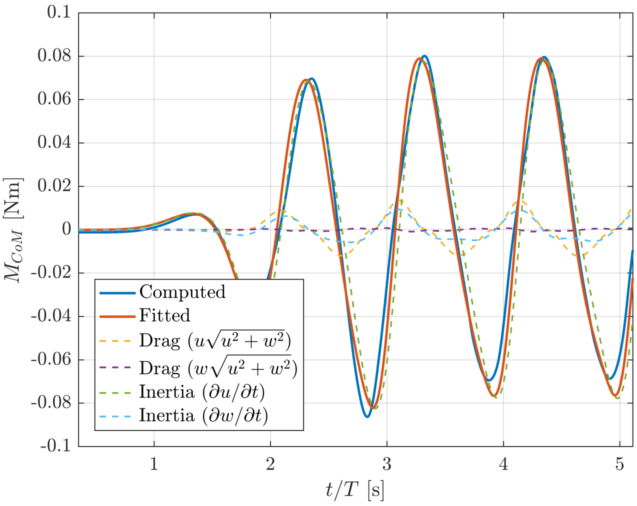

Figure 7.12: Fit of the centroidal moment obtained for test case R3.

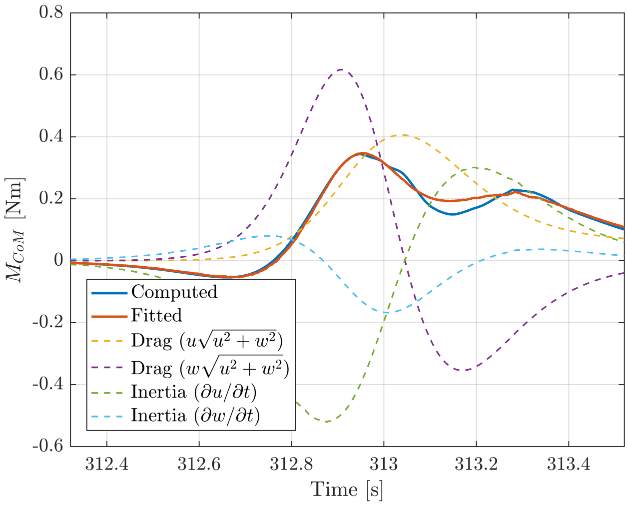

Figure 7.13: Fit of the centroidal moment obtained for test case T202.

Both in the case of the solitary waves and regular waves, the newly obtained fits are almost perfectly matching the moment estimate.
The analysis of all plots obtained shows that the importance of the several components varies significantly among the test cases. In the case of the regular waves, the inline inertia is by far the most important component determining phasing and amplitude of the load. On the contrary, for solitary wave tests all component are approximately equally important considering their contribution to the total load.

7.3. Coefficients results

In this section the coefficients obtained through the fitting procedures described in the previous section are presented. The coefficients are computed for the totality of the velocity cap. The results are plotted against relevant parameters such as KC and H/h.

The coefficients computed for the breaking wave cases are not included in the following graphs. All coefficient results are also reported in tables in appendix F.

7.3.1. Inline force coefficients

In figure 7.14, the inline coefficients are plotted against KC. In this plot, it is easy to individuate the original test cases on the right (the highest KC numbers), the additional solitary wave tests at the center/left and the regular wave tests on the far left (lowest KC). It can be observed that the drag coefficients tend to assume bigger values for decreasing KC. The biggest drag coefficients computed are in fact relative to the regular wave tests.
This behaviour of the drag coefficient does not correspond to what is found in literature for a smooth vertical cylinder in oscillating flows. In his research on low KC number regimes, Sarpkaya (1986) found that for any value of the parameter β, C_D experiences a dip at approximately $KC = 2-4$. No dip is observed in plot 7.14 where instead the drag coefficient decreases monotonically with increasing KC.

The inertia coefficient instead shows a much smaller variation. The highest values correspond again to the regular wave simulation and they are about 0.9. For KC bigger than 10 a small decrease is observed until the value of 0.8 that then stays relatively constant. The evolution of the C_M correlates to the case of a smooth cylinder much better than C_D. Even if the magnitude of the coefficient is considerably smaller than in the case of a cylinder, its independence of the KC number is also observed in the results by Sarpkaya (2010) for comparable values of β.

It is remarkable that the behaviour of the inline force coefficients does not seem affected by the wave type. Even if an overlapping area where both solitons and regular waves results are known for the same KC number range, no jump in the value of the coefficients between the regular waves and solitary waves is observed.

When plotting C_D and C_M against the dimensionless wave height (H/h), instead, the curve described by the regular wave estimates differs from the one described by the ones of the solitary waves (see figure 7.15). It is difficult to assess with certainty if the trend is different in the case of the the inertia coefficient because, as already noted, it remains relatively constant. The difference is instead quite apparent in the case of the drag coefficient which, in the case of the regular wave, has higher values than in the case of solitary waves for similar vales of H/h.

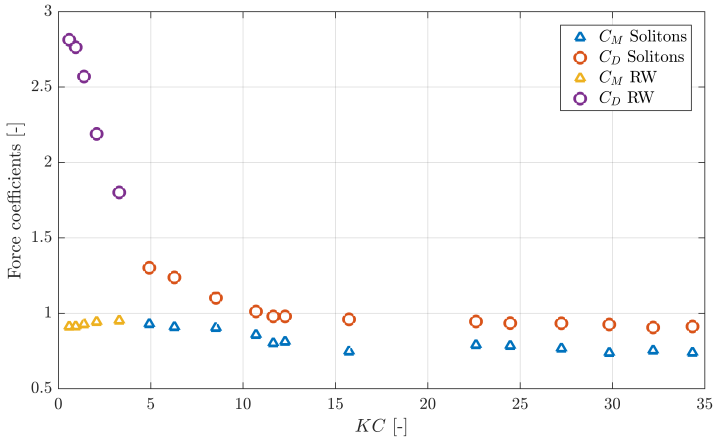

Figure 7.14: Inline force coefficients plotted against the KC number.

In order to deepen the investigation on the inline force coefficients, the loads are also recorded for the two parts of the velocity cap separately. Section 7.4, presents the results of that analysis which are used to understand better the magnitude and the behaviour of the total coefficients presented here.

7.4. Partition of the structure

Dividing the geometry of the velocity cap in two patches, it is possible to analyze the two fractions of the inline force independently.

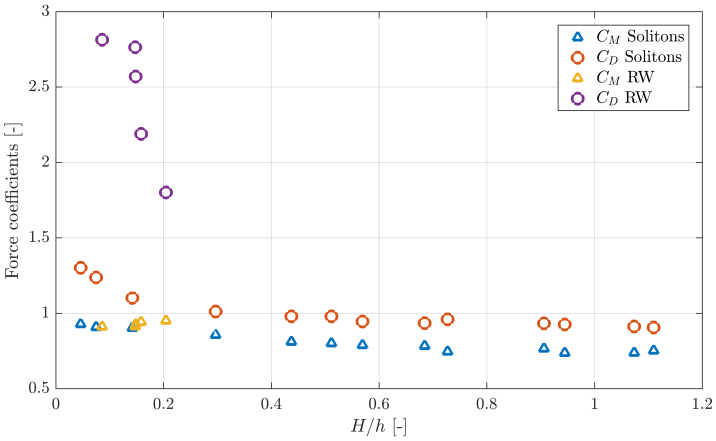

Figure 7.15: Inline coefficients versus the ratio H/h.

The aim of this section is to determine the force coefficients for the inline force relative to the two components of the velocity cap in order to understand how the total coefficients presented in the previous section build up. For this purpose, the force fits are computed with two new velocity estimates taken at different heights in the water column. In the case of the computations regarding the lower cylinder the estimate of the undisturbed velocity is given by the OpenFOAM reconstruction probed at 0.04 m from the bottom, while for the top part the velocity is probed at 0.13 m from the bottom. The geometrical properties of the velocity cap appearing in the fitting equation are also adjusted and they are relative to the single part of the cap considered (see appendix A). Figure 7.16 represents in a 3-dimensional sketch the location of the probed velocity.

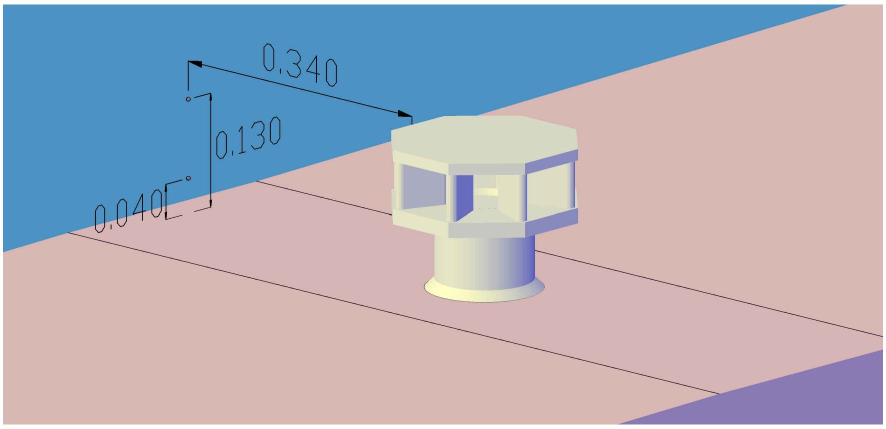

Figure 7.16: 3-dimensional sketch of the locations from which the velocity used for the computation of the partial coefficient was extracted. The dimensions are in meters.

The presentation of the results is based on the dimensionless parameters Re, KC and β defined locally for the two parts of the structure. The velocity estimates are based on the OCW3D reconstruction and they are taken from the same respective heights discussed above and shown in figure 7.16. Table 7.4 reports the results of the computations for the three dimensionless numbers.

Table 7.4: Re, KC and β defined for the two components of the velocity cap.

	Top part			Cylinder		
Test case	Re $\times 10^5$	KC	Re/KC $\times 10^3$	Re $\times 10^5$	KC	Re/KC $\times 10^3$
T101	1.91	27.24	7.01	0.92	54.50	1.69
T102	2.09	36.04	5.81	1.02	72.11	1.41
T103	2.31	43.00	5.37	1.12	85.99	1.31
T201_5	1.47	11.64	12.64	0.72	23.30	3.10
T201	1.78	24.47	7.28	0.87	48.96	1.78
T202	2.34	32.21	7.27	1.14	64.45	1.77
T203	2.37	36.68	6.47	1.16	73.39	1.58
T301_4	1.02	10.70	9.58	0.51	21.42	2.37
T301_5	1.41	12.28	11.48	0.70	24.57	2.84
T301	1.69	22.61	7.48	0.83	45.24	1.85
T302	2.31	29.83	7.76	1.14	59.68	1.90
T303	2.50	34.34	7.29	1.23	68.70	1.79
T401_1	0.19	4.93	3.77	0.09	9.86	0.94
T401_2	0.30	6.29	4.77	0.15	12.58	1.19
T401_3	0.56	8.53	6.58	0.28	17.08	1.64
R1	0.23	0.61	37.82	0.11	1.21	9.46
R2	0.37	0.97	38.07	0.18	1.93	9.52
R3	0.44	1.41	31.35	0.22	2.82	7.84
R4	0.52	2.09	24.71	0.26	4.18	6.18
R5	0.68	3.33	20.51	0.34	6.65	5.13

Figure 7.17 gives an example of the partial force time series plotted together with the total signal. In the solitary wave test cases approximately 70 % of the total load is acting on the top part of the cap and slightly less for the regular wave cases (60-65%).

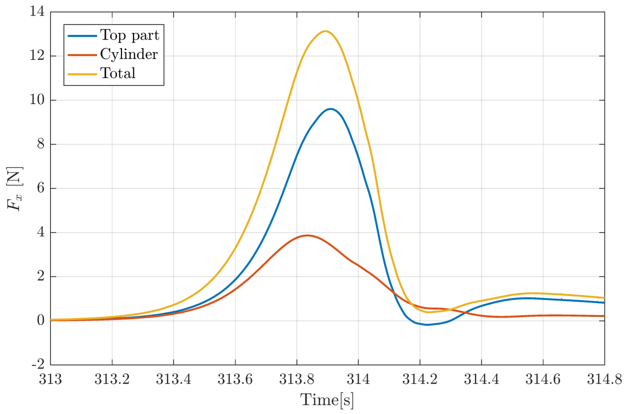

Figure 7.17: Force decomposition for the two parts of the velocity cap.

Fitting the two force signals for all test cases allows to determine the two sets of inline force coefficients. The numerical results are included in appendix F. The values of the force coefficients are then plotted against the KC number in figures 7.18 and 7.19.

The results plotted in the first graph can be directly compared with the experimental data regarding cylinder in unsteady flows found in literature. The data by Sarpkaya (2010) for the drag coefficient on a smooth cylinder presented in figure 2.2 relate well with the computed C_D of figure 7.18. The increase of the drag until the value of about 1 for KC number smaller than 10 is observed in the present numerical results and in the ones from literature. The scatter observed in the right-hand part of the graph can be due to the fact that the

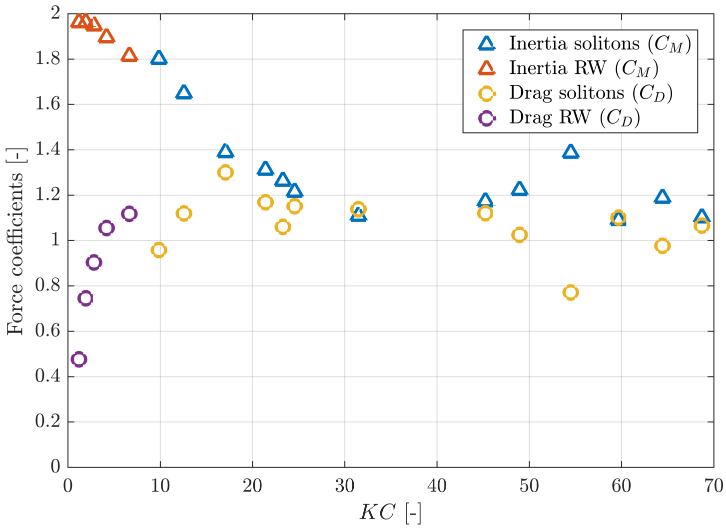

Figure 7.18: Drag and inertia coefficients for the support cylinder of the velocity cap plotted over the local KC number. Given that the diameter of the cylinder is smaller than the one of the top part the values of KC are always bigger.

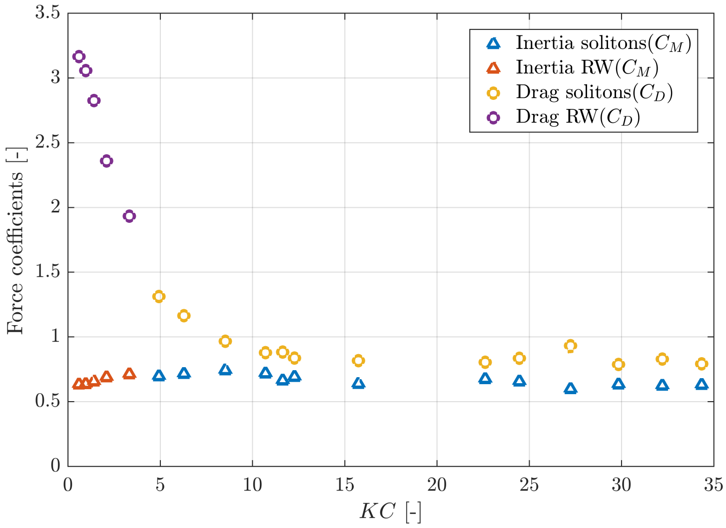

Figure 7.19: Drag and inertia coefficients for the top part of the velocity cap plotted over the local KC number.

flow field that generates the force on the cylinder is also affected by the presence of the top part. Figure 7.20 shows that indeed the quality of the force fit for the signal of the force acting on the cylinder is sometimes of poor quality. The wide shape of the force signal suggests that the velocity estimate used for the cylinder is not representative enough of the flow close to the cylinder.

With regards to the inertia coefficient of figure 7.18, a good match with the theoretical value of 2.0 is found for KC smaller than 10. However, unlike in the results by Sarpkaya (2010), for increasing KC only a decrease of the inertia coefficient is observed and not a local minimum.

Overall it can be said that the loads and the coefficients found for the support cylinder of the velocity cap show good agreement with the reviewed values of the coefficients obtained in the case of a single isolated cylinder in unsteady flows. The differences observed can be due to the modification of the flow field caused by the presence of both the top part and the cylinder.

The analysis of figure 7.19 instead shows approximately the same behaviour already observed for the total coefficients. It it clear now that given that the biggest part of the force is acting on the top part of the velocity cap, the coefficients computed for this part alone play a predominant role in defining the total coefficients.

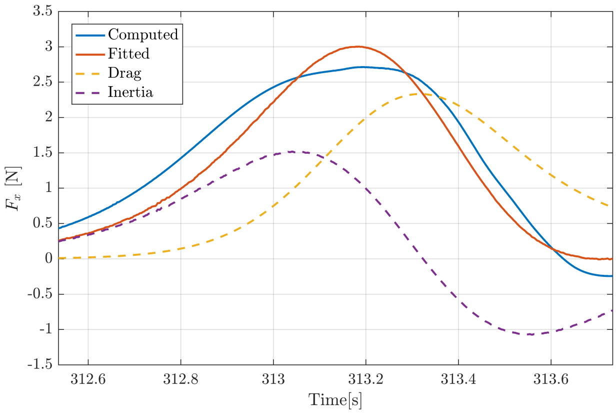

Figure 7.20: Force fit for the inline component acting on the support cylinder of the velocity cap. Data relative to test case T301.

As observed when describing the experimental estimate of the force coefficients, the reason for the low value of the inertia coefficient can be related to the volume estimate that is overestimating the actual volume. Nevertheless, the constant value of the coefficient is in good agreement with what found in literature for values of β bigger than 5000. In the same way for the drag coefficient, it can be assumed that the frontal area suggested is too small for small KC number where every small column between the openings of the top cap feels the flow almost individually.

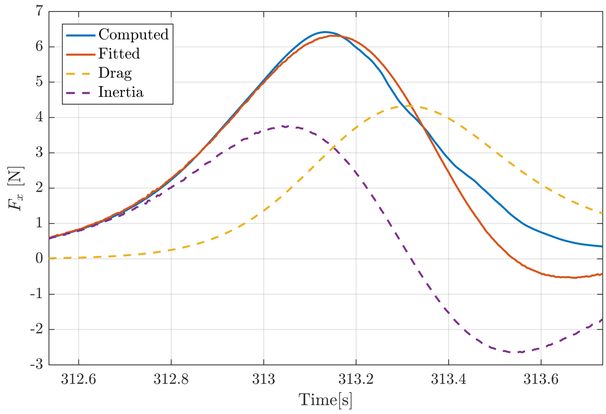

Figure 7.21: Force fit for the inline component acting on the top part of the velocity cap. Data relative to test case T301.

Putting the results of figure 7.18 and 7.19 together, it can be understood that the value of the force coefficients of the total structure are mainly determined by the coefficients found for the top part. C_D for the total structure is approximately the one found for the top part of the cap reduced of an offset while C_M resemble closely the inertia coefficient of the top part for KC bigger than 20 and it is slightly increased for lower values of KC due to the effect of the cylinder.

7.4.1. Vertical force coefficients

In this and in the next section the coefficients are again computed for the totality of the structure.
In the case of the vertical force characterization a direct comparison of the experimental and numerical results was not carried out. In chapter 5, the vertical loads were still showing a considerable mismatch. Comparing force coefficients relative to those signals would not produce valuable information as the origin of the difference in the force signals is still not fully explained. As in chapter 6 the analysis is focused on the coefficients relative to the new vertical force equation 6.3 which has been shown to provide a better match with the force signal. The estimate of the original lift coefficient C_L is only reported in table F.3 included in appendix F, together with the ones obtained with the new formula, and it is not included in the following graphs.

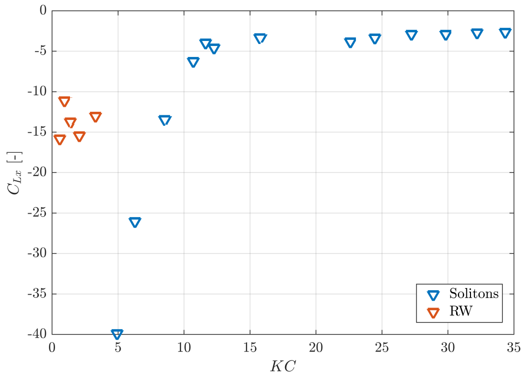

Figure 7.22: Horizontal drag coefficient versus the KC number.

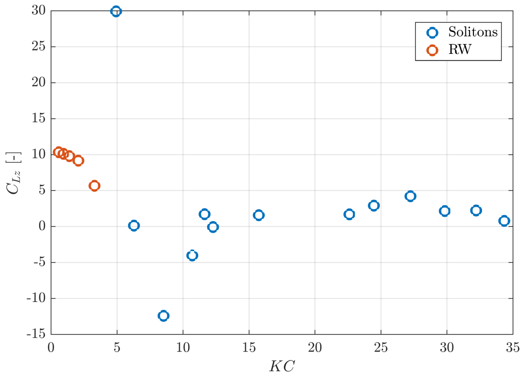

Figure 7.23: Vertical drag coefficient (C_{Lz}) versus the KC number.

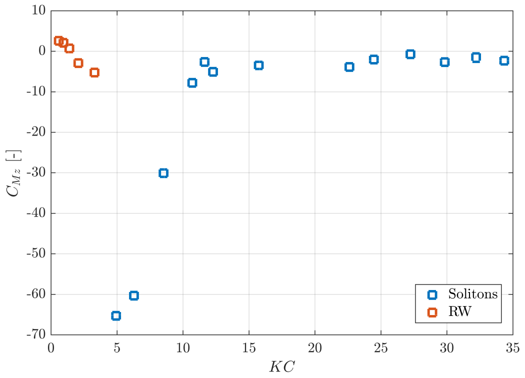

Figure 7.24: Vertical inertia coefficient (C_{Mz}) versus the KC number.

The estimates of the three coefficients of formula 6.3 are plotted here against the KC number and the dimensionless wave height.
The expansion of the data set made the picture of the vertical force coefficients more complex and the range of values that the vertical force coefficients assume is much wider than in the case of the inline force ones.
The dependency of the KC number is depicted for the three force coefficients in figures 7.22, 7.23 and 7.24.
The correlation with the H/h ratio is clear only in the case of the horizontal drag coefficient C_{Lx} and therefore only this coefficient is plotted against this ratio (see figure 7.25).
For the three coefficients, the values and the trend shown change considerably between regular waves and solitons. besides, among the solitary wave cases, a big difference in value is observed between the last three additional cases (T401_1, T401_2 and T401_3) and the others. The computed values of KC and H/h were the lowest for these three test cases since the generated wave is low, the shoaling is contained and the water depth is the highest.

In the case of the regular waves, the horizontal drag coefficient C_{Lx} does not show a clear dependency of the KC number nor of H/h and it ranges between -16 and -11 approximately. In the case of the solitary waves it instead shows a positive trend when plotted both against KC and H/h. The slopes of the curve seems changing depending on the KC number: steeper for low values of KC and flatter for high ones. The solitary wave cases corresponding to the lowest KC numbers give values of C_{Lx} between -40 and -13 while in the case of the other test cases the values stays bound between -6 and -1.5.

With regards to the vertical inertia coefficient (C_{Mz}), in the case of regular waves, its value decreases changing sign with increasing KC number, from 2.6 to -5.2. In the case of the solitary waves, the vertical inertia coefficient remains always negative. This coefficient reaches big negative values (from -60 to -30) in the solitary wave cases corresponding to the lowest KC numbers. As for C_{Lx}, the lowest values and the highest variation of the vertical inertia coefficient C_{Mz} are found for low KC but as can be seen in figure 7.24 when the overall steepness of the graph decreases for higher values of KC, this coefficient stays in the range between -8 and 0 approximately without showing a clear dependency of KC.

It is more difficult to characterize the vertical drag coefficient (C_{Lz}). In the case of the regular waves, this coefficient correlates negatively with KC and it varies between 10 and 5 approximately. In the case of the solitary wave cases it does not show a clear trend when plotted against KC. Even though the relevance of the vertical drag has been proven by the goodness of the fit obtained, it is still uncertain how accurate the estimate of the relative coefficient is. Especially for test cases T401_1, T401_2 T401_3, the vertical velocity amplitude is very low compared to the one of the vertical load and the fitting method determined at times high values (positive and negative) of the coefficient even if the contribution to the total fit remains low.

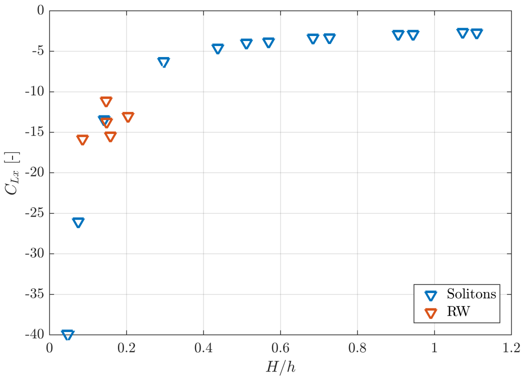

Figure 7.25: Horizontal drag coefficient versus the dimensionless wave height H/h.

In the case of C_{Lz} and C_{Mz} a correlation is also found with the eccentricity of the wave defined as $W_{0,max}/U_{0,max}$ (see figures 7.26 and 7.27). Neglecting the three data points on the left-hand side of the graph of figure 7.26 are relative to solitary wave tests involving the lowest low KC number, the vertical drag coefficient shows a mild positive correlation with the eccentricity parameter $W_{0,max}/U_{0,max}$. Such a correlation has not been found when fitting the experimental force signals of the six non-breaking solitary wave cases.

Looking at figure 7.27, the vertical inertia coefficient correlates much better with this property of the wave than with the KC number. For a value of the eccentricity equal to 0.15 approximately the coefficient is computed for both solitary waves and regular waves but they do not match. Even if the comparison is based on a small number of points this suggests that also other characteristics of the wave may influence the value of the vertical inertia coefficient.

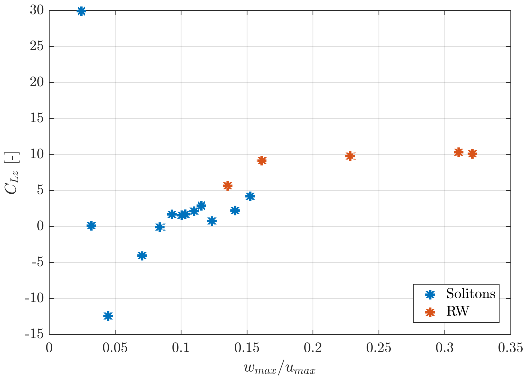

Figure 7.26: Vertical drag coefficient (C_{Lz}) versus the eccentricity of the orbital motion expressed by the parameter $W_{0,max}/U_{0,max}$

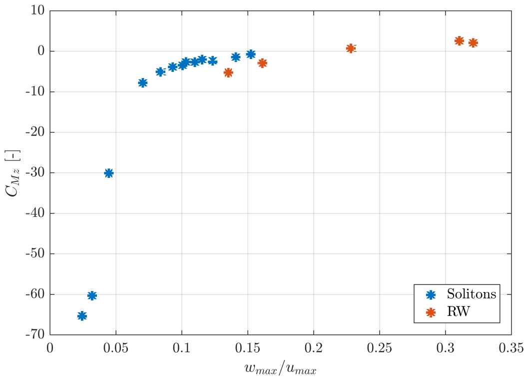

Figure 7.27: Vertical inertia coefficient (C_{Mz}) versus the eccentricity of the orbital motion expressed by the parameter $W_{0,max}/U_{0,max}$.

To conclude, it is clear that further research is needed on the the newly defined vertical force coefficients for regular and solitary waves. The need of these coefficients is more urging in the case of the uplift generated by regular wave, while in the case of a solitary wave the dynamic pressure downwards can probably be omitted in a design stage because it would only improve the overall stability of the structure.

7.4.2. Centroidal moment coefficients

This section focuses on the four new coefficients defined in equation 7.1. As in the case of the vertical force coefficients, the moment coefficients assume different values and show different trends between regular and solitary wave cases. Figure 7.28 shows the results for the four coefficients extracted for the centroidal moment. The relation with other parameters such as H/h has been studied but no clear correlation is found and the plots are not included here. For all coefficients the amplitude stays on the order of $10^{-}1$ except for the case of $C_{D,mom,z}$ (vertical drag moment coefficient) which is one to two order of magnitude bigger. One last observation is that the coefficients computed for solitary waves are always positive the only exception being $C_{M,mom,x}$ (horizontal inertia moment coefficient) which is always negative. In the case of the regular waves instead the coefficient often change sign the only exception being again $C_{M,mom,x}$ which stays negative.

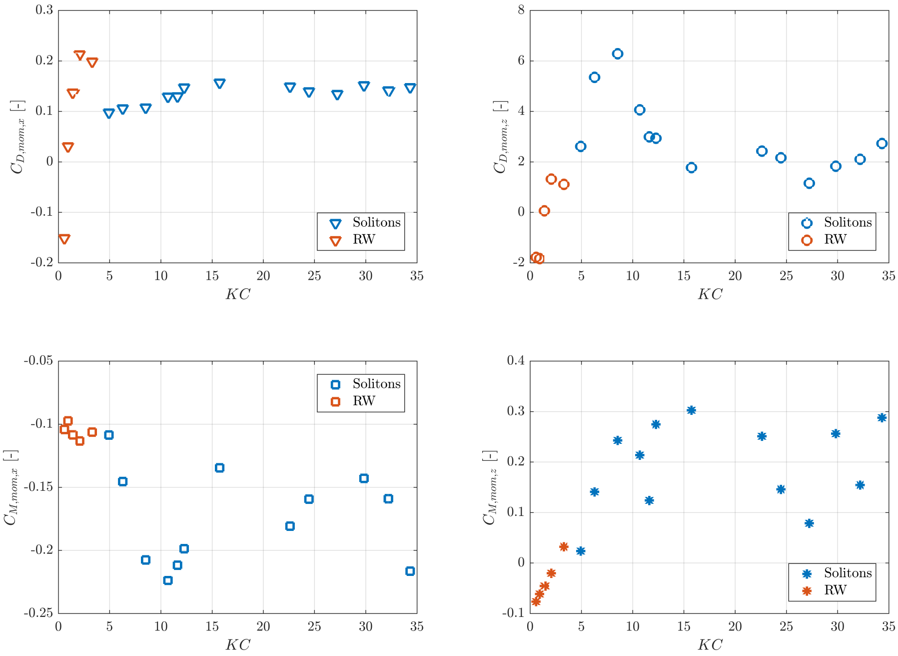

Figure 7.28: Centroidal moment coefficients versus the KC number.

As for the vertical force coefficients, the moment coefficients have been defined in this thesis for the first time and it is not recommended to use the values found in a design. However this results can be used as a starting point for further research.

7.5. Influence of the discharge

In order to model a case more representative of the working conditions of the velocity cap, two additional simulations (one for the solitary waves and one for the regular waves) are considered including the effect of a discharge through the velocity cap.

7.5.1. Numerical set-up

The two simulations are identical to test cases T201 and R3 with regards to wave conditions, domain size and boundary conditions. However, the geometry of the velocity cap is modified in order to allow a discharge to flow through it. The outlet of the pipe is modelled with a new patch on which the boundary conditions for pressure and other variables are set to a zero gradient and the velocity to a uniform constant value to control the discharge. The value of the velocity in the internal field of the computational domain is instead set to zero. The simulations therefore include a few seconds before the waves reach the velocity cap so that the velocity field in the space inside the and closely surrounding the cap can adjust to flow induced by the discharge. This condition and the new velocity cap used are shown in figure 7.29.

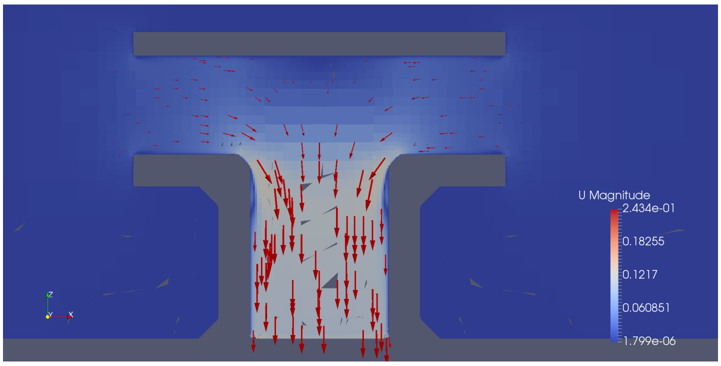

Figure 7.29: Longitudinal cross-section at the center-line of the new geometry used during a simulation. The red arrows have a dimension proportional to the velocity of the water. At instant depicted in the figure no wave has arrived at the velocity cap yet.

The different geometry of the velocity cap also determines a different vertical load in absence of the discharge (hydrostatic conditions). In order to determine the total force in absence of any flow, in fact, the model integrates the pressure field over all surfaces of the velocity cap. The integral over horizontal surfaces results in the vertical component of the force. Given that the total horizontal surface used in the hollow model is different from the one of the full one, the hydrostatic vertical force differs as well. The hydrostatic component of the vertical force is subtracted before presenting the results and it is determined by means of a separate simulation run with the same hollow geometry but no discharge nor waves.

The value of the discharge is derived from the study by Christensen et al. (2015). The shape of the velocity cap analyzed in their paper is similar to the one studied here. Therefore the discharge applied at pipe outlet is obtained by means of scaling considerations from the value used by the authors. The scaling factor takes into account the different dimension of the velocity cap. In the numerical simulation by Christensen et al. (2015) the vertical pipe has an inner diameter of 5.5 m while in the modified shape of the cap used in this thesis the inner diameter is 0.076 m. The computations done to come to the final value of the velocity imposed as boundary conditions are summarized in table 7.5. The exact value of the velocity used in the analysis by Christensen et al. (2015) is not known and the value reported here is an estimate. In the present work, for simplicity instead of the result 0.074 m/s, the value of 0.1 was used.

Table 7.5: Main dimensions needed to come to the value of the velocity to apply to the pipe outlet. The scale computed between the model used in this thesis and the model used by Christensen et al. (2015) is 1:72.37.

	Christensen et al. (2015)	Present thesis
Inner pipe diameter [m]	5.5	0.076
Area of the pipe [m^2]	23.75	0.0045
Discharge [m^3/s]	15	0.00034
Velocity [m/s]	0.63	0.074 → 0.1

7.5.2. Force analysis

In the plots of figure 7.30 and 7.31, the inline and vertical loads relative to the two test cases involving the discharge are plotted together with the results obtained for the same test cases without a discharge.

The results show that the difference on the inline load is very small. In both cases the case, including a discharge results in a slightly larger inline force but the difference is approximately 4 % in the case of the solitary wave and less than 2 % in the case of the regular waves. This leads to the important conclusion

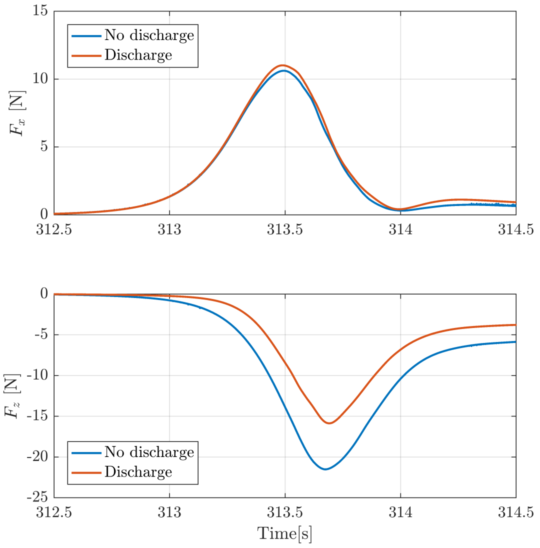

Figure 7.30: Inline and vertical force for test case T201. The results with and without discharge are plotted together. The simulated time interval extends from second 309.5 until second 315

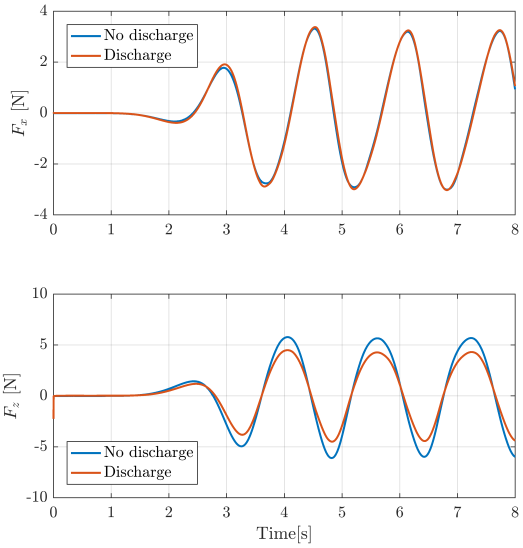

Figure 7.31: Inline and vertical force for test case R3. The results with and without discharge are plotted together. The entire simulated time interval is plotted.

that no big differences are expected with regards to the inline force if the simulations include or not the discharge considered here. The findings of the previous sections are therefore expected to be only slightly underestimating the more realistic scenario in which the velocity cap is discharging water when attacked by the waves. With regards to the vertical loads instead, its amplitude decreases when a discharge is taken in by the cap. Both the force downwards determined by the solitary wave and the uplift generated by the regular waves are smaller in absolute value when a discharge is present. The decrease is about 22 % for the maximum pressure downwards determined by the solitary wave and about 24 % for the maximum uplift determined by the regular waves.

The findings can be compared with the results by Mogridge and Jamieson (1978) who also modelled a discharge passing through a diffuser cap. In their study the discharge was exiting the cap and being discharged in the ambient flow while here the opposite happens. Nevertheless, the difference in inline load observed above compares quite well to what stated in their analysis.
In the case of the vertical load the authors observed a considerable increase of the uplift force determined by regular waves. This increase can be explained by the fact that the continuous flow of water is exerting a vertical push on the cap while flowing out.

The force coefficients for the newly obtained force signal are computed using the undisturbed velocity probed in the simulations that do not include the discharge and the geometrical properties determined for the filled velocity cap. Comparing the force coefficients for the two scenarios (discharge, no discharge) for the two test cases shows that in the case of the inline load the most considerable difference is on the drag coefficient. In the study by Christensen et al. (2015), the authors suggested that this additional flow of water could change the angle of attack and therefore the added mass of the structure. However it is observed here that the biggest variation determined by the discharge influences the drag rather than the inertia coefficient.

In the case of the vertical load it is more difficult to relate the differences in the load to the differences in the coefficients. However, the variation interests in the most significant way the vertical inertia coefficient which is defined as an added mass coefficient. The argument by Christensen et al. (2015) can therefore be valid with regard to the vertical added mass. The fact that the vertical component of the flow is deflected at the height of the openings by the presence of the discharge might be responsible for a reduction of the volume of water inside the cap that is interacting with the outer flow and, as a consequence, of the added mass. The reason why this effect is so mild in the vertical can be explained by the fact that the amplitude of the horizontal velocity is considerably larger than the vertical one and therefore the deflection operated by the discharge is not as relevant.

Table 7.6: Drag and inertia coefficients computed for the inline load in the case with and without discharge.

Test case		C_D	C_M	C_{Lx}	C_{Lz}	C_{Mz}
T201	Disch.	0.99	0.80	-2.12	4.60	-0.64
	No disch.	0.94	0.79	-3.34	2.92	-2.00
R3	Disch.	2.74	0.94	-10.50	9.39	0.40
	No disch.	2.57	0.93	-13.72	9.80	0.75

As a concluding remark, it is good to note that the uplift determined by the regular waves is reduced by the effect of the discharge and this is working in favour of safety. Therefore the coefficients determined in absence of discharge are stricter parameters which can be more relevant in a design.

7.6. Summary

In this section the numerical results computed by the N-S/VOF solver are used to define coefficients for the inline force, the vertical force and the overturning moment around the centroid.

It was found that the inline coefficients correlate best when plotted against the KC number. The definitions of KC used differ for solitary wave and regular wave and the correlation found suggests that they manage to link the properties of the flow in the two wave conditions.
The specific values of the coefficients are mainly determined by the fraction of the load acting on the top part of the cap as could be observed by looking at the partition of the inline load between top part of the cap and support cylinder.

Vertical force and moment coefficients found are plotted against several parameter and the best correlation is found with the KC number. In the case of the vertical force coefficients C_{Lz} and C_{Mz}, a correlation is also found with the eccentricity of the wave orbital motion expressed as W_0/U_0. However more research is needed in order to better characterize these two loads.

At the end of the chapter the analysis of the more realistic scenario of a discharge flowing through the cap is also presented. This condition has a really small effect on the inline load while the vertical force results reduced in amplitude. This decrease is thought to be related to a reduction on the vertical added mass of the cap caused by the flow deflection due to the discharge.

8

Discussion

In order to analyze the significance of the concepts and findings presented in the previous chapters and their relations with previous works, the discussion is organized as follows. At first, the newly suggested vertical and centroidal moment equations are discussed. Secondly, the validity and limitations of the numerical model validated in this thesis are discussed. Finally the focus is laid on the comparison between the inline force coefficients estimated in this thesis and the results found in literature.

8.1. Vertical force and centroidal moment equations

The equations most commonly used in literature for the characterization of inline force, vertical force and centroidal moment have been applied in the present analysis in order to estimate the relative coefficients. The utility of these coefficients is that they allow a reconstruction of the loads on a particular structure with an estimate of the undisturbed velocity as the only input. However, the load reconstructions obtained with the original lift force and overturning moment equations provide a poor fit to the records. It is worth observing that in the case of the centroidal moment reconstruction the numerical estimate is the only one available and the results could be compared with any experimental evidence.

The original equations 2.11 and 2.14 are derived for one-dimensional steady flows in which it holds that $W_0 \ll U_0$ and therefore any inertial and vertical component can be neglected (Wei Zhang, 2011).
In the present application instead, the undisturbed flow is unsteady and it has a strong component along the x axis and a smaller component on the z axis. In the case of the vertical force characterization, an attempt has also been made to use a formulation of the Morison equation over the vertical but the obtained results are not significantly better. This approach is often followed in the case of the characterization of the forces on a horizontal cylinder under the action of waves (Ramberg and Niedzwecki, 1982), but in the case of a structure sealed to the bed like the velocity cap it did not result in satisfactory force fits. It is shown that the effect of the vertical drag (dependency of $W_0 \left\| \overrightarrow{u_0} \right\|$) and of the vertical inertia (dependency of $\partial W_0 / \partial t$) can not be neglected in order to come to good force fits.

With regards to the centroidal moment all components which are contributing to the total vertical or inline force are observed to be relevant. To the author's knowledge no studies have been carried out to determine a fitting equation for the centroidal moment characterization for any kind of structure in highly unsteady flows. In the cases reviewed in literature, the flows under analysis were steady or slowly varying and the simple formulation of the centroidal moment equation (eq. 2.14) was giving sufficiently good results (Kornel Kerenyi and Guo, 2009). In the case of a submerged structure under the effect of waves, the said equation does not capture accurately the evolution of the centroidal moment and its use is not recommended in a design.

The newly suggested formulas come from the considerations about which flow components may be responsible for the additional load or moment on the velocity cap and their validity is supported by the improvements on the fits obtained.
The coefficients results, however, both in the case of the vertical force and the centroidal moment are far less

consistent than the ones regarding the Morison coefficients and it is more difficult to characterize their dependency of parameters such as the KC number. This feature is common also for the results regarding the old formulation of C_L according to the lift force equation. It was already pointed out by Sarpkaya (2010) that in the case of a cylinder under the effect of waves the transverse force coefficient C_L experiences dramatic changed at vortex shedding stages. For the case of an intake cap, the characterization of the vertical force and the centroidal moment due to solitary and regular waves is not possible by means of the conventional formulas but the study on the dependencies of the newly defined coefficients still needs to be deepened.

8.2. Validity of the OpenFOAM model

The OpenFOAM model presented in this thesis is an important tool that has the potential to assess the loads on the velocity cap. However the validation process pointed out several aspects which still show discrepancies between the model and the experimental data. The presentation and quantification of these discrepancies is important in the perspective of a safe utilization of the model for design purposes.

8.2.1. Experimental and numerical reconstruction of the velocity field

The PIV measurements on the center-line of the velocity cap allowed a direct comparison with the flow field computed by the CFD model. The Reynolds-averaged results show consistent differences with the PIV ensemble averaged results with regards to the flow separation on the top of the cap and the velocity profile of the jet coming out of the openings of the cap.

In terms of force reconstruction the observed mismatch is certainly having an effect even if it can be assumed that the influence on the inline force estimate is low.
All the forces acting on the structure are computed by the model as the summation of pressure forces and viscous forces. The former are determined integrating the computed pressure field over the surfaces of the velocity cap while the latter are due to the viscous shear stress acting tangentially to the cap surfaces. The forces computed as the integration of the viscous shear stress over the cap patches, in fact, do not exceed 3 % of the total inline load, which is in agreement with what reported by Sumer and Fredsøe (2006). Therefore the biggest part of the load is determined by the pressure forces. The mismatch observed in the flow field reconstruction at the top of the structure is likely to cause a wrong pressure field and shear stress reconstruction. However the former does not results in a net horizontal component and the latter influence the total load only for a fraction of the 3 % already computed.
Therefore, although it is true that the flow separation and the vortex shedding is not accurately captured by the model, these features have little effect on the determination of the peak of the inline load which shows a good agreement with the measurements.

The poor agreement with the tail of the inline force signal and also the error on the peak of the vertical force can be due to an incorrect velocity reconstruction of the model which resulted in an incorrect pressure field.

8.2.2. Experimental and numerical estimate of the inline force coefficients

The comparison between the experimental and numerical estimate of the inline coefficients is used to analyze the degree of accuracy to which the force components are predicted by the model. The coefficients presented in chapter 6, however, are obtained fitting the force records affected by the experimental bias. The pressure component on the base plate determines a difference in the force estimation. The two force signals (numerical and experimental) are therefore simply not comparable since they represent different set-ups.
Hence, the coefficients are re-computed for the corrected force signals presented in chapter 5. Those force estimates have been used in that chapter to show how the numerical results compare to the experimental estimate of the forces.

The comparison is presented in figure 8.1 and it is based on the six original solitary wave cases that did not involve breaking. The inertia coefficients estimated in the two cases are very close and they assume values between 0.8 and 0.7. A bigger difference is observed with regards to the drag coefficient. The C_D estimated fitting the N-s/VOF solver results is generally smaller than the one estimated form the experimental records. The underestimation increases with decreasing KC number reaching up to 19 % in case of test T301 which corresponded to the lowest KC number of these six simulations. One possible reason for the observed mismatch can be that numerical model does not predict accurately enough the evolution of the velocity in proximity of cap. This would result in an underestimation of the form drag and the skin friction (viscous shear stress). However it is important to be also aware that the original force measurements could not be used directly and there is no possibility to assess with certainty how closer to reality the suggested correction brings the results.

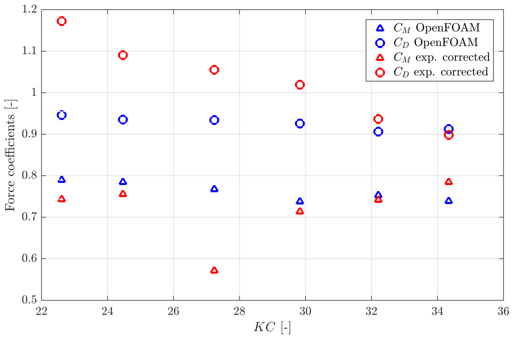

Figure 8.1: Comparison of the inline force coefficients plotted over KC for the six test cases simulated both in physical and numerical model tests. The experimental values are obtained with the corrected force signals (exp. corrected).

It is important to note that the decomposition between drag and inertia and the consequent coefficient estimates are highly dependent of the synchronization used between numerical and experimental time axis. As presented in chapter 5 the validity of this type of synchronization allows to match the wave profiles at the sixth wave gauge in the best possible way. However, in this way, one loses information on the differences between the wave celerity estimated numerically and experimentally.

The origin of the observed difference and the influence of the wave celerity difference on the undisturbed particle motion was not investigated in this thesis.

8.3. Comparison with previous works

The coefficients found in the case of the vertical and moment equations formula have not any documented counterpart in literature and therefore no direct comparison can be made. In the case of the inline force instead many studies have been carried out to classify the inertia and drag coefficients on several geometries.

The coefficients found by Sarpkaya (2010) for a single cylinder in sinusoidally oscillating flows are first analyzed in comparison with the numerical results. The plots of the inertia coefficient found for the geometry of the velocity cap against the KC number (see figure 7.14) showed a similar trend to the one reported by the author for the same range of KC and similar values of β. The magnitude however is different. The drag coefficient is instead showing both a different behaviour and magnitude when plotted against the same parameter. The study by Sarpkaya (1979) focused on a more similar set-up to the present thesis, analyzing two configurations that involved a central pipe surrounded by a circle of smaller cylinders. The values reported by the author for the inertia coefficients do not compare with the numerical results of this study. However the negative trend observed for C_D when plotted against KC is a common feature. The different value of the coefficients found for the velocity cap can be explained based on the estimates of the volume for the inertia coefficient and of the frontal area in the case of the drag coefficient. The way in which these constants were estimated is overestimating the actual volume of the cap and underestimating the actual area of all the surfaces that face the flow.

The clear negative correlation between C_D and KC can therefore be explained by considering the evolution of the flow regime. For low KC numbers the vortex detachment stays contained and the interaction of the wakes shed by the several vertical columns between the openings in the top part of the cap weakly interact with each other. The area that faces the flow is therefore underestimated if only the area that is visible in the front view is considered. In the case of high KC number, the interaction of the wakes is probably heavily influencing the drag force and the flow feels the top part of the cap more as a whole. In this situation, the frontal area becomes a more accurate estimate of the surface of the structure that faces the flow and the drag coefficient decreases consequently to a value close to 1. For the considered values of the frequency number β, the inertia coefficient does not show a big variation. With this regard, it can be noted that for such high numbers of β the added mass does not change considerably for changing KC.

Finally a comparison with the work by Hecimovich (2013) is also addressed. In his thesis, the author analyzed the inline force coefficients for an intake cap which showed a more open geometry than the one of the cap used in this thesis project. The drag coefficient reported is very close to the one found in this study and it shows a similar trend when plotted against KC. The values and the trend of the inertia coefficients are instead different. The difference regarding this parameter cannot be fully explained but it can be related to the different geometry of the velocity cap analyzed: more open in the case of study of 2013 and more bulky in the present application.

9

Conclusions

The presentation of the conclusions is given in form of answers to the research question presented in chapter 1. After the research questions have been answered, this chapter also contains the recommendations for further studies.

The main research question has been formulated as:

"How to characterize the forces on a submerged velocity cap in unsteady flows?"

The answer to this complex question has been sought by by splitting it into three sub-questions.

1. ***What are the characteristic flow features with regards to turbulence and to ensemble averaged flow field along the center-line of a velocity cap under unsteady flow (solitary waves)?***

The study of the flow field has been carried out through PIV measurements taken for the test cases involving solitary waves. In all cases, flow separation occurs even for small velocities due to the sharp edges of the velocity cap. In particular a recirculation zone creates at the top leading edge of the cap which extends with time when the wave is passing. The flow is also observed to develop through the cap as it is shown by the jet coming out of the cap at the height of the openings at the trailing side.

2. ***How to characterize the forces and the turning moment on a velocity cap under different types of wave loads by means of the Morison, lift force and the turning moment equation models?***

The Morison equation is able to provide good force fits for the inline force signal. It is observed that drag and inertia components contribute in equal amount to the determination of the peak inline force due to solitary waves.
The characterization of the vertical load and of the centroidal moment, instead, is done by means of different, newly suggested equations which include new terms to better describe the evolution of the relative load. In the case of the vertical force the contributions that are shown to be important are the horizontal drag, the vertical drag and the vertical inertia , while in the case of the centroidal moment they are the horizontal drag, the vertical drag, the horizontal inertia and the vertical inertia. The new equations (eq. 6.3 for the vertical force and 7.1 for the centroidal moment) are shown to provide much better fits to the load records than the original equations (eq. 2.11 and 2.14).

3. ***To what extent can the loads and the flow field be reproduced with a detailed CFD model?***

In order to come to a validation of the model the the use of a turbulence closure is necessary. The N-S/VOF solver used with a slightly modified version of the standard k-ωSST turbulence closure gives a reconstruction of the inline load that gives an error on the peak of the prediction within 8 % with respect to the measured forces. In the case of the vertical load the observed mismatch reaches 14 %.

The flow field reconstruction captures with a good accuracy the development of the flow when it remains potential around the structure as the comparison with the PIV measurements has shown. However where the structure is inducing turbulence in the flow the prediction of the model shows differences from the measurements that in some areas are considerable.

To dig deeper in the capabilities of the OpenFOAM, the force and moment coefficients were computed from the numerical estimates of the loads obtained for a set of simulation including solitary and regular wave cases.
The fits of the inline force showed that inertia and drag are equally contributing in determining the peak inline force in the case of the solitary wave cases, while inertia is dominant in the case of the regular wave cases. Drag and inertia coefficients correlate well with the two definitions of KC number adopted for regular and solitary waves and it seems that the coefficients results between regular and solitary waves converge to the same values for similar value of KC. The inertia coefficient varied very little throughout the simulations, assuming values between 0.75 and 0.95. The drag coefficient assumed a wider range of values: from 2.8 in the case of low KC until a relatively constant value of 0.95 for KC bigger than 10-15. The comparison with the coefficients obtained from the corrected experimental records shows that the inertia coefficient is in good agreement while the drag coefficients results slightly underestimated by the model and the underestimation seems increasing with decreasing KC.
The coefficients defined for the vertical force and centroidal equation experience a considerably bigger range of variation and they show different trends and values depending on the type of wave analyzed.

The main results regarding the coefficients are summarized in table 9.1.

Table 9.1: Summary of the force and moment coefficients. The minimum maximum and mean value are computed without considering the three test cases for which breaking was observed.

	Solitary waves			Regular waves		
Coefficient	Min	Max	Mean	Min	Max	Mean
C_D	0.91	1.30	1.01	1.80	2.81	2.43
C_M	0.74	0.93	0.81	0.91	0.95	0.93
C_{Lx}	-39.88	-2.63	-8.90	-15.82	-11.11	-13.82
C_{Lz}	-12.41	29.92	2.38	5.80	10.34	9.02
C_{Mz}	-65.28	-0.70	-14.42	-5.21	2.60	-0.53
$C_{D,mom,x}$	0.10	0.16	0.13	-0.15	0.21	0.09
$C_{D,mom,z}$	1.16	6.28	2.96	-1.83	1.32	-0.22
$C_{M,mom,x}$	-0.22	-0.07	-0.16	-0.11	-0.10	-0.11
$C_{M,mom,z}$	0.02	0.30	0.19	-0.08	0.03	-0.03

The capabilities of the OpenFOAM model are also explored by simulating the case of a discharge passing through the velocity cap. According to the computational results the inline force due to a discharge taken in by the cap is higher by few percents (2 - 4 %) while the vertical load is considerably smaller in amplitude (22 - 24 %). Computing the Morison coefficients in the two cases shows that largest variation interests C_D meaning that the perturbation of the flow field due to the discharge affects more the drag force than the added mass properties of the structure. The considerable variation observed for the vertical force can instead be related to a variation of the vertical added mass due to the fact that the discharge changes the angle of attack of the flow.

9.1. Recommendations and future works

The final recommendations regard critical aspects observed during the research.

- In first place, the experimental set-up used to study the loads on the velocity cap determined a force bias that needed to be taken in account when comparing those records with the numerical results. For future campaigns, a set-up needs to be prepared such that the water penetration under the base plate is prevented.
- With regards to the numerical model, it was noted the importance of obtaining a good mesh in the region near the structure. In chapter 5 it is observed as the OpenFOAM utility used to generate the mesh failed in properly refine the mesh close to some edges. In order to improve the validity of the results, the mesh should be correctly refined in this regions. This together with a sensitivity analysis

on other turbulence closures could lead to better understanding of the discrepancies observed and possibly to an improvement of the force results.

- Finally, it needs to be pointed out that the coefficients reported for the vertical force and moment fits can be the object of deeper research and for the time being it is not recommendable to use the results reported in this thesis for a design.

Looking at the future, possible further developments are listed below.

- The present project could not exploit in the analysis all the data collected during the experiments. The next phase of the research on load characterization for a velocity cap could focus with more detail on the irregular wave and N-wave tests not considered here. An experimental estimate of the force coefficients would be extremely useful, especially for the cases on irregular waves where the KC number is generally lower than for solitary waves. This could allow assessing whether the underestimation of the drag coefficients persists and if it evolves in some way and whether the estimate of the inertia coefficient remains in good agreement with the experimental results.
- The analysis on the dependency of the vertical force and moment coefficients can be object of deeper research. This could be achieved by applying the OpenFOAM model to other wave conditions. Looking at the plots obtained for the dependency of the several force and moment coefficients of the dimensionless number discussed, it can be argued that the addition of test cases in the same range of KC but for different values of other parameters (for instance β and W_0/U_0) would give more information on the coefficients themselves and on the performances of the model. The use of the coefficients in a design could in fact only follow from the full understanding of their dependencies of relevant flow parameters.
- In the perspective of preparing a tool that could aid the design on many sides, a coupling with other numerical models could be an asset. Seeing the importance of the foundations for such an offshore submerged structure a geotechnical model that could compute soil deformation and bearing capacity would be beneficial.

Bibliography

E. Berberović, N. P. van Hinsberg, S. Jakirlić, I. V. Roisman, and C. Tropea. Drop impact onto a liquid layer of finite thickness: Dynamics of the cavity evolution. *Phys. Rev. E*, 79:036306, Mar 2009. doi: 10.1103/PhysRevE.79.036306. URL `https://link.aps.org/doi/10.1103/PhysRevE.79.036306`.

J. Bricker, A. Nakayama, H. Takagi, J. Mitsui, and T. Miki. Mechanisms of damage to coastal structures due to the 2011 great east japan tsunami. *Handbook of Coastal Disaster Mitigation for Engineers and Planners*, pages 385–415, 08 2015.

J. D. Bricker and A. Nakayama. Contribution of trapped air, deck superelevation, and nearby structures to bridge deck failure during a tsunami. *Journal of Hydraulic Engineering*, 140(5):05014002, 2014. doi: 10.1061/(ASCE)HY.1943-7900.0000855. URL `https://ascelibrary.org/doi/abs/10.1061/%28ASCE%29HY.1943-7900.0000855`.

N. Bruinsma. *Validation and Application of a Fully Nonlinear Numerical Wave Tank*. Master's thesis, Delft Univerity of Technology, 2016.

R. Burrows, R. Tickell, D. Hames, and G. Najafian. Morison wave force coefficients for application to random seas. *Applied Ocean Research*, 19(3):183 – 199, 1997. ISSN 0141-1187. doi: https://doi.org/10.1016/S0141-1187(97)00023-0. URL `http://www.sciencedirect.com/science/article/pii/S0141118797000230`.

A. Capel. Hydraulic study for submerged intake/discharge systems of shin-ulchin nuclear power plant units 1 and 2 - physical modelling bed protection and hydraulic forces. *Internal report*, 2012a.

A. Capel. Hydraulic study for submerged intake/discharge systems of shin-ulchin nuclear power plant units 1 and 2 - evaluation and optimization report desk study - task 5 hydraulic forces on the velocity caps and diffusers. *Internal report*, 2012b.

S. K. Chakrabarti. Hydrodynamic coefficients for a vertical tube in an array. *Applied Ocean Research*, 3(1): 2 – 12, 1981. ISSN 0141-1187. doi: https://doi.org/10.1016/0141-1187(81)90080-8. URL `http://www.sciencedirect.com/science/article/pii/0141118781900808`.

C. Chian and R. Ertekin. Diffraction of solitary waves by submerged horizontal cylinders. *Wave Motion*, 15(2):121 – 142, 1992. ISSN 0165-2125. doi: https://doi.org/10.1016/0165-2125(92)90014-S. URL `http://www.sciencedirect.com/science/article/pii/016521259290014S`.

E. D. Christensen, J. Buhrkall, M. C. D. Eskesen, and B. Jensen. Analyses of current and wave forces on velocity caps. In *ASME 34th International Conference on Ocean, Offshore and Arctic Engineering. [OMAE2015-41907]*, St. John's, NL, Canada, 2015. doi: https://doi:10.1115/OMAE2015-41907.

A. Cornett, M. Hecimovich, and I. Nistor. Extreme wave loads on submerged water intakes in shallow water. *Journal of Hydrodynamics, Ser. B*, 27(1):38 – 51, 2015. ISSN 1001-6058. doi: https://doi.org/10.1016/S1001-6058(15)60454-1. URL `http://www.sciencedirect.com/science/article/pii/S1001605815604541`.

Deltares. Wave height meter. `https://www.deltares.nl/app/uploads/2016/04/Programmable-electromagnetic-liquid-velocity-meter.pdf`, 2016. Accessed: 2018-07-15.

A. Engsig-Karup, H. Bingham, and O. Lindberg. An efficient flexible-order model for 3d nonlinear water waves. *Journal of Computational Physics*, 228(6):2100 – 2118, 2009. ISSN 0021-9991. doi: https://doi.org/10.1016/j.jcp.2008.11.028. URL `http://www.sciencedirect.com/science/article/pii/S0021999108006190`.

T. Glasbergen. *Characterization of incoming tsunamis for the design of coastal structures*. Master's thesis, Delft Univerity of Technology, 2018.

M. Hecimovich. *Wave Loads on a Submerged Intake Structure in the Surf Zone*. Master's thesis, University of Ottawa, 2013.

V. Heller. Scale effects in physical hydraulic engineering models. *Journal of Hydraulic Research*, 49(3):293–306, 2011. doi: 10.1080/00221686.2011.578914. URL `http://www.tandfonline.com/loi/tjhr20`.

C. W. Hirt and B. D. Nichols. Volume of fluid (vof) method for the dynamics of free boundaries. *Journal of computational physics*, 39:201–225, 1979.

S. Hughes. *Physical models and laboratory techniques in coastal engineering*. World Scientific, 1993.

D.-S. Hur and N. Mizutani. Numerical estimation of the wave forces acting on a three-dimensional body on submerged breakwater. *Coastal Engineering*, 47(3):329 – 345, 2003. ISSN 0378-3839. doi: https://doi.org/10.1016/S0378-3839(02)00128-X. URL `http://www.sciencedirect.com/science/article/pii/S037838390200128X`.

N. G. Jacobsen, D. R. Fuhrman, and J. Fredsøe. A Wave Generation Toolbox for the Open-Source CFD Library: OpenFoam®. *International Journal for Numerical Methods in Fluids*, 70(9):1073–1088, 2012. doi: {10.1002/fld.2726}.

J. Journée and W. Massie. *Offshore Hydrodynamics*. Delft University of Technology, 2001.

T. S. Kornel Kerenyi and J. Guo. *Hydrodynamic Forces on Inundated Bridge Decks*. Office of Infrastructure Research and Development Federal Highway Administration, 2009.

L. E. Larson and D. I. Downs. Water intake structure, 1975. URL `https://patents.google.com/patent/US3927534A/en`. US3927534A US Grant.

F. Liu. A thorough description of how wall functions are implemented in openfoam. In *Proceedings of CFD with OpenSource Software*, Hamburg, Germany, 2016. URL `http://www.tfd.chalmers.se/~hani/kurser/OS_CFD_2016`.

P. A. Madsen, D. Fuhrman, and H. A. Schäffer. On the solitary wave paradigm for tsunamis. *Journal of Geophysical Research*, 113, 12 2008. doi: doi:10.1029/2008JC004932.

F. Menter. Zonal two equation k-ω turbulence models for aerodynamic flows. *23rd Fluid Dynamics, Plasmadynamics, and Lasers Conference*, pages 201–225, 1993. doi: doi:10.2514/6.1993-2906.

F. Menter and T. Esch. Elements of industrial heat transfer predictions. In *16th Brazilian Congress of Mechanical Engineering (COBEM)*, Uberlandia, Brazil, 11 2001.

G. Mogridge and W. Jamieson. Non-breaking and breaking wave loads on a cooling water outfall. In *Proceedings of 16th Conference on Coastal Engineering*, Hamburg, Germany, 1978. URL `https://icce-ojs-tamu.tdl.org/icce/index.php/icce/article/view/3424`.

J. R. Morison, J. W. Johnson, and S. A. Schaaf. The force exerted by surface waves on piles. *Journal of Petroleum Technology*, 2(5):149–154, 1950.

F. T. Nieuwstadt, B. J. Boersma, and J. Westerweel. *Turbulence, Introduction to Theory and Applications of Turbulent Flows*. Springer, 2016. doi: 10.1007/978-3-319-31599-7.

B. T. Paulsen. *Efficient computations of wave loads on offshore structures*. PhD thesis, The Technical University of Denmark, 2013.

B. T. Paulsen, H. Bredmose, and H. B. Bingham. An efficient domain decomposition strategy for wave loads on surface piercing circular cylinders. *Coastal Engineering*, 86:57–76, 2014.

E. Pita and I. Sierra. Seawater intake structures. In *International Symposium on Outfall Systems*, Mar del Plata, Argentina, May 2011.

S. B. Pope. *Turbulent Flows*. Cambridge University Press, 2000. doi: 10.1017/CBO9780511840531.

S. Ramberg and J. Niedzwecki. Horizontal and vertical cylinders in waves. *Ocean Engineering*, 9(1):1 – 15, 1982. ISSN 0029-8018. doi: https://doi.org/10.1016/0029-8018(82)90041-5. URL `http://www.sciencedirect.com/science/article/pii/0029801882900415`.

A. S. Kiran Raju, s. R. Pilli, M. Sridhar, M. Vendhan, P. Sistla, and M. Venkata Ramana Murthy. Design of intake structure for desalination plant in high energy environment. In *International Conference on Innovative Technologies and Management for Water Security*, Chennai, India, 02 2014.

T. Sarpkaya. Hydrodynamic forces on various multiple-tube riser configurations. *Proceedings of the Annual Offshore Technology Conference*, 01 1979. doi: 10.4043/3539-MS.

T. Sarpkaya. Force on a circular cylinder in viscous oscillatory flow at low keulegan—carpenter numbers. *Journal of Fluid Mechanics*, 165:61–71, 1986. doi: 10.1017/S0022112086002999.

T. Sarpkaya. On the parameter $\beta = re/kc = d^2/\nu t$. *Journal of Fluids and Structures*, 21(4):435 – 440, 2005. ISSN 0889-9746. doi: https://doi.org/10.1016/j.jfluidstructs.2005.08.007. URL `http://www.sciencedirect.com/science/article/pii/S0889974605001519`.

T. Sarpkaya. *Wave Forces on Offshore Structures*. Cambridge University Press, 2010. ISBN 978-0-521-89625-2. URL `https://app.knovel.com/hotlink/toc/id:kpWFOS0004/wave-forces-offshore/wave-forces-offshore`.

B. M. Sumer and J. Fredsøe. *Hydrodynamics around Cylindrical Structures (Revised Edition)*. World Scientific, 2006.

I. A. Svendsen and I. Jonsson. *Hydrodynamics of Coastal Regions*. Den Private Ingeniørfond Technical University Denmark, 1980.

The OpenFOAM Foundation. OpenFOAM v5 User Guide, 2017. URL `https://cfd.direct/openfoam/user-guide`.

J. Tu, G. H. Yeoh, and C. Liu. *Computational Fluid Dynamics - A Practical Approach (2nd Edition)*. Elsevier, 2008; 2013. ISBN 978-0-08-098243-4. URL `https://app.knovel.com/hotlink/toc/id:kpCFDAPAE4/computational-fluid-dynamics/computational-fluid-dynamics`.

C. C. Wei Zhang, Y.J. Ge. Estimation of aerodynamic forces and moments on bridge decks based on two dimensional velocity fields. *Engineering Mechanics Institute Conference*, 2011.

T. Wilting. Wave load analysis on a velocity cap. External traineeship report, Deltares, 2017.

J. Wolfram and M. Naghipour. On the estimation of morison force coefficients and their predictive accuracy for very rough circular cylinders. *Applied Ocean Research*, 21(6):311 – 328, 1999. ISSN 0141-1187. doi: https://doi.org/10.1016/S0141-1187(99)00018-8. URL `http://www.sciencedirect.com/science/article/pii/S0141118799000188`.

World nuclear association. Fukushima accident. `http://www.world-nuclear.org/information-library/safety-and-security/safety-of-plants/fukushima-accident.aspx`, 2018.

G. Xu, C. Cai, and L. Deng. Numerical prediction of solitary wave forces on a typical coastal bridge deck with girders. *Structure and Infrastructure Engineering*, 13(2):254–272, 2017. doi: 10.1080/15732479.2016.1158195. URL `https://doi.org/10.1080/15732479.2016.1158195`.

A

Geometrical properties of the velocity cap

The dimensions of the velocity cap are derived from the original technical drawing of the velocity cap under analysis and are expressed in millimeters. The dimension are obtained scaling down the velocity cap by a factor 46.25 (see chapter 3).

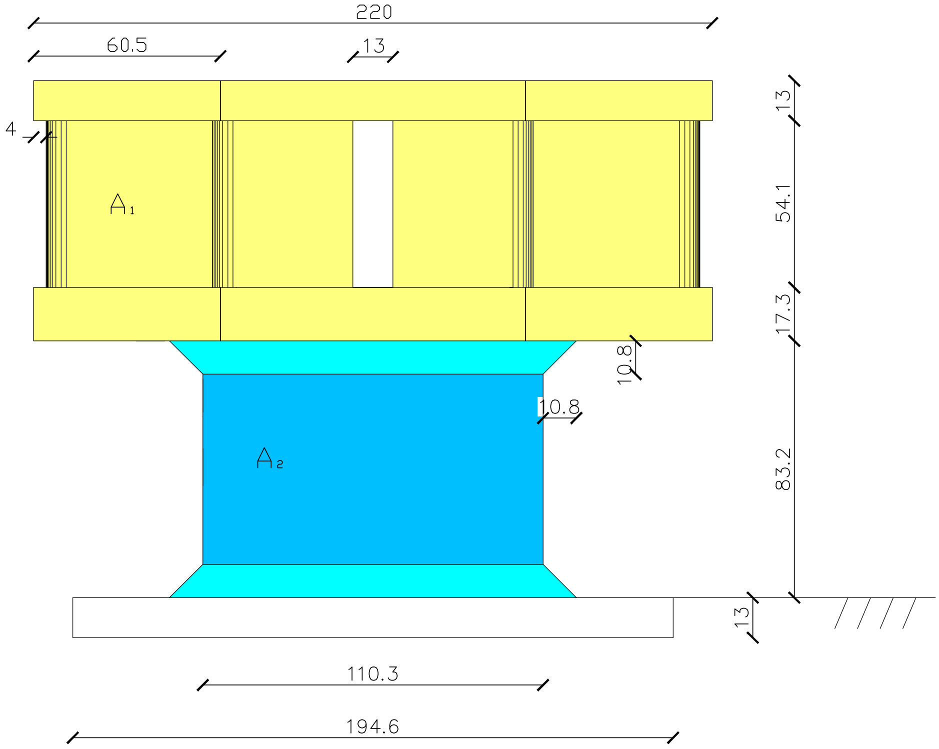

Figure A.1: Front view of the velocity cap.

The model-scale velocity cap is composed by a full vertical cylinder and an open top part and so is the virtual model used in all CFD simulations that do not include a discharge through the cap. In the case of the CFD simulations involving a discharge, instead, the geometry of the velocity cap is different and the vertical cylinder is hollow. However, in all computations of the force and moment coefficients (therefore also the ones in which the velocity cap is hollow) the value of the frontal area and of the volume are the one presented hereafter which assume that the structure is not hollow.

A.1. Frontal area

Drawing A.1 is then used for the determination of the frontal area A and the total volume V used in the force formulas (ch. 6). Looking at the sizes reported, the frontal area is determined summing a component for the top part of the cap and one for the neck drawn in different colours.

$$A_1 = 220 * 54.1 - (13+8) * 54.1 = 17432 mm^2 \tag{A.1}$$

$$A_2 = (2 * 10.8 + 2 * 110.3) * 10.8/2 + (83.2 - 2 * 10.8) * 110.3 = 6915 mm^2 \tag{A.2}$$

Which give a total area of 24347 mm^2.

A.2. Volume

With regards to the volume, first the area of the octagon of the cap and of the bases of the cylinder are computed. The diameter is not constant for the height of the neck and this is taken into account.

$$A_{oc} = 220^2 - 2 * (60.5^2) = 41079 mm^2 \tag{A.3}$$

$$A_{cy,1} = \frac{\pi}{4} * (110.3 + 10.8)^2 = 11518 mm^2 \tag{A.4}$$

$$A_{cy,2} = \frac{\pi}{4} * 110.3^2 = 9555 mm^2 \tag{A.5}$$

Then the volumes:

$$V_{top} = A_{oc} * (54.1 + 17.3 + 13) = 3467110 mm^3 \tag{A.6}$$

$$V_{neck} = A_{cy,1} * 10.8 * 2 + A_{cy,2} * (83.2 - 10.8 * 2) = 837367 mm^3 \tag{A.7}$$

Which give a total volume of 4304476 mm^3. For simplicity it was preferred not to subtract the empty volume that is inside the top part of the cap.

A.3. Center of mass

The center of mass, also called centroid, is a property of the geometry for the cap. For the complicated shape of the velocity cap, the open-source software Salome was used to compute this value. The computations does not take into account the bottom plate that is inserted in the floor of the flume. The computation of the center of mass height is based on the model whose vertical cylinder is filled. The computed centroid is 11.61 cm above the flume floor and this corresponds to the center of mass of the coloured part of the cap in figure A.1 (yellow plus light blue).

B

Irregular wave tests

Similarly to the solitary wave testes, the irregular waves tests are also 9 and come from the combination of the same three water depths described in 3.1.3 and 3 different spectra (and therefore different H_S).

In table B.1, the specification of the irregular waves tests are relative to the steering files properties. In the last column, the number of repetitions of the test (only one in this other tests) is replaced by the total duration of one simulation.

Figure B.2 and B.3 show the horizontal and vertical forces peaks per single wave plotted against the ratio H/h. Even if the peaks of the vertical forces oriented downwards were generally slightly bigger than the one oriented upwards, the uplifts are more important from the poin of view of a design. It is important to remember that the value of H for the irregular waves is the distance between the wave trough and the wave crest obtained by means of a zero-crossing analysis. This is different from the case of the solitary where the surface elevation always stands above the still water level.

As found by Cornett et al. (2015) the inline force peaks show a positive linear trend when plotted against H/h. Furthermore, differently form the case of the solitary waves where the maximum vertical force is a pressure downwards and no lift was observed, in the case of the irregular waves the uplift was almost as important as the downward component.
It is interesting to note that Mogridge and Jamieson (1978) found that, in the case of an open diffuser cap, the maximum uplift and the maximum inline force occurred both approximately at mean water level. The situation observed here is different (see figure B.1). The peak inline force is occurring at MWL while and the peak uplift is observed at the wave trough. This behaviour resembles more what found by the authors in the case of a submerged sealed cylinder. This can mean that the loads on the velocity cap analyzed in this thesis do not differ much in nature from the ones on a submerged cylinder and that the openings of the cap are not so important to determine secondary internal flows that can generate the phase lag observed by Mogridge and Jamieson (1978).

Table B.1: Description of the 9 test cases involving irregular waves.

Test name (Irregular waves)	Water depth (h) [m]	H_s [m]	T_p [s]	Test duration [s]
JS101	0.58	0.1	2.07	518
JS102	0.58	0.1	1.60	400
JS103	0.58	0.1	1.27	320
JS201	0.62	0.1	2.07	518
JS202	0.62	0.1	1.60	400
JS203	0.62	0.1	1.27	320
JS301	0.68	0.1	2.07	518
JS302	0.68	0.1	1.60	400
JS303	0.68	0.1	1.27	320

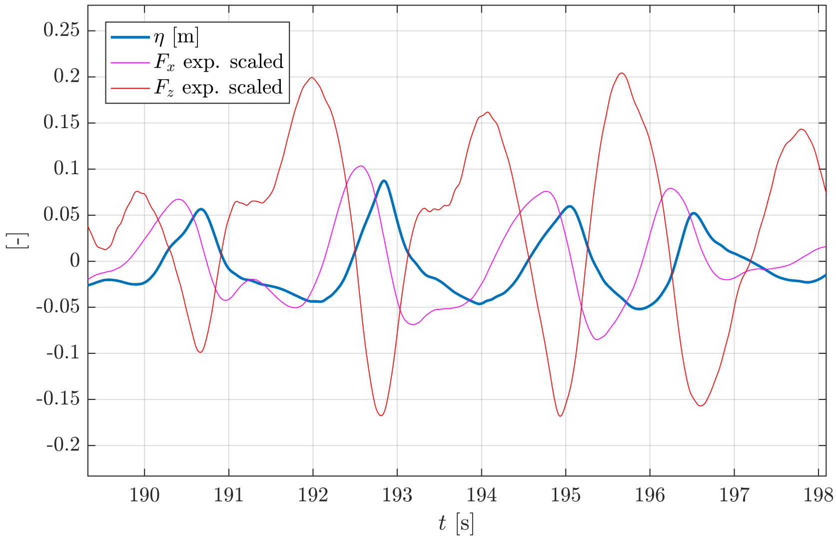

Figure B.1: Example of the phasing between loads and surface elevation in the case of test JS101. The scale factor is 50 for the both the inline and vertical force.

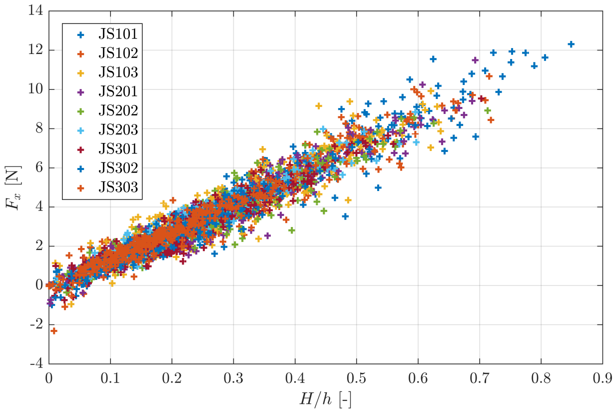

Figure B.2: Plot of the maximum inline force due to a single wave for all the nine tests involving irregular waves.

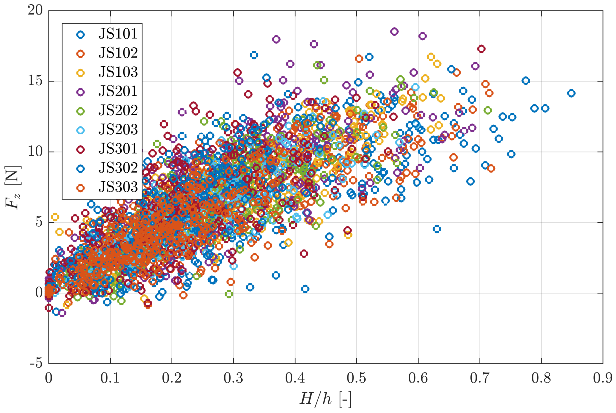

Figure B.3: Plot of the maximum uplift due to a single waves.

B.1. OCW3D modelling of the irregular wave cases

In a perspective of characterizing the experimental records of the loads on the velocity cap, an estimate of the undisturbed horizontal velocity needed to be defined so to fit the records with Morison and lift force equations. Given that no PIV measurements were taken for these test cases, an OCW3D set-up with the steering files of the irregular waves was prepared.

As for the solitary waves tests the calibration of the model was based on matching the surface elevation time series obtained with the model and from the experiments.

Several combination of breaking criterion *br* and POT value were analysed but the match was overall not accurate enough to proceed to the study of the numerical estimate of the velocity. Figure B.4 shows the case of JS102 as an example. Especially in the case of the highest waves of the simulation the model predicted significantly lower waves.

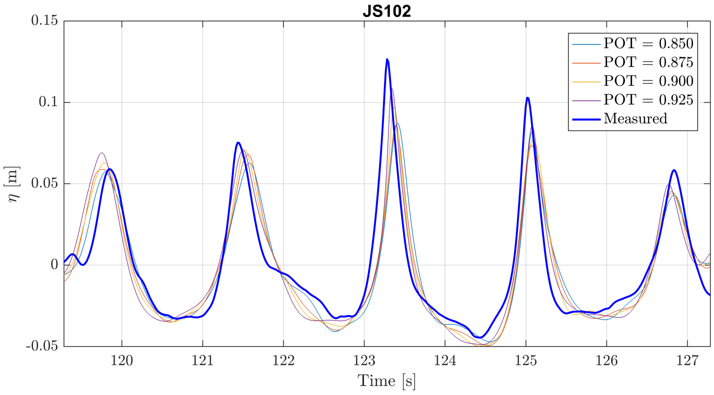

Figure B.4: Surface elevation at the sixth wave gauge as measured during the experiments and as computed by the potential flow solver. Data relative to test case JS102.

OCW3D has already been used successfully to model the surface elevation of an irregular wave field generated during physical tests, as documented in the work by Wilting (2017). However in that case the physical set-up was including a way to dissipate the wave energy at the end of the flume (i. e. a rubble mound). In the experiments examined in this thesis the wave energy that was not dissipated due to wave breaking at the end of the slope could propagate backwards and therefore modifying the irregular wave field generated by the wave paddle. The potential flow solver could not account for this condition and therefore the results were not matching the experimental records.

This mismatch prevented the modelling of those test cases in OpenFOAM because the results of OCW3D did not provide accurate inlet boundary conditions for the one-way domain decomposition strategy described in section 4.2.3.

C

Preliminary undisturbed velocity estimates

The velocity used in the force characterization was obtained sampling the horizontal velocity field next to the structure in the OpenFOAM simulations. The reason for this choice are described in chapter 6. Other ways to define the undisturbed velocity were also pursued and were eventually discarded. In this appendix a description of those estimates is presented.

C.1. PIV estimate

The availability of ensemble-averaged PIV measurements allowed to extract velocity time-series that could be used for the comparison with the other numerical estimates described later. The point selected for the extraction was chosen at a location as far as possible from the structure, but still in the PIV domain, in order to obtain an estimate of the velocity as unaffected by the presence of the cap as possible. The velocity was taken from a point 31 cm in front of the cap and 11.6 cm above the bed. It was decided to avoid depth averaging procedures in order to base the force coefficient calculation on a relatively simple velocity estimate that, when designing, could be obtained in a fast and cost effective way. The location along the x axis in the PIV window was highlighted by a red line in figure 3.12.

Figure C.1 shows the PIV velocity estimate extracted for test T201. As a reference, the signal of the velocity are reported also for the other points at the same location but at different water depths (the first 16.7 cm from the bottom, corresponding to the height of the cap).

Even if the PIV data provides the only direct observation of the velocity field around the velocity cap this velocity reconstruction is not used as an estimate of the undisturbed velocity. The reason regards the fact that in many cases only 5 test repetitions have been carried out and the resulting ensemble average gives a signal not smooth enough to be clearly representing the averaged flow conditions. Moreover, the Morison equation depends of the derivative of the velocity signal and the presence of wiggles is amplified when computing the derivative and the results are coarsened.

C.2. Analytic estimates of the horizontal velocity

A way to define the horizontal undisturbed velocities consists in integrating the kinematic boundary condition of the continuity equation. Knowing the time-dependent signal from the wave gauges for the surface elevation η, it is in fact possible, under the assumption of potential flow, to reconstruct the amplitudes of the velocities in the water column at the position of the cap. For the mathematical derivation, the equations used were continuity equation, neglecting the term in cross-flow direction (eq. C.1), and the kinematic boundary conditions at the bottom (eq. C.2, at $z = -h$) and at the free surface (eq. C.3, at $z = \eta$).

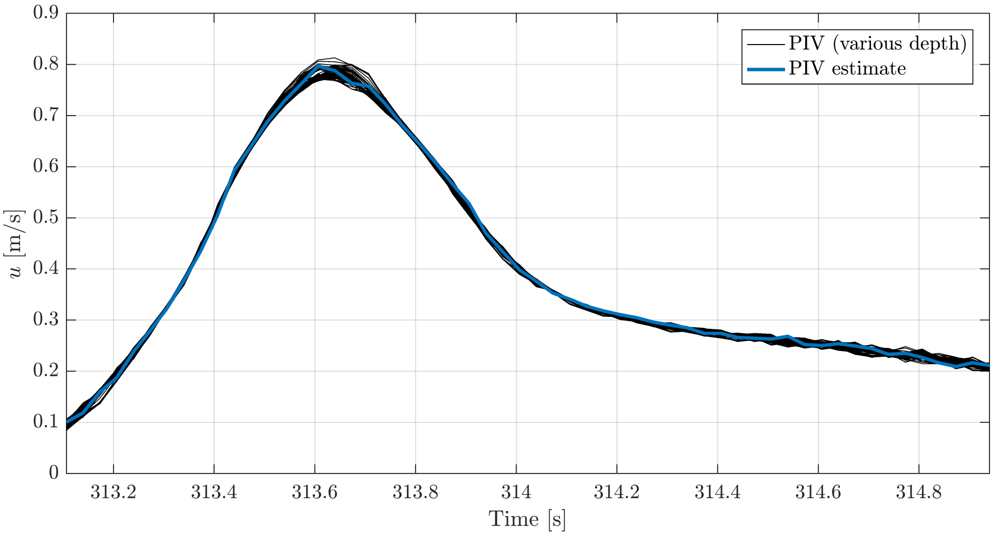

Figure C.1: Plot of the horizontal velocity approximately 31 cm in front of the cap, at the height of 0.116 m above the floor. Data relative to the ensemble-averaged results obtained from the 40 repetitions of test T201.

$$\frac{\partial u}{\partial x} = -\frac{\partial w}{\partial z} \tag{C.1}$$

$$w = 0 \tag{C.2}$$

$$w = \frac{\partial \eta}{\partial t} + u\frac{\partial \eta}{\partial x} \tag{C.3}$$

In the kinematic boundary condition, in this case, one should not neglect the non linear term given the shallow water situation and the intrinsic nonlinearity of a solitary wave.
In addition, when a wave is propagating with (almost) constant shape, it is possible to switch operator so to pass from a time derivative to a spatial derivative in the following way:

$$-c\frac{\partial}{\partial x} = \frac{\partial}{\partial t} \tag{C.4}$$

Thanks to eq. C.4 the continuity equation and the kinematic boundary condition at the surface can now be written as:

$$\frac{\partial w}{\partial z} = -\frac{1}{c}\frac{\partial u}{\partial t} \tag{C.5}$$

$$w = \frac{\partial \eta}{\partial t} - \frac{u}{c}\frac{\partial \eta}{\partial t} \tag{C.6}$$

Equations C.5 and C.6 are now written in a more convenient form because the information available from the experimental measures are time-series from the wave gauges and therefore they are function of time.
Ignoring that the vertical velocity is not linear over depth, the vertical gradient of the vertical velocity reads:

$$\frac{\partial w}{\partial z} \simeq \frac{w}{\eta + h} = \frac{1}{\eta + h}\left(1 - \frac{u}{c}\right)\frac{\partial \eta}{\partial t} \tag{C.7}$$

A first estimate of the horizontal velocity was therefore obtained by integrating in time the following differential equation [1]:

---

[1] To solve this implicit differential equation the MATLAB function $ode45$ was used (for reference see MATLAB Documentation).

$$\frac{\partial u}{\partial t} = \frac{1}{\eta + h}(c - u)\frac{\partial \eta}{\partial t} \tag{C.8}$$

The obtained signal is independent of the depth and showed always an overestimation of approximately 10 to 15 % with respect to the velocities recorded with the PIV measurements. The reason for this big mismatch is probably mostly related to the fact that the vertical velocity profile is not linear over the vertical and therefore eq. C.7 is not accurate enough.

The second approach consisted in using the formula for the horizontal velocity derived by Svendsen and Jonsson (1980) from the Boussinesq solitary wave theory. According to the pure solitary wave theory the expression for the surface elevation of such a wave propagating over a flat bottom is:

$$\eta = Hsech^2\left[\sqrt{\frac{3H}{4h^3}}(ct - x)\right] \tag{C.9}$$

Where H is the wave height and the wave celerity c is defined as $c = \sqrt{g(h+H)}$. The formula by Svendsen and Jonsson then reads:

$$u(z,t) = \sqrt{g \cdot h} \cdot \left(\frac{\eta}{h} - \left(\frac{\eta}{2h}\right)^2 + \left(\frac{1}{3} - \frac{1}{2} \cdot \left(\frac{z+h}{h}\right)^2\right) \cdot h \cdot \frac{\partial^2 \eta}{\partial x^2}\right) \tag{C.10}$$

In this formula, the velocity is function of the free surface elevation η, its second derivative in space (which can be written as a time derivative thanks to the operator swap of eq. C.4), the total water depth h and the vertical coordinate z.

The implementation of that approach gave results that were not matching the PIV measurements nor the subsequently obtained results from the numerical model (OCW3D). The reason is probably because the pure solitary wave theory and therefore the formula by Svendsen and Jonsson for the horizontal velocity was based on the assumption of a flat bottom and constant amplitude and shape of the wave. In the case treated here, the bottom has a slope and the solitary waves are shoaling and changing shape. This means that the general formula that describes a solitary wave in the Boussinesq model does not hold anymore and, therefore, so does not the formula by Svendsen and Jonsson (1980).

In both approaches, the operator swap of equation C.4 cannot be applied because the wave is not propagating with constant amplitude, (i.e. it is shoaling) nor with constant shape. The mismatch with the measured velocities from the PIV led to the decision not to work further with these first results.

Figure C.2 shows the estimates obtained with the methods of above and a comparison with the ensemble averaged PIV measurements relative to the tests repeated 40 times ('T201').

C.3. Velocities from the OceanWave3D computations

After the first results, the numerical model Oceanwave3D was used to obtain a better estimate for the horizontal velocity in absence of the cap. The description of the numerical set-up was given in chapter 4. The velocity was probed at the locations of the 7 numerical wave gauges defined in the OCW3D domain. The velocity reconstruction discussed here is based on the one at the position of the velocity cap (WHM6).

In all test cases, the comparison between the measured PIV data and the OCW3D results showed a good match. For plotting purpose only, the peak of the velocity in the PIV time-series was matched with the one of the computation of the numerical model.

Figure C.3 shows the comparison between the results of the numerical model and the PIV measurements plotted together with the old estimate obtained with the simple continuity equation integration. Both the PIV records and the OCW3D output consist of several time-series at the location of the velocity cap, one per vertical grid cell. The lines plotted in the figure are taken from the cell whose center is the closest to the height of the center of mass (0.116 m above the floor).
As far as the OCW3D results are concerned, an extra step is needed. The vertical discretization implemented

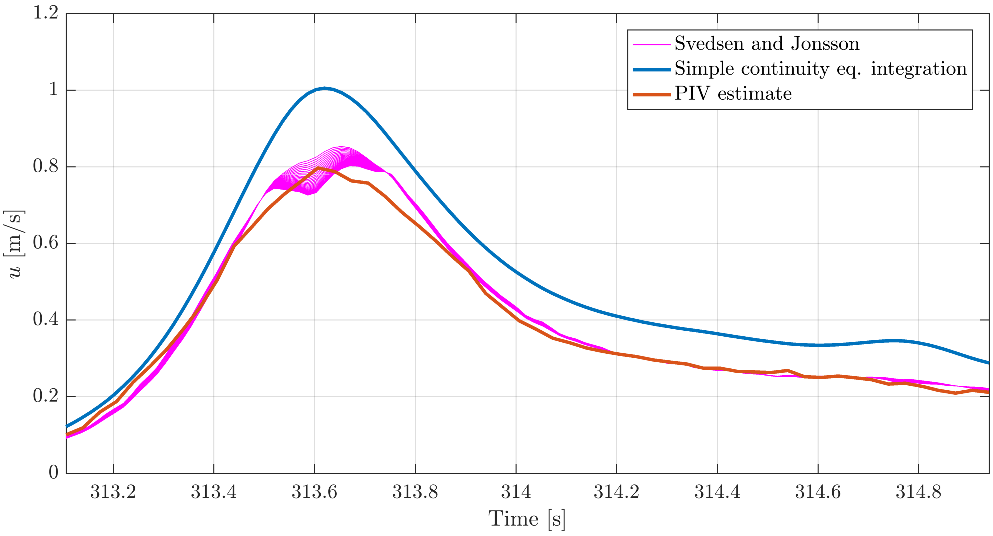

Figure C.2: Comparison of the first two attempts to compute the undisturbed velocity with the records extracted from the PIV measures. The result of the eq. by Svendsen and Jonsson (1980) dependents of the depth and is plotted in multiple lines. The fraction of water column for which the relative velocities are plotted is the height of the velocity cap above the bottom (16.7 cm).

in this model is the so-called σ-layer. This means that the outputs of the velocity are relative to the value σ = const. which is not equal to the value of the velocity at a constant depth. Before averaging, therefore the OCW3D output was interpolated at the desired heights (16 grid points over the height of the cap). Finally,the velocity signal was extracted from the grid point the closest to the center of mass of the cap. With regards to the peak of the signal, the model predicts velocities slightly bigger than the one observed in the PIV measurements. The reason can be that the velocity observed in the PIV window are not undisturbed by the presence of the cap or that a small mismatch between surface elevation computed by the numerical model and measured during the experiments was still observed after the tuning process.

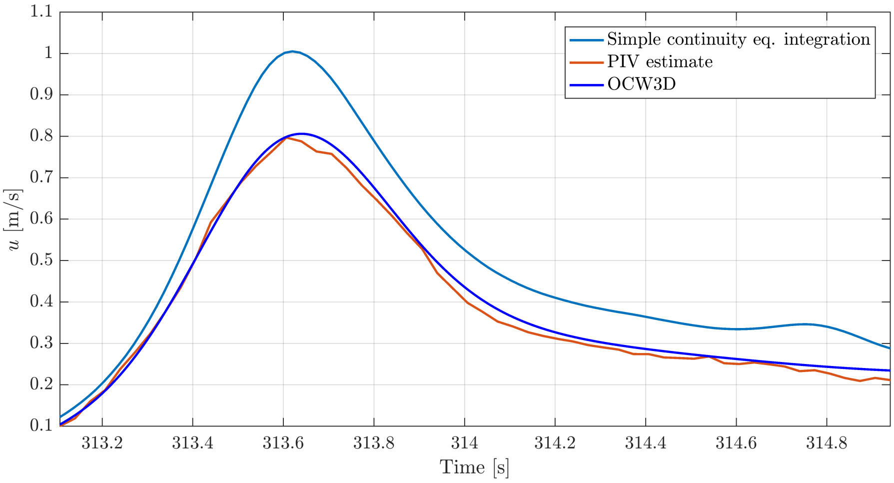

Figure C.3: Comparison of the results for the horizontal velocity at the position of the cap from the first computation attempted, from the PIV measurements and from the OCW3D model.

D

Implementation of the weighted least squares method for the coefficient fitting

The time-series of the loads were interpolated following the weighted least squares method. These method puts additional emphasis in fitting the curve around its peak being therefore a good instrument for finding force coefficients to be used in a design. This appendix contains the information on the actual implementation of this method and the formulas and procedures used to extract the force and moment coefficients.

D.1. General description of the weighted least squares method

From the algebraic point of view any curve in time $c(t)$ can be interpolated by means of a function $f(t)$ of the form

$$f = a_1 f_1(t) + a_2 f_2(t) + a_3 f_3(t) + ... + a_m f_m(t) \tag{D.1}$$

where $a_1, a_2, ...$ are the coefficients and $f_1, f_2, ...$ are generic functions of the variable t. Knowing the quantities $f_1, f_2, ...$ and the curve that needs to be fitted $c(t)$, the coefficients can be found by solving the system of equations that in matrix form reads

$$\begin{pmatrix} f_1(t_1) & f_2(t_1) & ... & f_m(t_1) \\ f_1(t_2) & f_2(t_2) & ... & f_m(t_2) \\ \vdots & \vdots & \vdots & \vdots \\ f_1(t_n) & f_2(t_n) & ... & f_m(t_n) \end{pmatrix} \begin{pmatrix} a_1 \\ a_2 \\ \vdots \\ a_m \end{pmatrix} = \begin{pmatrix} c(t_1) \\ c(t_2) \\ \vdots \\ c(t_n) \end{pmatrix} \tag{D.2}$$

or in compact notation

$$\overline{\overline{M}}\,\overline{a} = \overline{b} \tag{D.3}$$

Here the matrix of the known terms $\overline{\overline{M}}$ has dimension $n \times m$ being n the number of time steps in the time window considered and m the number of coefficients in the fitting equation.
The weighted least squares method theory then defines the error vector taking into account also a diagonal matrix of the weights.

$$\overline{e} = \overline{\overline{W}}(\overline{\overline{M}}\,\overline{a} - \overline{b}) \tag{D.4}$$

Without taking into account any weight all the equations of the system described above have the same importance in the determination of the final results of the coefficients. When fitting a force or a moment curve, however, it is more interesting to fit the curve at its maxima or minima. That is why in this thesis the weight matrix $\overline{\overline{W}}$ was used. The weight matrix is of dimension $n \times n$ and it has on its diagonal the squares of the loads that wants to be fitted.

The solution for the vector of coefficients $\overline{a}$ is sought minimizing the error matrix defined as $\overline{\overline{E}} = \overline{e}^T \overline{e}$ by setting its derivative with respect to the coefficients equal to zero.

$$\frac{d\overline{\overline{E}}}{d\overline{a}} = 0 \tag{D.5}$$

solving which for $\overline{a}$ gives

$$\overline{a} = \left[\overline{\overline{M}}^T \left(\overline{\overline{W}}^T \overline{\overline{W}} \right) \overline{\overline{M}} \right]^{-1} \overline{\overline{M}}^T \left(\overline{\overline{We}}^T \overline{\overline{W}} \right) \overline{b} \tag{D.6}$$

This expression allows finding the the vector of unknown coefficients. In the reviewed literature however the fitting equation is generally only function of two coefficients as in the Morison equations. In those cases instead of solving big systems of equations, a computationally cheaper solution is generally used.
When the fitting formula is the Morison equation ($f = f(t, C_D, C_M)$) and c is a generic known inline force time-series, the square error can be written in a different way as

$$\epsilon^2 = \frac{1}{N} \sum_{i=1}^{n} \left[[f(t_i, C_D, C_M) - c(t_i)]^2 c(t_i)^2 \right] \tag{D.7}$$

Setting the partial derivatives $\partial\epsilon^2/\partial C_D$ and $\partial\epsilon^2/\partial C_M$ equal to zero allows so define explicit formulas to define the force coefficients without solving any system of equation.
Depending on the number of coefficients of the fitting equation used the first or the second method was used.

D.2. Inline force fitting

The equation used to fit the inline force was the Morison equation. This equation is of the form

$$f = C_D f_D + C_M f_I \tag{D.8}$$

Where C_D and C_M are the force coefficients and f_D and f_M are functions of the velocity and of the acceleration respectively.

$$f_D = \frac{1}{2} \rho A U_0 |U_0| \tag{D.9}$$

$$f_I = \rho V \frac{\partial U_0}{\partial t} \tag{D.10}$$

In this situation it is convenient to use the equations proposed in literature to derive directly the force coefficients without setting the system of equations in matrix form. Once the time-series f_D, f_I and the time-series of the inline force F_x are known, the solution for the coefficients is

$$C_D = \frac{\sum(F_x^3 f_D) * \sum(F_x^2 f_I^2) - \sum(F_x^3 f_I) * \sum(F_x^2 f_D * f_I)}{\sum(F_x^2 f_D^2) \sum(F_x^2 f_I^2) - (\sum(F_x^2 f_D f_I))^2} \tag{D.11}$$

$$C_M = \frac{\sum(F_x^3 f_I) * \sum(F_x^2 f_D^2) - \sum(F_x^3 f_D) * \sum(F_x^2 f_D * f_I)}{\sum(F_x^2 f_D^2) \sum(F_x^2 f_I^2) - (\sum(F_x^2 f_D f_I))^2} \tag{D.12}$$

The summations are clearly on the number of elements of the F_x, f_I and f_D time-series and it depends on the duration of the time window considered. This formulas are broadly used in literature (see for instance Hur and Mizutani (2003) Hecimovich (2013)) and are obtained by setting the derivative of equation D.7 with respect to the coefficients equal to zero.

D.3. System of equations solved for the vertical force

The vertical force has been fitted in two ways. In the case of the lift force model the fitting equation can be written as:

$$f = C_L f_L \tag{D.13}$$

where

$$f_L = \frac{1}{2}\rho A U_0 |U_0| \tag{D.14}$$

when computing the weighted least square error the unknown is only one, so the equation to find C_L is only given by one partial derivative, which results in

$$C_L = \frac{\sum(F_z^3 f_L)}{\sum(F_z^2 * f_L^2)} \tag{D.15}$$

In the case of the new vertical force equation defined by 6.3 it is instead more convenient to write the problem in matrix form again. The system of equations set for computing the force coefficients would be written as:

$$\begin{pmatrix} \frac{1}{2}\rho A U_0(t_1)\left\|\overrightarrow{u_0(t_1)}\right\| & \frac{1}{2}A W_0(t_1)\left\|\overrightarrow{u_0(t_1)}\right\| & \rho V\frac{\partial W_0(t_1)}{\partial t} \\ \frac{1}{2}\rho A U_0(t_2)\left\|\overrightarrow{u_0(t_2)}\right\| & \frac{1}{2}A W_0(t_2)\left\|\overrightarrow{u_0(t_2)}\right\| & \rho V\frac{\partial W_0(t_2)}{\partial t} \\ \vdots & \vdots & \vdots \\ \frac{1}{2}\rho A U_0(t_n)\left\|\overrightarrow{u_0(t_n)}\right\| & \frac{1}{2}A W_0(t_n)\left\|\overrightarrow{u_0(t_n)}\right\| & \rho V\frac{\partial W_0(t_n)}{\partial t} \end{pmatrix} \begin{pmatrix} C_{Lx} \\ C_{Lz} \\ C_{Mz} \end{pmatrix} = \begin{pmatrix} F_z(t_1) \\ F_z(t_2) \\ \vdots \\ F_z(t_n) \end{pmatrix} \tag{D.16}$$

where $[t_1, \ldots, t_n]$ is the time window considered and the norm of the vector u_0 is $\left\|\overrightarrow{u_0(t_n)}\right\| = \sqrt{W_0^2 + U_0^2}$. The solution for the coefficients is then computed as in equation D.6.

D.4. System of equations solved for the centroidal moment

In the same way as for the vertical force fitting equation the system of equations reads:

$$\begin{pmatrix} \frac{1}{2}\rho A D U_0(t_1)\left\|\overrightarrow{u_0(t_1)}\right\| & \frac{1}{2}A D W_0(t_1)\left\|\overrightarrow{u_0(t_1)}\right\| & \rho V D\frac{\partial U_0(t_1)}{\partial t} & \rho V D\frac{\partial W_0(t_1)}{\partial t} \\ \frac{1}{2}\rho A D U_0(t_2)\left\|\overrightarrow{u_0(t_2)}\right\| & \frac{1}{2}A D W_0(t_2)\left\|\overrightarrow{u_0(t_2)}\right\| & \rho V D\frac{\partial U_0(t_2)}{\partial t} & \rho V D\frac{\partial W_0(t_2)}{\partial t} \\ \vdots & \vdots & \vdots & \vdots \\ \frac{1}{2}\rho A D U_0(t_n)\left\|\overrightarrow{u_0(t_n)}\right\| & \frac{1}{2}A D W_0(t_n)\left\|\overrightarrow{u_0(t_n)}\right\| & \rho V D\frac{\partial U_0(t_n)}{\partial t} & \rho V D\frac{\partial W_0(t_n)}{\partial t} \end{pmatrix} \begin{pmatrix} C_{D,mom,x} \\ C_{D,mom,z} \\ C_{M,mom,x} \\ C_{M,mom,z} \end{pmatrix} = \begin{pmatrix} M_{CoM}(t_1) \\ M_{CoM}(t_2) \\ \vdots \\ M_{CoM}(t_n) \end{pmatrix} \tag{D.17}$$

where $[t_1, \ldots, t_n]$ is the time window considered. The solution for the coefficients is then computed as in equation D.6.

E

Plots of the forces obtained in the RAS simulations

The plots of the force results obtained applying turbulence are included here. As in chapter 5 the experimental records are corrected in order to get rid of the additional pressure component.

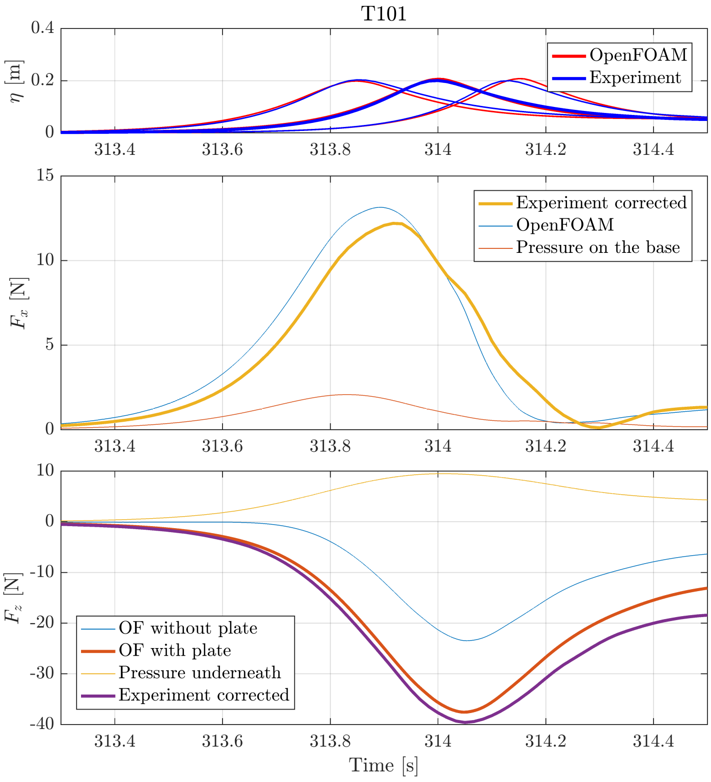

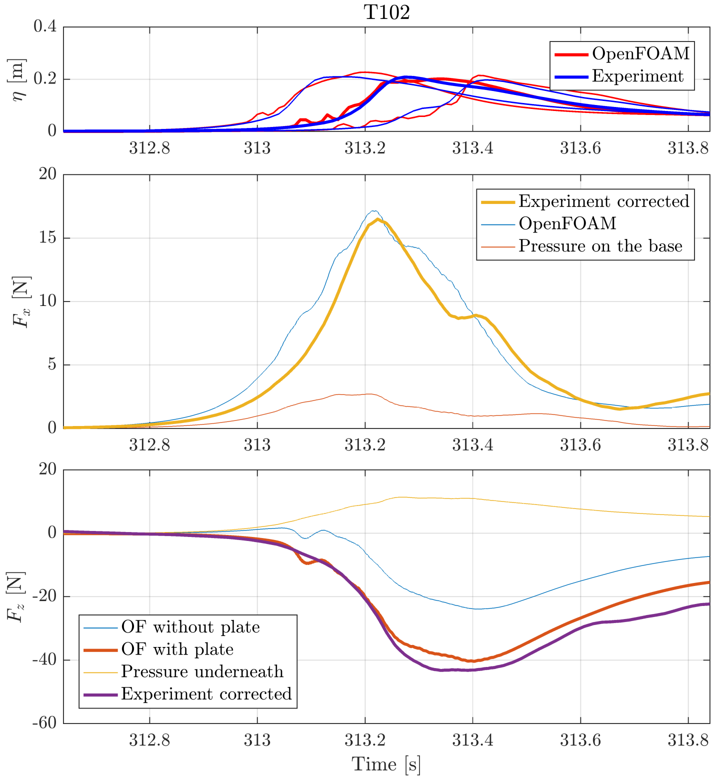
T102
η [m]
0.4
0.2
0
OpenFOAM
Experiment
312.8
313
313.2
313.4
313.6
313.8
F_x [N]
20
15
10
5
0
Experiment corrected
OpenFOAM
Pressure on the base
F_z [N]
20
0
-20
-40
-60
OF without plate
OF with plate
Pressure underneath
Experiment corrected
Time [s]

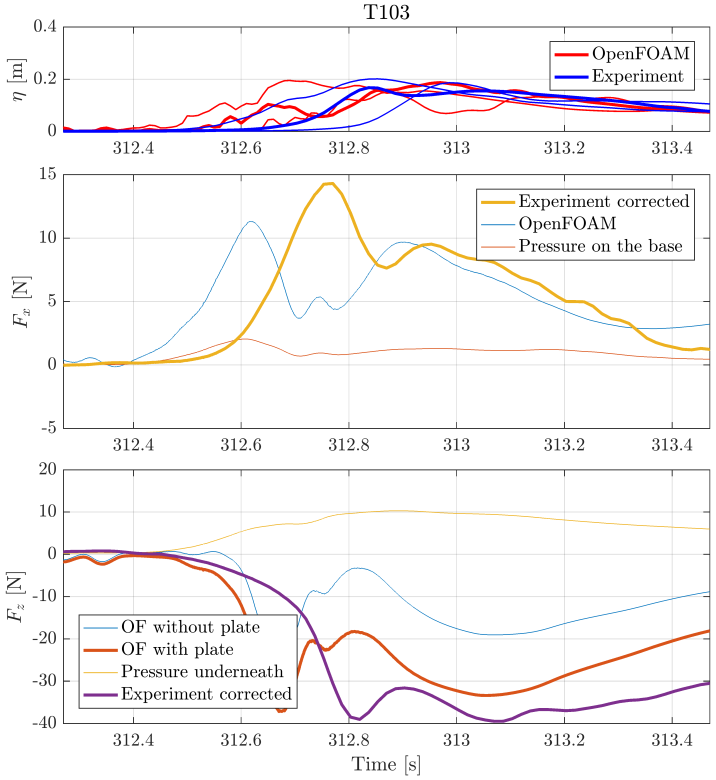
T103
η [m]
0.4
0.2
0
OpenFOAM
Experiment
312.4
312.6
312.8
313
313.2
313.4
F_x [N]
15
10
5
0
-5
Experiment corrected
OpenFOAM
Pressure on the base
F_z [N]
20
10
0
-10
-20
-30
-40
OF without plate
OF with plate
Pressure underneath
Experiment corrected
Time [s]

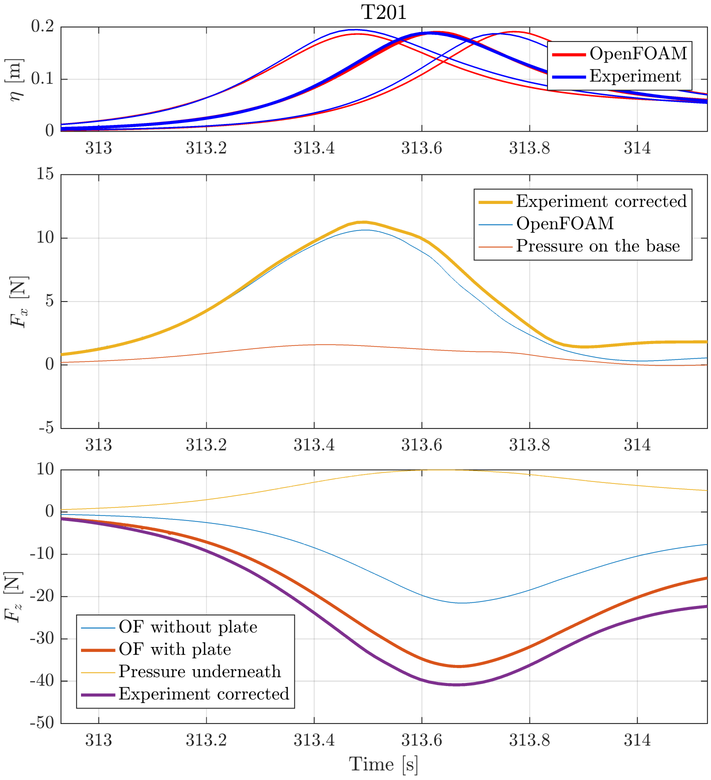
T201
η [m]
0.2
0.1
0
OpenFOAM
Experiment
313
313.2
313.4
313.6
313.8
314
F_x [N]
15
10
5
0
-5
Experiment corrected
OpenFOAM
Pressure on the base
F_z [N]
10
0
-10
-20
-30
-40
-50
OF without plate
OF with plate
Pressure underneath
Experiment corrected
Time [s]

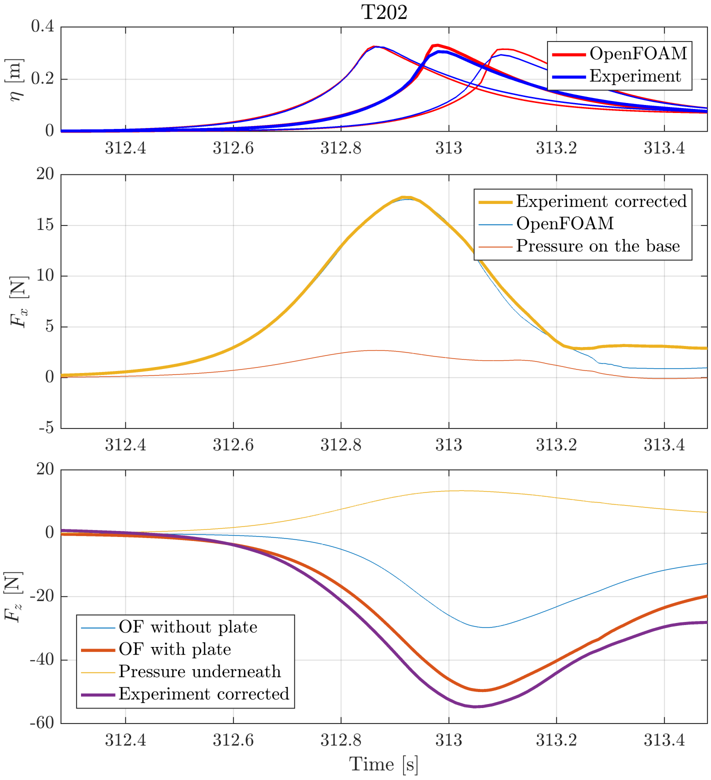
T202
η [m]
0.4
0.2
0
OpenFOAM
Experiment
312.4
312.6
312.8
313
313.2
313.4
F_x [N]
20
15
10
5
0
-5
Experiment corrected
OpenFOAM
Pressure on the base
F_z [N]
20
0
-20
-40
-60
OF without plate
OF with plate
Pressure underneath
Experiment corrected
Time [s]

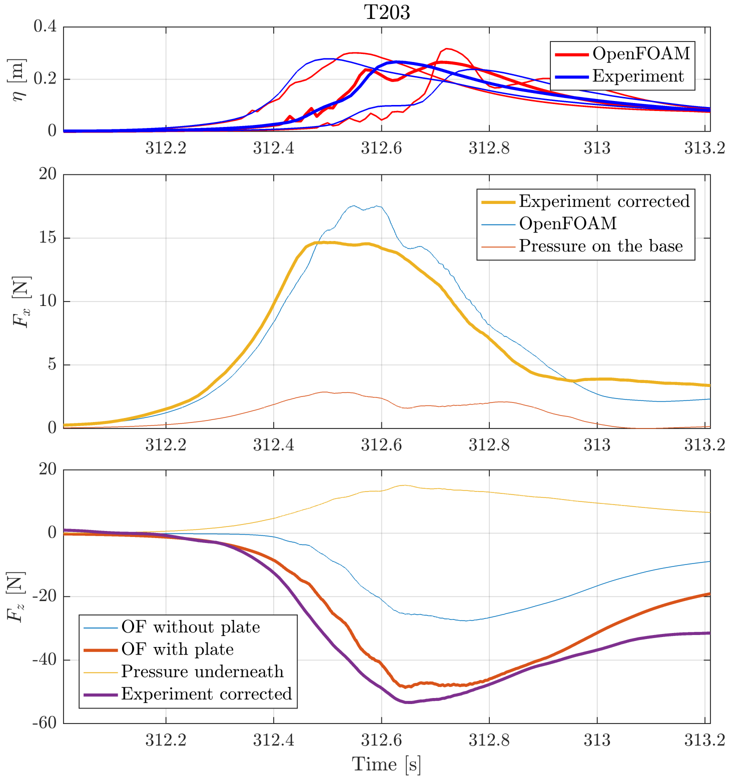
T203
η [m]
0.4
0.2
0
312.2
312.4
312.6
312.8
313
313.2
OpenFOAM
Experiment
F_x [N]
20
15
10
5
0
Experiment corrected
OpenFOAM
Pressure on the base
F_z [N]
20
0
-20
-40
-60
OF without plate
OF with plate
Pressure underneath
Experiment corrected
Time [s]

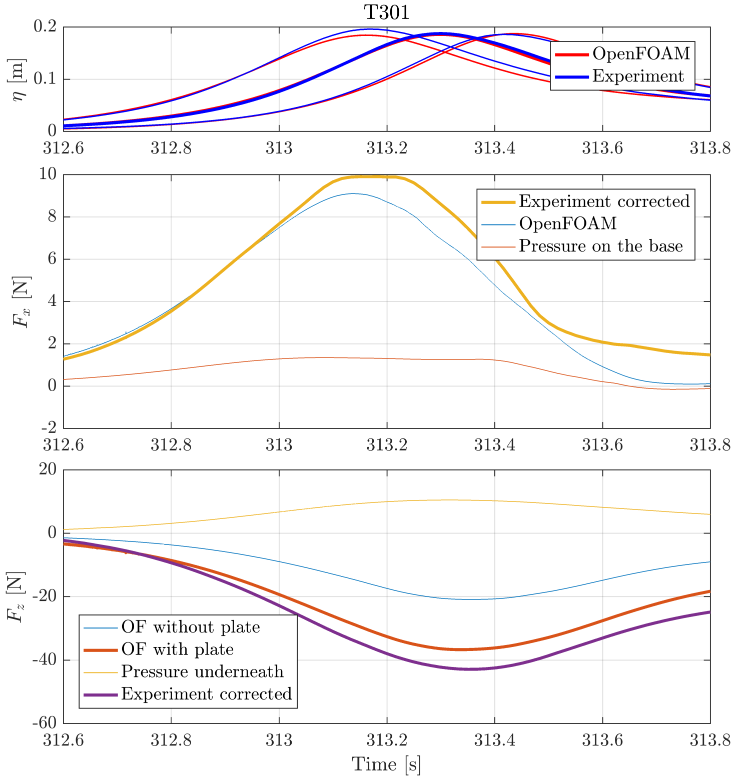
T301
η [m]
0.2
0.1
0
312.6
312.8
313
313.2
313.4
313.6
313.8
OpenFOAM
Experiment
F_x [N]
10
8
6
4
2
0
-2
Experiment corrected
OpenFOAM
Pressure on the base
F_z [N]
20
0
-20
-40
-60
OF without plate
OF with plate
Pressure underneath
Experiment corrected
Time [s]

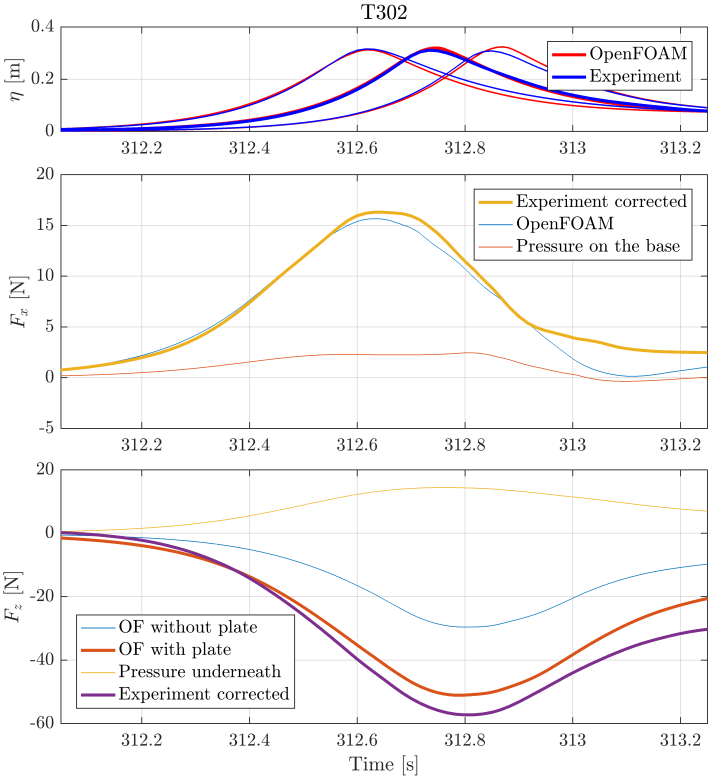
T302
η [m]
0.4
0.2
0
312.2
312.4
312.6
312.8
313
313.2
OpenFOAM
Experiment
F_x [N]
20
15
10
5
0
-5
Experiment corrected
OpenFOAM
Pressure on the base
F_z [N]
20
0
-20
-40
-60
OF without plate
OF with plate
Pressure underneath
Experiment corrected
Time [s]

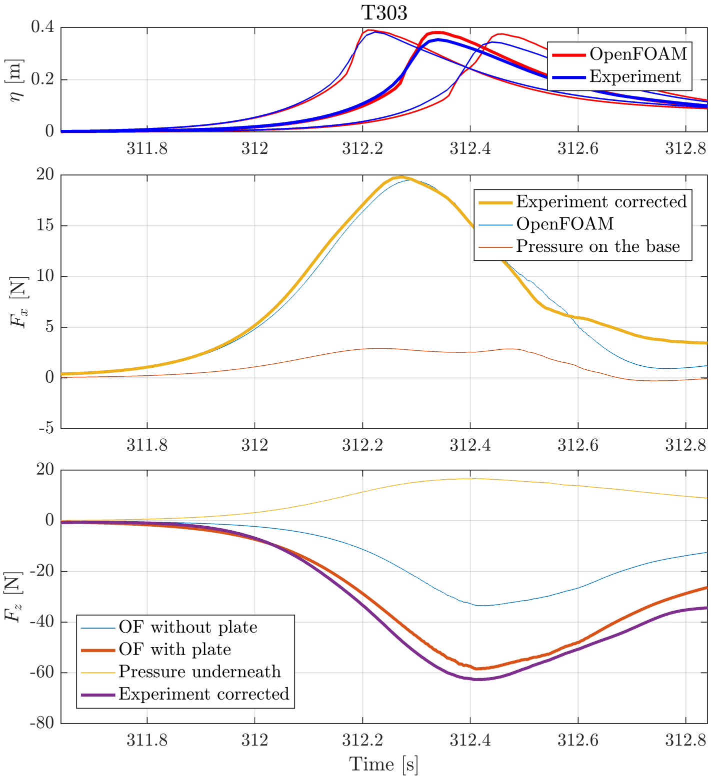
T303
η [m]
0.4
0.2
0
311.8
312
312.2
312.4
312.6
312.8
OpenFOAM
Experiment
F_x [N]
20
15
10
5
0
-5
Experiment corrected
OpenFOAM
Pressure on the base
F_z [N]
20
0
-20
-40
-60
-80
OF without plate
OF with plate
Pressure underneath
Experiment corrected
Time [s]

F

Numerical coefficients estimates

In this appendix the coefficients computed fitting the force and moment output of the numerical model are included.
The coefficients relative to the breaking cases are reported in red in the tables.

F.1. Inline force coefficients

Table F.1: Inline force coefficients computed from the OpenFOAM records of the inline loads. The coefficients are the drag and inertia coefficients defined as in equation 2.9. The error (ϵ) are expressed as a percentage of the computed signal and are estimated as in equation 6.6.

	Inline force		
Test case	C_D	C_M	$\epsilon(F_x)$
T101	0.93	0.77	5.67
T102	0.93	0.75	4.33
T103	0.77	0.69	13.55
T201_5	0.98	0.80	3.95
T201	0.94	0.79	5.73
T202	0.91	0.75	5.15
T203	0.93	0.76	4.30
T301_4	1.01	0.86	3.38
T301_5	0.98	0.81	3.86
T301_6	0.96	0.75	3.81
T301	0.95	0.79	5.54
T302	0.93	0.74	5.30
T303	0.91	0.74	4.68
T401_1	1.30	0.93	1.51
T401_2	1.24	0.91	2.56
T401_3	1.10	0.90	3.38
R1	2.81	0.91	1.92
R2	2.76	0.91	3.27
R3	2.57	0.93	4.37
R4	2.19	0.94	5.77
R5	1.80	0.95	5.39

F.2. Partial inline force coefficients

Table F.2: Inline hydrodynamics coefficients for the two components of the velocity cap. The error ϵ are express in percentage and are computed as in equation 6.6.

	Top part			Cylinder		
Test case	C_D	C_M	$\epsilon(F_{x,top})$	C_D	C_M	$\epsilon(F_{x,cyl})$
T101	0.93	0.60	2.28	0.77	1.39	15.18
T102	0.95	0.57	2.97	0.83	1.37	14.30
T103	0.68	0.49	15.83	0.85	1.50	12.75
T201_5	0.88	0.66	3.49	1.06	1.26	8.87
T201	0.84	0.66	5.75	1.03	1.22	10.32
T202	0.83	0.62	4.54	0.98	1.19	11.35
T203	0.87	0.61	4.92	1.00	1.26	12.00
T301_4	0.88	0.72	4.43	1.17	1.31	7.39
T301_5	0.84	0.69	5.29	1.15	1.22	7.69
T301_6	0.82	0.64	5.37	1.14	1.11	7.29
T301	0.80	0.68	7.57	1.12	1.17	8.89
T302	0.79	0.63	7.21	1.10	1.09	9.64
T303	0.79	0.63	5.84	1.07	1.10	11.02
T401_1	1.31	0.70	2.71	0.96	1.80	11.60
T401_2	1.16	0.72	2.54	1.12	1.65	12.66
T401_3	0.97	0.74	3.91	1.30	1.39	7.06
R1	3.17	0.63	2.56	0.48	1.96	1.03
R2	3.06	0.64	4.15	0.75	1.96	1.86
R3	2.83	0.66	5.37	0.90	1.95	2.39
R4	2.36	0.69	7.06	1.06	1.90	3.38
R5	1.93	0.71	6.44	1.12	1.81	3.71

F.3. Vertical force coefficients

Table F.3: Vertical force coefficients computed from the OpenFOAM records of the vertical loads. The reported coefficients are the lift force coefficients C_L as defined by equation 2.11 and the three new coefficients defined by equation 6.3.

	Original eq.		New vertical force eq.			
Test case	C_L	$\epsilon(F_z)(1)$ [%]	C_{Lx}	C_{Lz}	C_{Mz}	$\epsilon(F_z)(2)$ [%]
T101	-2.72	11.01	-2.88	4.22	-0.70	4.03
T102	-2.34	8.77	-2.75	0.46	-1.30	11.30
T103	-2.78	17.75	-1.45	1.60	2.86	27.95
T201_5	-3.42	8.09	-3.95	1.73	-2.60	5.29
T201	-2.90	9.24	-3.34	2.92	-2.00	1.91
T202	-2.36	9.57	-2.71	2.24	-1.42	4.66
T203	-2.32	4.41	-2.49	-0.17	-0.93	5.41
T301_4	-5.19	9.16	-6.24	-4.01	-7.77	5.31
T301_5	-3.81	8.51	-4.58	-0.06	-5.07	5.02
T301_6	-2.74	7.84	-3.30	1.58	-3.43	4.44
T301	-3.18	8.78	-3.83	1.71	-3.85	0.84
T302	-2.43	9.02	-2.89	2.17	-2.65	2.10
T303	-2.23	7.87	-2.63	0.80	-2.30	4.35
T401_1	-31.83	9.63	-39.88	29.92	-65.28	5.64
T401_2	-19.71	11.35	-26.03	0.13	-60.33	6.77
T401_3	-10.44	10.79	-13.42	-12.41	-30.09	8.13
R1	-30.93	13.70	-15.83	10.34	2.60	8.48
R2	-18.34	13.91	-11.11	10.13	2.11	8.68
R3	-15.52	13.34	-13.72	9.80	0.75	11.54
R4	-12.89	13.19	-15.43	9.17	-2.89	15.39
R5	-9.50	14.20	-13.02	5.68	-5.21	17.12

F.4. Centroidal moment coefficients

Table F.4: Centroiddal moment coefficients defined from equation 7.1. The errors (ϵ) are expressed as a percentage of the computed signal and are estimated as in equation 6.6.

Test case	$C_{D,mom,x}$	$C_{D,mom,z}$	$C_{M,mom,x}$	$C_{M,mom,z}$	$\epsilon(M_{CoM})$ [%]
T101	0.13	1.16	-0.07	0.08	7.22
T102	0.12	1.99	-0.13	0.10	3.30
T103	0.10	1.85	-0.16	0.07	20.57
T201_5	0.13	2.99	-0.21	0.12	12.03
T201	0.14	2.17	-0.16	0.15	5.29
T202	0.14	2.10	-0.16	0.15	3.82
T203	0.12	1.88	-0.12	0.12	8.26
T301_4	0.13	4.06	-0.22	0.21	10.20
T301_5	0.15	2.94	-0.20	0.27	5.48
T301_6	0.16	1.78	-0.13	0.30	6.28
T301	0.15	2.43	-0.18	0.25	3.78
T302	0.15	1.83	-0.14	0.26	5.55
T303	0.15	2.73	-0.22	0.29	6.96
T401_1	0.10	2.62	-0.11	0.02	2.11
T401_2	0.11	5.35	-0.15	0.14	6.62
T401_3	0.11	6.28	-0.21	0.24	10.99
R1	-0.15	-1.78	-0.10	-0.08	7.32
R2	0.03	-1.83	-0.10	-0.06	9.57
R3	0.14	0.07	-0.11	-0.05	8.85
R4	0.21	1.32	-0.11	-0.02	8.70
R5	0.20	1.11	-0.11	0.03	7.58